JULY 1984

# *Low Enrichment Fuel Evaluation and Analysis Program*

Summary Report for the Period
January, 1983 - June, 1984

WILLIAM KERR, Project Director


Department of Nuclear Engineering
and the
Michigan-Memorial Phoenix Project

# LOW ENRICHMENT

# FUEL EVALUATION

# AND

# ANALYSIS PROGRAM

Summary Report for the Period

January, 1983 to June, 1984

William Kerr, Project Director
Department of Nuclear Engineering
and the
Michigan-Memorial Phoenix Project
The University of Michigan
Ann Arbor, Michigan

July, 1984

## PROJECT PARTICIPANTS

William Kerr

John S. King

John C. Lee

William R. Martin

Reed R. Burn

Felippe Beaklini

Clifton Drumm

Brent Heuser

Baard Johansen

Gerald Munyan

William Wan

David Wehe

TABLE OF CONTENTS

## LIST OF FIGURES

LIST OF TABLES

# I. Introduction

The University of Michigan Department of Nuclear Engineering and the Michigan-Memorial Phoenix Project have been engaged in a cooperative effort with Argonne National Laboratory to test and analyze low enrichment fuel in the Ford Nuclear Reactor (FNR). The effort was begun in 1979, as part of the Reduced Enrichment Research and Test Reactor (RERTR) Program, to demonstrate, on a whole-core basis, the feasibility of enrichment reduction from 93% to below 20% in MTR-type fuel designs.

The key technical basis of the low enrichment uranium (LEU) fuel is to reduce the uranium enrichment while increasing, at the same time, the uranium loading of each fuel element in order to compensate for the reactivity loss due to the larger $^{238}U$ content. The required uranium loading can be achieved by increasing the uranium density in the fuel meat and by increasing the fuel volume fraction. At the same time it is necessary to insure that fuel elements operate within their thermal-hydraulic limits.

The first phase in our investigation performed in preparation for the LEU fuel testing in the FNR core included (a) initiation of development of experimental and analytical techniques applicable for neutronic evaluation of the MTR-type fuel elements, (b) selection of a LEU design for the FNR, (c) preparation of a preliminary FNR license amendment, and (d) a thermal-hydraulic testing program for the MTR-type fuel elements. The 1979 Summary Report[1] includes a discussion of this initial phase of the FNR LEU project.

Subsequent effort during 1980 was devoted to improving and validating the experimental techniques and analytical methods to be used in characterizing the high enrichment uranium (HEU) and LEU cores for the FNR. The experimental effort focused on the measurement of in-core and ex-core spatial flux distributions and the measurement of ex-core

spectra. In the analytical area, work has continued to improve and verify the computer codes and calculational models used to predict the neutronic behavior of the FNR. In addition, a series of thermal/hydraulic tests were performed for the MTR-type fuel elements and an amendment to the FNR Safety Analysis Report was submitted as part of the required License Amendment to the NRC to permit the use of the LEU fuel in the FNR. (Approval was granted in February 1981.) The 1980 Summary Report[2] presents the details of this phase of the LEU project.

The continuation of the project into 1981 culminated with the loading of the LEU core into the FNR and the achievement of initial criticality on December 8, 1981. The critical loading followed one-for-one replacements of HEU fuel elements with LEU fuel elements in the center and periphery of the FNR core. Following the critical loading, approximately six weeks of low power testing of the LEU core was performed including measurement of control rod worths, full core flux maps, and spectral measurements in-core and ex-core. This was then followed by two months of high power testing (2MW), during which similar measurements were taken. The experimental and analytical work performed during this phase of the LEU demonstration testing has been summarized in the 1982 Summary Report[3].

Testing of the LEU fuel at the FNR has continued during this reporting period. This included comparison of LEU core configurations with mixed HEU-LEU configurations. Unfolding of the neutron flux spectra through multiple foil activation analysis has been a major undertaking during this phase of the project. Considerable effort has also been expended during this period on comparison of subcadmium flux measured with rhodium self-powered neutron detectors (SPNDs) and with wire activations. Simulation and analysis of these flux data have been performed to explain the spatial-spectral dependence of the SPND sensitivity factor. Measurements and

analysis of reactivity parameters for LEU core configurations have also been undertaken.

Section II presents the demonstration experiments and testing portion of the current project, and discusses the measured differences in various neutronic characteristics between the HEU, LEU, and mixed HEU-LEU cores. This includes unfolding of neutron flux spectra through multiple foil activations as well as measurements of subcadmium flux distributions, control rod worths and reactivity coefficients. Section II also presents a comparison of subcadmium flux measured by SPNDs and iron wire activations, which is still a topic of current investigation. Section II makes extensive references to two papers[4,5] presented at the International Symposium on the Use and Development of Low and Medium Flux Research Reactors held in Cambridge, MA and at the International Conference on Reduced Enrichment for Research and Test Reactors held in Tokyo, Japan in October, 1983. These two papers are included as Appendices A and B to this Summary Report. Results of the spectral unfolding measurements are taken from D. Wehe's doctoral dissertation[6], and are presented as Appendix C.

Section III is devoted to the analysis of the FNR HEU and LEU core configurations and comparison with the measured data. The comparisons between calculation and experiment include subcadmium flux distributions, control rod worths, and core criticality. Similar to the discussion of the experimental program in Section II, Section III makes extensive references to Appendices A and B.

The FNR LEU project has also been involved to a significant extent in the area of generic methods development for MTR-type research and test reactors. Section IV summarizes the work performed in this area, including analysis of an IAEA research reactor benchmark problem and representation of the spectral-spatial coupling for generation of few-group cross sections for reflectors.

Section V summarizes the current status of the overall project, including a discussion of the tasks currently under investigation. The principal unresolved issues are identified and recommendations are made for future effort to complete the current and planned tasks.

## II. LEU DEMONSTRATION EXPERIMENTS AT THE FNR

During this 1983-1984 reporting period, the major emphasis in the LEU demonstration has involved performing:

1. Additional subcadmium flux measurements using iron wire activations and rhodium SPNDs. These measurements were particularly helpful in improving our understanding of the SPND detector sensitivity. The theoretical developments and experimental results were presented at the MIT International Symposium on the Use of Low and Medium Flux Research Reactors in October, 1983, and are discussed in Appendix A.

2. Measurements of the temperature coefficient of reactivity, power defect and void coefficient of reactivity, and control rod worth. The results of the latter two measurements and comparisons with preliminary calculations of control rod worths were presented at the annual RERTR meeting held in Japan last year. A revised copy of that paper included as Appendix B contains minor corrections to Figure 1 and Table 5. FNR operating experiences with the LEU fuel are also discussed in Appendix B.

3. The spectral unfolding of the HEU and LEU incore activation data. These measurements included separate unfoldings for the thermal/epithermal spectra, and the fast spectra. These results have been published as part of a doctoral thesis, and are included as Appendix C.

### A. SPND Sensitivity Measurements

During this past 1983-1984 reporting period, effort has been made to more accurately determine the sensitivity of our rhodium SPND. The SPND sensitivity measurements were primarily performed at two locations, the core center (L-37) and the heavy water reflector ($D_2O$ tank), and for LEU cores and mixed HEU-LEU cores. Measurements in the light water reflector (L-40) have also been performed.

To ensure accuracy, both the SPND measurements and the foil activations are performed within a period of 24 hours. The net current from the rhodium emitter wire is measured as the SPND, mounted to an Inconel paddle, is held in place by a brace fitted to the top of the fuel element. A complete SPND axial scan is usually performed. An absolute measure-

ment of the subcadmium neutron flux is made by irradiating a bare foil and a cadmium covered foil. The bare and cadmium foils are taped, side by side, to a thin aluminum paddle which is then inserted between the fuel plates of the fuel element. The ratio of SPND net current, corrected for epicadmium current and paddle flux depression, to absolute subcadmium flux yields the SPND sensitivity. The 1979 Summary Report includes a complete description of the SPND and foil activation experimental procedures.

Table 1 presents the sensitivity measurements performed in this reporting period along with measurements made in 1982 for a HEU core. Although this work is not completed it is evident that the measured value of the SPND sensitivity in the heavy water reflector is significantly higher than in the core center fuel element. The large discrepancy between heavy water reflector measurements made in the LEU core and in the mixed HEU-LEU core is of concern. Further efforts underway should determine a more consistent SPND sensitivity in the heavy water reflector. A complete description of SPND and foil activation flux measurements is contained in Appendices A and B.

Table 6 in Appendix C gives a comparison of subcadmium fluxes measured by different reactions. As explained in Appendix C, there is an apparent inaccuracy in the ENDF-IV Fe-58 $(n,\gamma)$ cross section. For thermal energies the iron capture cross section is underestimated by approximately 12%. When this cross section is adjusted accordingly the in-core SPND sensitivity increases, bringing our quoted value of the sensitivity into better agreement with values quoted by other authors. Table 2 of this section is an updated table from Appendix A, showing our work along with the work of other authors.

B. SPND Flux Measurements

Several SPND maps have been obtained during this reporting period. The SPND subcadmium flux values for a 38-

Table 1

Measured SPND Sensitivities at 1/4-Core Height for HEU, LEU and Mixed Cores[1]

| Location Fuel Type | Iron Wire | | Rh Wire | SPND | $S_{sc}$[2] |
|---|---|---|---|---|---|
| | $\sigma$ (barns) | $\phi_{sc}$ ($10^{13}$ n/cm$^2$-s) | $f_{sc}$ | $I_{net}$ ($10^{-9}$amps) | ($10^{-21}$amps/$\phi_{sc}$-in) |
| Core Regular Element | | | | | |
| HEU[3] | .844 | 2.52 | .81 | 47.78 | 1.64 |
| LEU | .844 | 1.99 | .75 | 43.32 | 1.75 |
| Mixed[4] | .844 | 1.78 | .75 | 41.60 | 1.87 |
| $D_2O$ Reflector | | | | | |
| HEU[3] | .907 | 1.96 | .90 | 52.67 | 2.60 |
| LEU | .907 | 2.44 | .89 | 56.97 | 2.22 |
| Mixed[4] | .907 | 1.90 | .89 | 54.80 | 2.75 |
| $H_2O$ Reflector | | | | | |
| Mixed[4] | .907 | 1.63 | .93 | 36.90 | 2.25 |

[1] Rhodium emitters were 2.54 cm long and .0508 cm diameter.

[2] Measured sensitivity increased by 7% to account for support paddle.

[3] Cross section calculated for LEU spectrum is used for HEU case

[4] LEU fuel element at center-of-core lattice position.

Table 2

Comparisons of SPND Sensitivity

| Author | Emitter Diameter (mils) | $S_{2200}$ ($10^{-21}$amps/$\phi_{2200}$-cm) | $S_{sc}$ ($10^{-21}$amps/$\phi_{sc}$-cm) | |
|---|---|---|---|---|
| | | | Core | $D_2O$ |
| **Measurements** | | | | |
| Warren | .020 | 1.20 | .89 | .95 |
| Kroon | .018 | .91 | - | - |
| | .020 | .99 | .76 | .80 |
| Jebair | .020 | 1.01 | - | - |
| Baldwin | .018 | .96 | - | - |
| | .020 | 1.04[1] | .77 | .83 |
| This work (LEU) | .020 | 1.04[4] | .77[4] | .97[4] |
| ($D_2O$) | .020 | 1.23[4] | - | - |
| **Calculations** | | | | |
| This Work (VIM-LEU) | .020 | .99 | .73 | .78 |
| (VIM-$D_2O$) | - | .98 | - | - |
| Warren | .020 | 1.31 | .97 | 1.04 |
| Laaksonen | .018 | .75[2] | - | - |
| | .020 | .88[3] | .64 | .68 |
| Goldstein | .020 | 1.51 | 1.12 | 1.20 |

(1) Extrapolated to 20 mils based on Kroon's experiment.
(2) Value interpolated off graph at $E_T$=.030 eV.
(3) Extrapolation based on Laaksonen's estimate.
(4) Sensitivity updated after correction to iron capture cross section.

element HEU core, a 33-element LEU core, and a 34-element HEU/LEU mixed core are shown for a north-south and east-west traverse in Figures 1 and 2, respectively. The complete SPND subcadmium flux maps are presented later in Section III.B together with calculated results.

The replacement of the large equilibrium HEU core by the smaller and fresher LEU and mixed cores reduces the core flux and raises the flux in both the $H_2O$ and $D_2O$ reflectors (see $D_2O$-X in Figure 1), as observed earlier[3]. The increases in reflector peaking are dominated by the reduced core dimension in the north-south direction associated with the smaller LEU and mixed cores. The large peaks at L-57 in Figure 2 are due to the special element waterholes in the HEU and LEU core.

As reported in Appendix B of Ref. 3, the replacement of a single fresh HEU element by a fresh LEU element at the center (L-37) of an equilibrium HEU core produces a local flux depression. The ratio of HEU to LEU local flux is ~1.19. As seen in Figure 1, compared with the HEU core the presence of an LEU element in the mixed core at L-37 lowers the subcadmium flux by a factor of 2.15/1.81, or 1.19, as expected.

C. Temperature Coefficient of Reactivity

The temperature coefficient of reactivity measurement is normally performed at the FNR in conjunction with the calorimetric test. In the experiment reactor power is increased from low power to 1 MW and stabilized while the secondary cooling system remains off. Four thermocouples measure bulk pool temperatures at 2' and 20' below the pool surface, and heat exchanger inlet and exit temperatures. Pool water temperatures and control rod heights are recorded when power first reaches 1 MW and, again, about one hour later. The reactivity change is calculated from the change in regulating rod position associated with the temperature increases registered at the thermocouples.

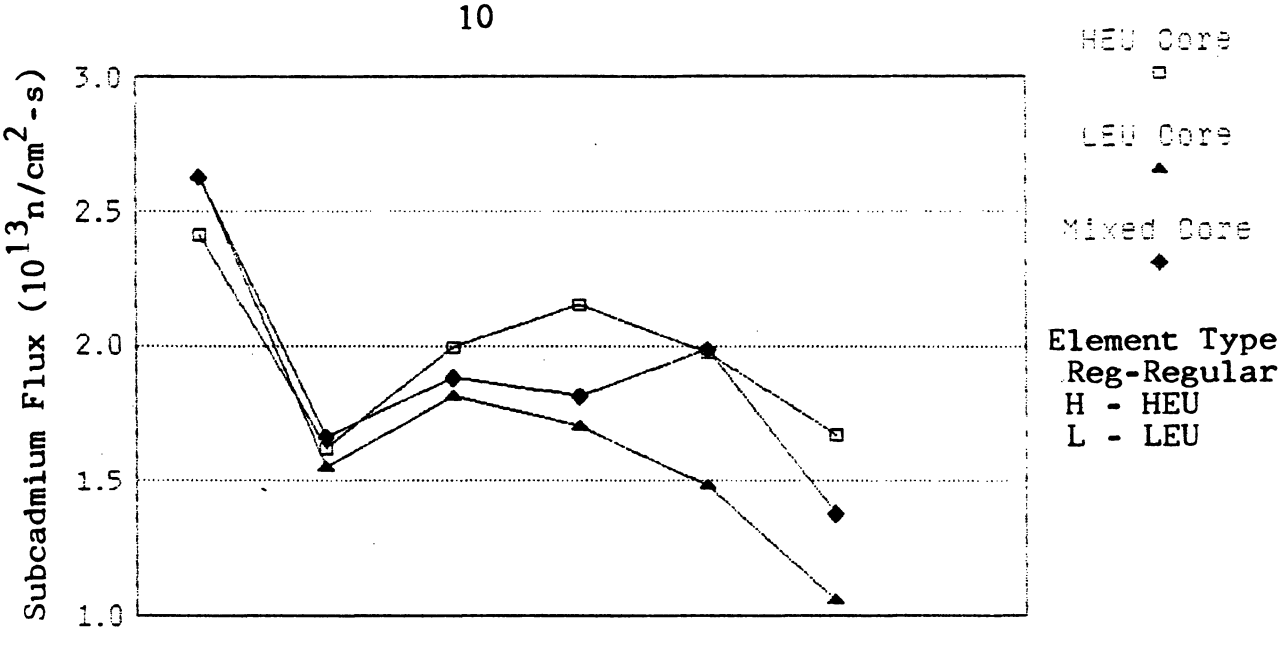


Figure 1 SPND North-South Flux Profiles for HEU, LEU and Mixed Cores

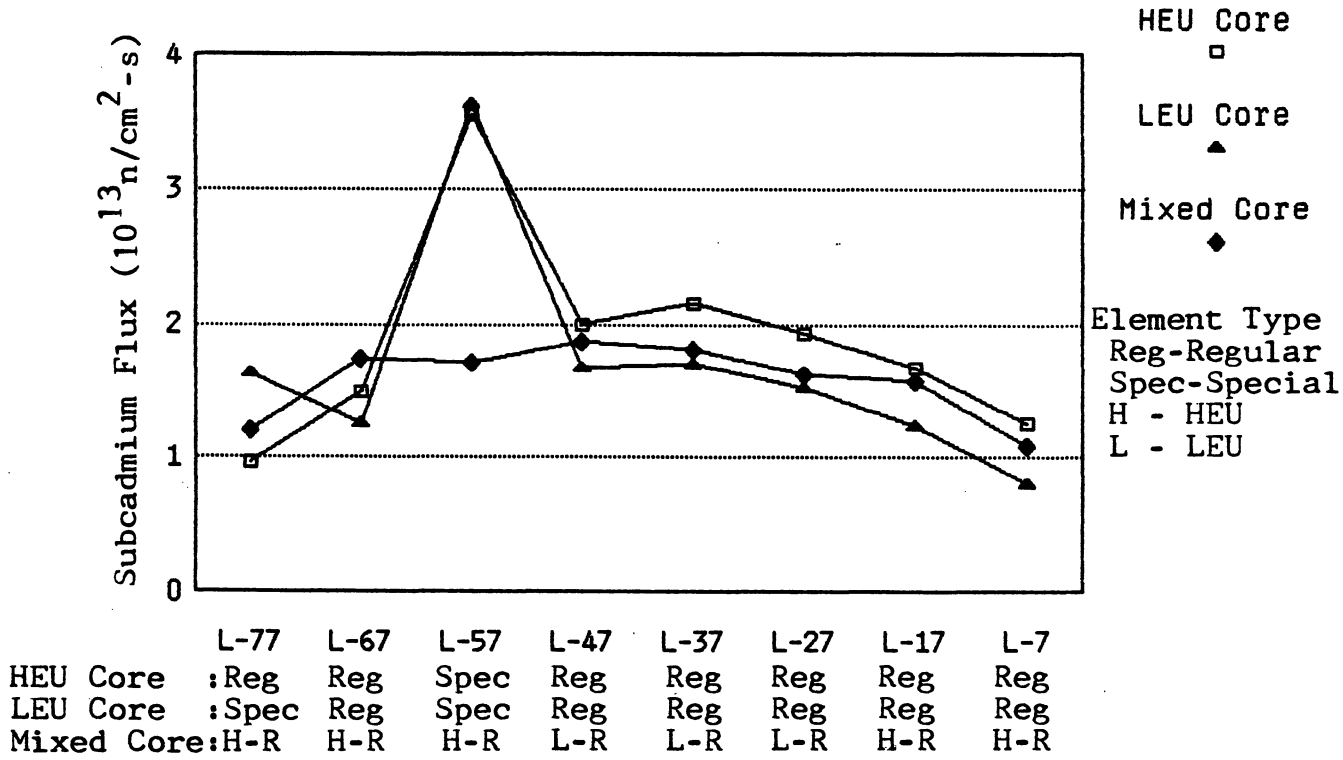


Figure 2 SPND West-East Flux Profiles for HEU, LEU and Mixed Cores

In the temperature coefficient measurement performed for the July, 1983, LEU core [FNR Cycle 227A], the average temperature rise obtained over a period of one hour and three minutes from the four thermocouples was 9.8°F, yielding a temperature coefficient of reactivity of $-7.9 \times 10^{-3}$ %Δk/k/°F. Earlier measurements yielded a temperature coefficient of reactivity of $-7.5 \times 10^{-3}$ %Δk/k/°F for the March, 1981, HEU core [FNR Cycle 196A], $(-6.1 \pm 1.4) \times 10^{-3}$ %Δk/k/°F for the April, 1983, mixed core [FNR Cycle 224A], and $(-7.3 \pm .9) \times 10^{-3}$ %Δk/k/°F for the February, 1984, mixed (mostly LEU) core [FNR Cycle 234C].

D. Power Defect of Reactivity

The power defect of reactivity represents the total of all reactivity effects induced by taking the reactor from a cold zero-power condition to the normal operating condition. Two different techniques were utilized to measure the power defect. The first method involves measuring the reactivity inserted by the regulating rod as core power is quickly increased from 5 kW to 1 MW with the secondary cooling system off. Linearly extrapolating the reactivity change to 2 MW yields the power defect at full power. In the second method the secondary cooling system remains on while power is brought from 50 kW to 2 MW.

The first method yielded a power defect measurement of -0.21 %Δk/k for the September, 1979, HEU Core [FNR Cycle 177], -0.31 %Δk/k for the May, 1982, HEU core [FNR Cycle 211B] and -0.25 %Δk/k for the July, 1983, LEU core [FNR Cycle 227C]. Based on the second method the power defect for the August, 1983, LEU core [FNR Cycle 227D] was measured as -0.23 %Δk/k. Both approaches yield similar results for the LEU cores. The discrepancy in power defects measured for the HEU cores is currently under investigation. Efforts are also underway to simulate these measurements.

E. Void Coefficient of Reactivity

In the void coefficient of reactivity experiment the void is simulated by inserting an aluminum blade measuring .040" x 2.25" x 24.0" into the central water channel of the fuel elements. Once the blade is inserted and reactor power stabilized at 2 MW the core reactivity change is calculated from the change in regulating rod position.

The core configurations and control rod positions for experiments performed on the February, 1979, HEU core [FNR Cycle 169B] and the July, 1983, LEU core [FNR Cycle 227A] are shown in Figures 3 and 4, respectively. The measured void coefficients of reactivity for the HEU and the LEU core presented in Figure 5 are similar to one another when uncertainties in measurements are considered. The uncertainties in the measured void coefficients of reactivity in Figure 5 represent the variation in the measurements taken by three students during the February, 1979, experiment. Figure 5 also includes corrections of minor typographical errors present in Figure 1 of Appendix B.

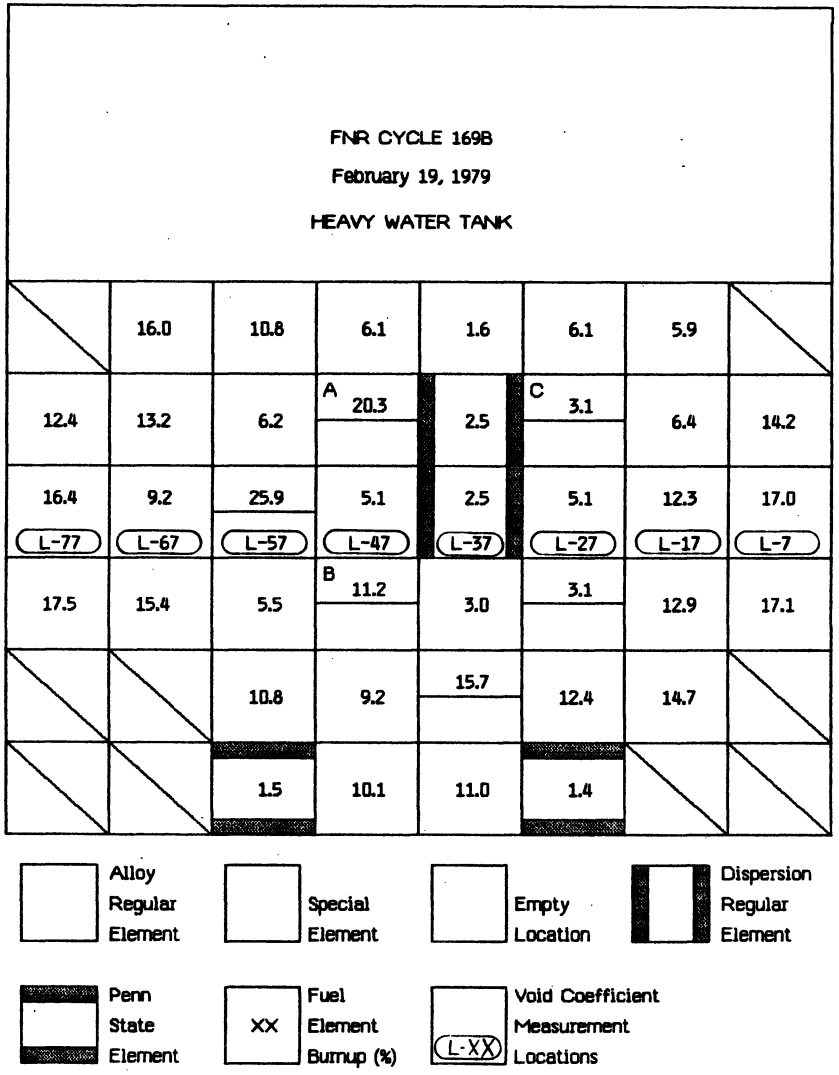


Figure 3 Core Configuration for Void Coefficient of Reactivity Experiment - February 1979 HEU Core

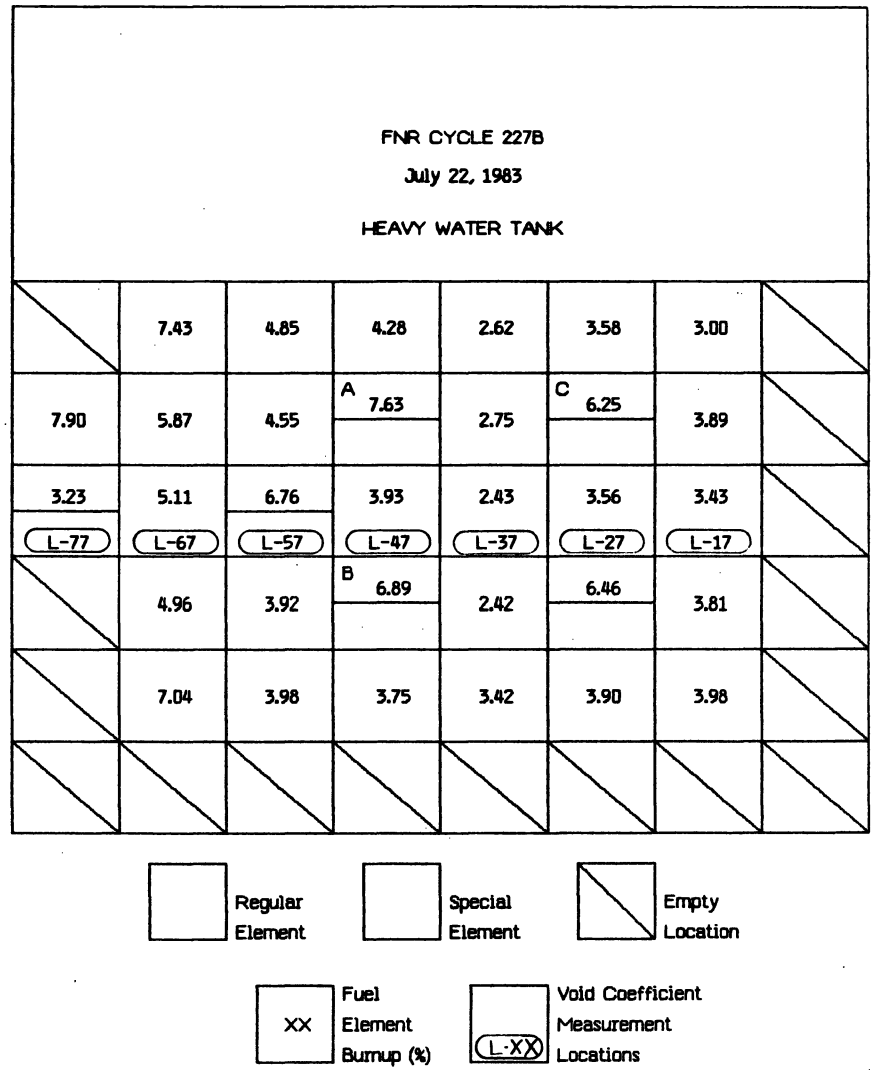


Figure 4 Core Configuration for Void Coefficient of Reactivity Experiment - July 1983 LEU Core

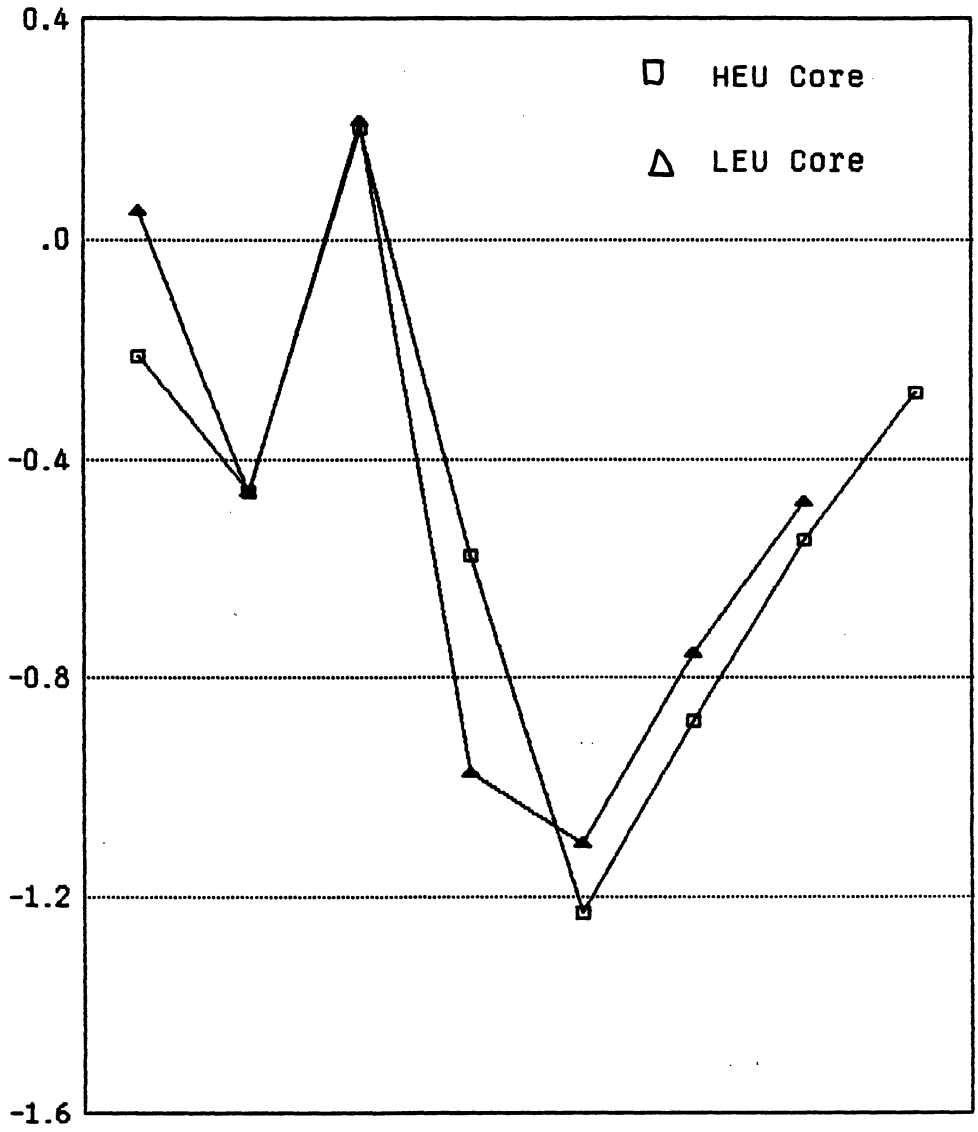


| | L-77 | L-67 | L-57 | L-47 | L-37 | L-27 | L-17 | L-7 |
|---|---|---|---|---|---|---|---|---|
| HEU Core: | Reg | Reg | Spec | Reg | Disp | Reg | Reg | Reg |
| LEU Core: | Spec | Reg | Spec | Reg | Reg | Reg | Reg | Reg |
| Measured Uncertainty: | ±.07 | ±.13 | ±.23 | ±.32 | ±.02 | ±.01 | ±.04 | ±.01 |

Figure 5 Void Coefficient of Reactivity Across a West-East Traverse of the FNR Core for LEU and HEU Fuels

# III. SIMULATION AND ANALYSIS OF THE TEST DATA

## A. Iron Wire Activation Analysis

Much of the experimental work performed during the LEU project involved the determination of subcadmium flux distributions by means of iron wire activations and rhodium SPND measurements. The determination of the subcadmium flux from the SPND and iron wire measurements is the subject of this section of the report.

This section will begin by presenting the methods for determining the subcadmium flux from iron wire measurements, which involves the determination of effective subcadmium cross sections for Fe-58, in spectra corresponding to the core center and ex-core regions. Then, the determination of subcadmium flux distributions from rhodium SPND measurements will be discussed. This includes effective subcadmium cross sections for rhodium in spectra corresponding to the core and ex-core regions and the flux depression caused by the rhodium wire.

The subcadmium flux can be determined from bare and cadmium covered iron wires as follows:

$$\phi_{sc} = \frac{A_b - A_{cd}}{\sigma_{58}} \tag{1}$$

where $A_b$ and $A_{cd}$ are the measured saturated activities per Fe-58 nucleus for bare and cadmium covered iron wires, respectively. Here, $\sigma_{58}$ is the effective subcadmium cross section for Fe-58 defined as follows:

$$\sigma_{58} = \frac{\int_0^{E_c} \sigma_{58}(E)\phi(E)dE}{\int_0^{E_c} \phi(E)dE} \tag{2}$$

where $\sigma_{58}(E)$ is the activation cross section for Fe-58, $\phi(E)$ is an approximation to the flux spectrum, and $E_c$ is the cadmium cutoff energy. Since Fe-58 is a weak absorber, there is no need to consider flux depression in the wire, so all that is needed is to determine the unperturbed flux spectrum in the region where the measurement is made.

The subcadmium cross section for Fe-58 has been determined by utilizing several codes in the SCALE package[7]. The CSAS code is used to set up the input for the NITAWL and XSDRN[8] codes. The iron wire is modelled in cylindrical geometry with a surrounding environment to simulate insertion into an LEU core, an HEU core, and penetration X of the heavy water tank. To simulate the core environments, fuel, moderator, clad, and non-lattice regions are volume averaged and homogenized, with number densities corresponding to the values given in Table C-2 of Ref. 2. A .05 cm diameter iron wire is surrounded by a light water region of .2 cm outside diameter followed by a core region of 16 cm outside diameter.

The NITAWL code is run to perform resonance calculations for the uranium isotopes with the Nordheim Integral Treatment. NITAWL also sets up a cross section library in a format accessible by the XSDRN code. The XSDRN code is then run in a 123-group, cylindrical geometry calculation, with 4 meshes in the iron wire and 20 meshes in the surrounding region, for a total of 24 meshes. The quadrature order is S-8 and the order of scattering is P-3, with a white outer boundary condition. The XSDRN code is used to generate a 30-group library from the 123-group SCALE library. The 30-group library generated by the XSDRN code contains one set of microscopic cross sections for each isotope in each zone of the problem.

The ICE code[7] is then used to generate a macroscopic cross section library for use in the ANISN code. Most of the analysis for both the iron wire activations and for the

SPND measurements are performed with the ANISN code[9] utilizing the 30-group library generated by the XSDRN and ICE codes.

In order to determine the subcadmium cross section for Fe-58 in the core region, a .05 cm diameter iron wire is surrounded by a .2 cm diameter region of light water and a 40 cm diameter region of a homogenized mixture of fuel, clad, moderator, and non-lattice regions. An S-8, P-1 calculation is then performed in 30 groups with the ANISN code to determine the flux weighted, subcadmium cross section for iron. These values are given in Table 3. Since iron is a 1/v absorber in the thermal range, the cross section for Fe-58 can be determined by multiplying the total iron activation cross section by the ratio of the Fe-58 2200 m/s cross section to the total iron 2200 m/s cross section, and this is also given in Table 3. In this analysis, the iron number density is taken to be .08491/b-cm, and the cadmium cutoff energy is .625 eV, with the values for .625 eV obtained by interpolating the values at .5488 eV with those at .6552 eV available with the 30-group library.

Table 3

Subcadmium Cross Sections for Iron Wire (barns)

| Region | $\sigma_{Fe}$ | $\sigma_{58}$ |
|---|---|---|
| 2200 m/s | 2.58 | 1.18 |
| LEU Lattice | 1.86 | .850 |
| HEU Lattice | 1.87 | .854 |
| $D_2O$-X | 2.00 | .913 |

Similar calculations were performed for an iron wire inserted into position X in the heavy water tank. A .05 cm diameter iron wire is surrounded by a 2.54 cm diameter region of light water followed by a 12.54 cm region of heavy

water. A shell source is input on the boundary of the heavy water region to simulate the incoming current of neutrons from the core. The spectrum for the shell source was obtained from a one-dimensional, global core, slab geometry calculation. The spectrum at the core-heavy water tank interface was used as a shell source input for the iron wire activation calculation. The subcadmium cross section for an iron wire inserted into heavy water tank penetration X is also given in Table 3. The $\sigma_{58}$ values of Table 3 represent a slight improvement over the corresponding values given in Table I of Appendix A.

Alternatively, the iron wire activations can be analyzed by calculating the activation of bare and cadmium covered irons wires directly. If the subcadmium flux is defined as the difference between the total flux within a bare iron wire and the total flux within a cadmium covered iron wire, the subcadmium flux can be determined as follows. The subcadmium flux can be approximated as:

$$\phi_{sc} = \int_0^\infty \phi_b(E)dE - \int_0^\infty \phi_{cd}(E)dE \qquad (3)$$

which can be rewritten as:

$$\phi_{sc} = \frac{A_b}{\sigma_{58,b}} - \frac{A_{cd}}{\sigma_{58,cd}} . \qquad (4)$$

Here the bare and cadmium covered Fe-58 cross sections are defined as follows:

$$\sigma_{58,b} = \frac{\int_0^\infty dE\sigma_{58}(E)\phi_b(E)}{\int_0^\infty dE\phi_b(E)} \qquad (5)$$

$$\sigma_{58,cd} = \frac{\int_0^\infty dE \sigma_{58}(E)\phi_{cd}(E)}{\int_0^\infty dE \phi_{cd}(E)} \qquad (6)$$

where $\phi_b(E)$ and $\phi_{cd}(E)$ are the spectra seen by a bare and cadmium covered iron wire, respectively.

This method unfortunately requires knowledge of the Fe-58 cross section, which is presently unavailable in the SCALE package of codes, and since the iron cross section is not 1/v in the epithermal region, the Fe-58 cross section cannot be determined from the total iron cross section. The bare and cadmium covered iron wires have been modelled by ANISN calculations, however, and the results are given in Table 4. The ANISN calculation assumed a .05 cm diameter of iron wire surrounded by a .1 cm diameter region of light water, surrounded by a .2 cm diameter region of cadmium, and surrounded finally by a region of either core material or heavy water.

Table 4

Bare and Cadmium Covered Iron Wire Cross Sections (barns)

| Region | $\sigma_{Fe,b}$ | $\sigma_{Fe,cd}$ |
|---|---|---|
| LEU Lattice | .533 | .0453 |
| HEU Lattice | .559 | - |
| $D_2O$-X | 1.24 | .0837 |

B. Analysis of SPND Measurements

The SPND measurements have been analyzed in a similar manner as the iron wire activations. Analysis of the

rhodium SPND measurements is complicated by two factors. First, since rhodium has a large absorption cross section, the flux is significantly perturbed by the insertion of the SPND into the core. The flux depression caused by the insertion of the rhodium SPND must be determined in order to relate SPND current measurements to subcadmium flux. Another complicating factor in the analysis of the SPND measurements is that the detector is mounted on an Inconel paddle, which also causes a significant perturbation in the flux when the detector is inserted.

Several attempts were made to model the Inconel paddle with the one-dimensional transport theory codes, ANISN and XSDRN, by cylindricizing the paddle and preserving the volume of Inconel. It was decided that it was infeasible to adequately model the complicated geometry of the Inconel paddle in this manner since the flux depression caused by the paddle depended sensitively upon the thickness of water between the SPND and the Inconel, and also upon the thickness of the Inconel paddle. It was decided to model the SPND itself, which can be modeled reasonably well in one-dimensional cylindrical geometry, and to rely upon measurements to estimate the flux depression caused by the Inconel paddle.

Given a net SPND current, $I_{net}$, the subcadmium flux can be determined as follows:

$$\phi_{sc} = \frac{I_{net} f'_{sc}}{S_{sc}} , \qquad (1)$$

where the subcadmium current fraction $f'_{sc}$ defined in Appendix A is approximated by the subcadmium activation fraction

$$f_{sc} = \frac{\int_V d\underline{r} \int_0^{E_c} dE\sigma(E)\phi_p(\underline{r},E)}{\int_V d\underline{r} \int_0^{\infty} dE\sigma(E)\phi_p(\underline{r},E)} \quad (2)$$

and $S_{sc}$ is the detector sensitivity. The detector sensitivity depends on the beta escape probability $\bar{\beta}_{sc}$, flux perturbation factor $f_p$ and the effective subcadmium cross section $\bar{\sigma}$ for Rh-103 as defined in Appendix A.

The factors $\bar{\sigma}$, $f_{sc}$ and $f_p$ have been calculated by utilizing the codes in the SCALE package. The CSAS code is used to set up the input files for the NITAWL and XSDRN codes. The SPND is modeled in cylindrical geometry with the .05 cm diameter rhodium emitter wire surrounded by the aluminum oxide insulator of .1 cm outer diameter and the Inconel collector of .16 cm outer diameter. The SPND has been modeled in surrounding environments simulating HEU fuel, LEU fuel, and heavy water tank penetration X.

The XSDRN code is used to collapse the 123-group SCALE package library to 30 groups, with the group structure in the collapsed library set up to preserve most of the detail in the vicinity of the rhodium resonance around 1.3 eV. The XSDRN code produces a set of microscopic cross sections for each isotope in each region. The ICE code is then used to perform the cross section mixing and to generate a macroscopic cross section library for use in the ANISN code. Most of the transport theory analysis of the SPND detector was performed with the ANISN code in 30 group, P-1, S-8 calculations.

The core and heavy water tank surrounding environments have been simulated in exactly the same manner as in the previous section for the analysis of the iron wire activations. The subcadmium cross sections $\bar{\sigma}$ for Rh-103 calculated by the ANISN code are given in Table 5. The cadmium

cutoff energy is taken to be .625 eV, with values at .625 eV determined by interpolating between the values at .5488 eV and at .6552 eV. The subcadmium fractions $f_{sc}$ for the SPND, calculated with the ANISN code, are compared with the experimental values also in Table 5.

Table 5

Subcadmium Cross Sections for Rhodium Wire (barns)

| Region | $\bar{\sigma}$ | $f_{sc}$ | | $f_p$ |
|---|---|---|---|---|
| | ANISN | ANISN | Measured | ANISN |
| 2200 m/s | 150 | - | - | - |
| LEU Lattice | 114 | .80 | .75 | .75 |
| HEU Lattice | 114 | .82 | .79 | .73 |
| $D_2O$-X | 120 | .90 | .90 | .72 |

The flux perturbation factors $f_p$ for the insertion of the SPND have been determined by comparing the flux in the rhodium emitter wire with the flux in the same volume with the detector removed. The flux spectra have been normalized to be the same far away from the location of the detector insertion. The flux perturbation factors are also given in Table 5. The parameters $\bar{\sigma}$, $f_{sc}$, $f_p$ and $S_{sc}$ calculated with the ANISN code compare favorably with those obtained with the VIM Monte Carlo code[10] as presented in Table II of Appendix A.

C. Simulation of Flux Maps

Figures 6.A, 7.A and 8.A compare the absolute subcadmium fluxes determined from SPND measurements with those determined from 2DB-UM[11] calculations for an equilibrium HEU core, a nearly fresh LEU core, and a mixed HEU-LEU core. SPND current measurements have been converted to subcadmium fluxes by the methods described in Section III.B of this

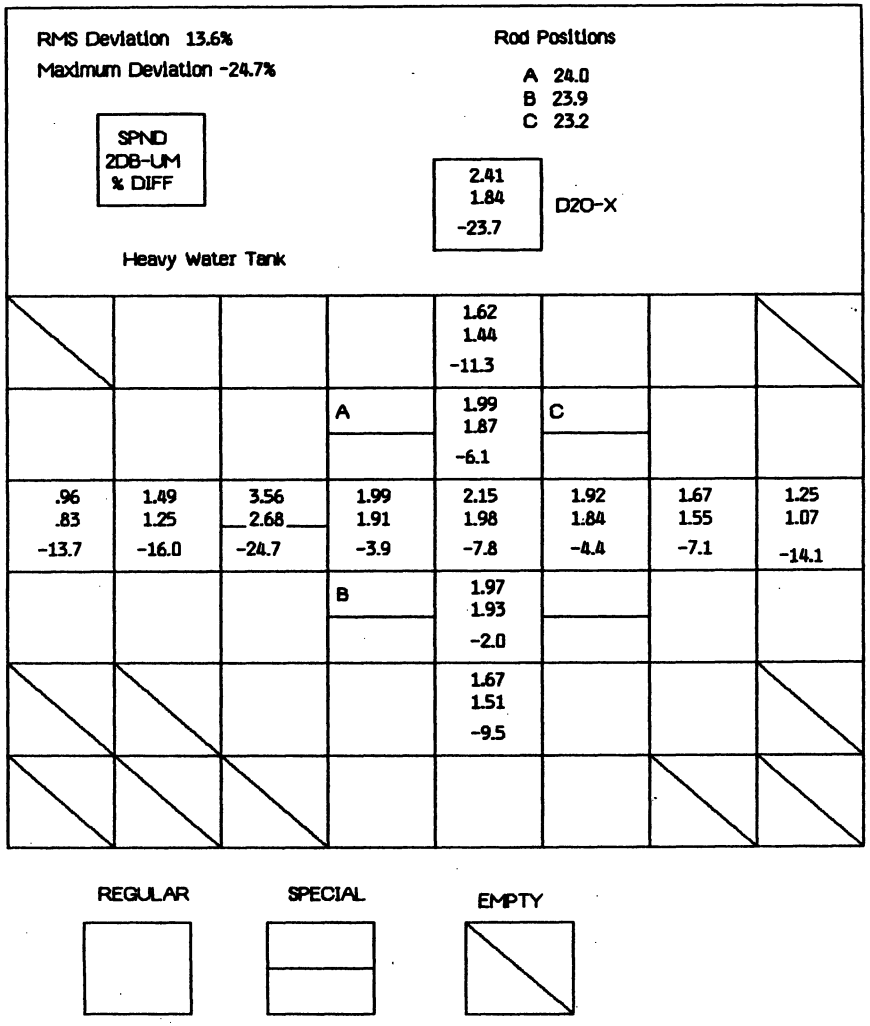


Figure 6.A SPND and 2DB-UM Absolute Subcadmium Fluxes - 5/29/82 HEU Core

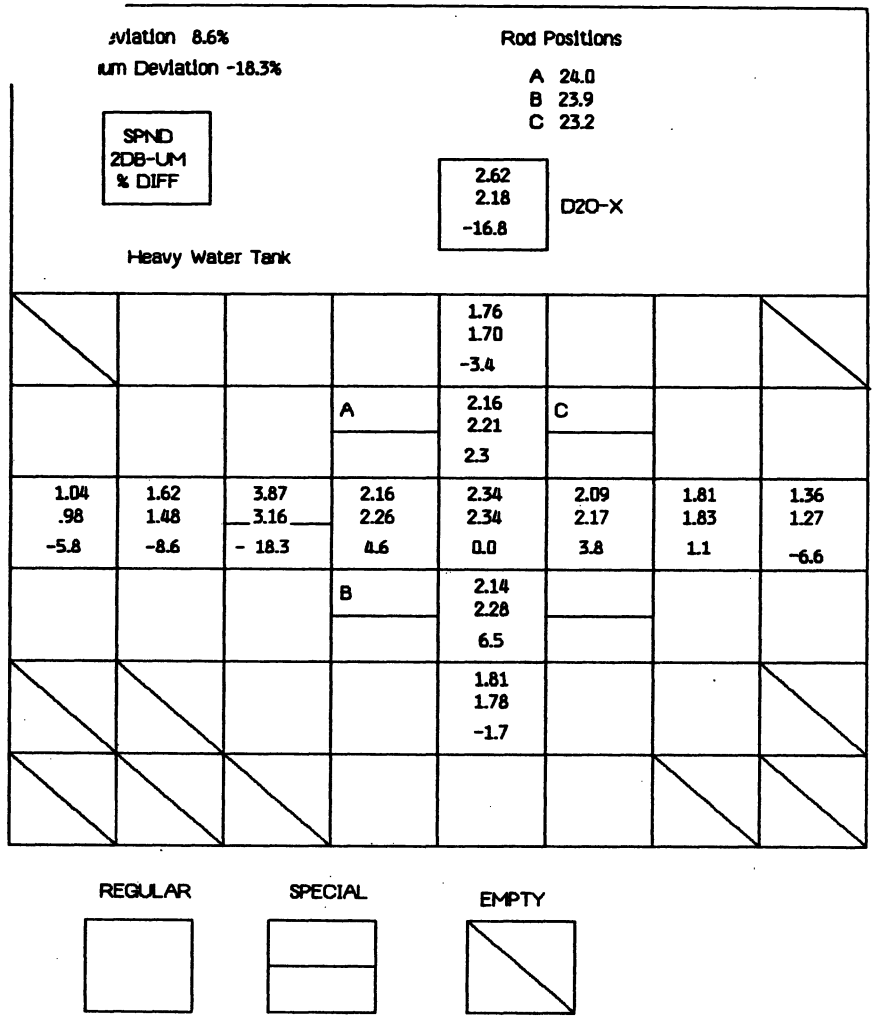


Figure 6.B SPND and 2DB-UM Absolute Subcadmium Fluxes Normalized to Iron Wire at L-37 - 5/29/82 HEU Core

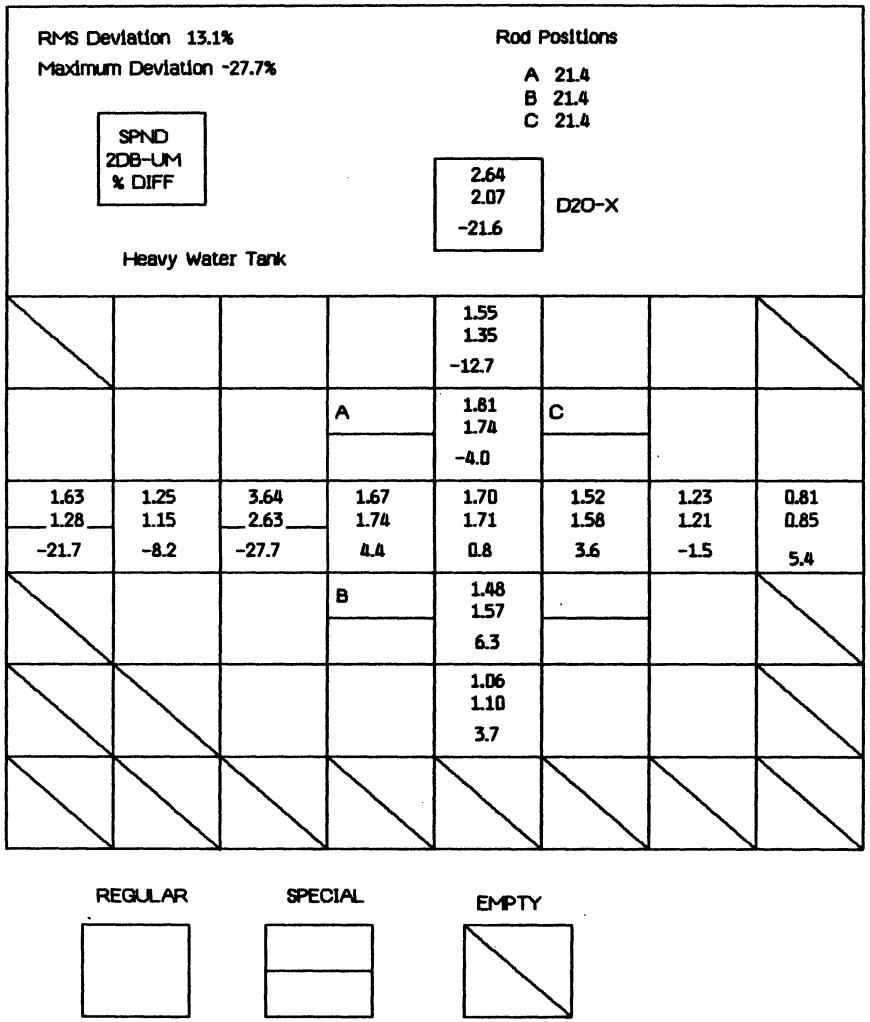


Figure 7.A SPND and 2DB-UM Absolute Subcadmium Fluxes - 9/16/83 LEU Core

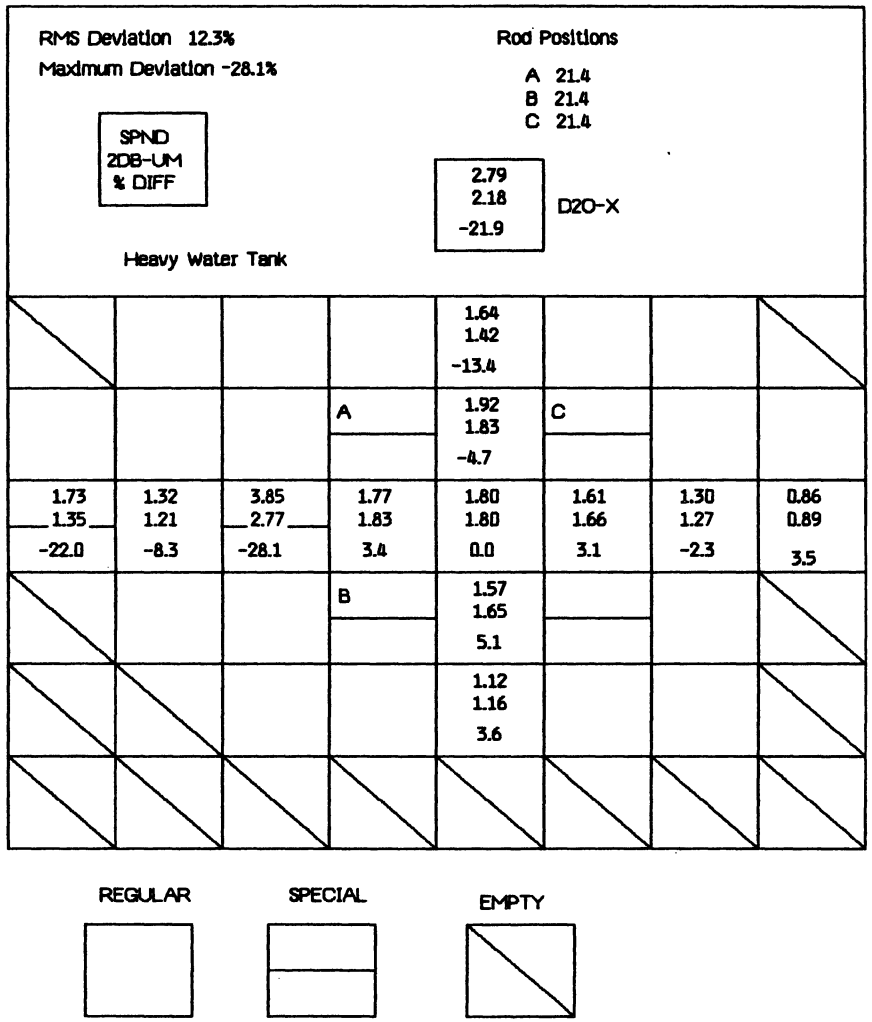


Figure 7.B SPND and 2DB-UM Absolute Subcadmium Fluxes Normalized to Iron Wire at L-37 - 9/16/83 LEU Core

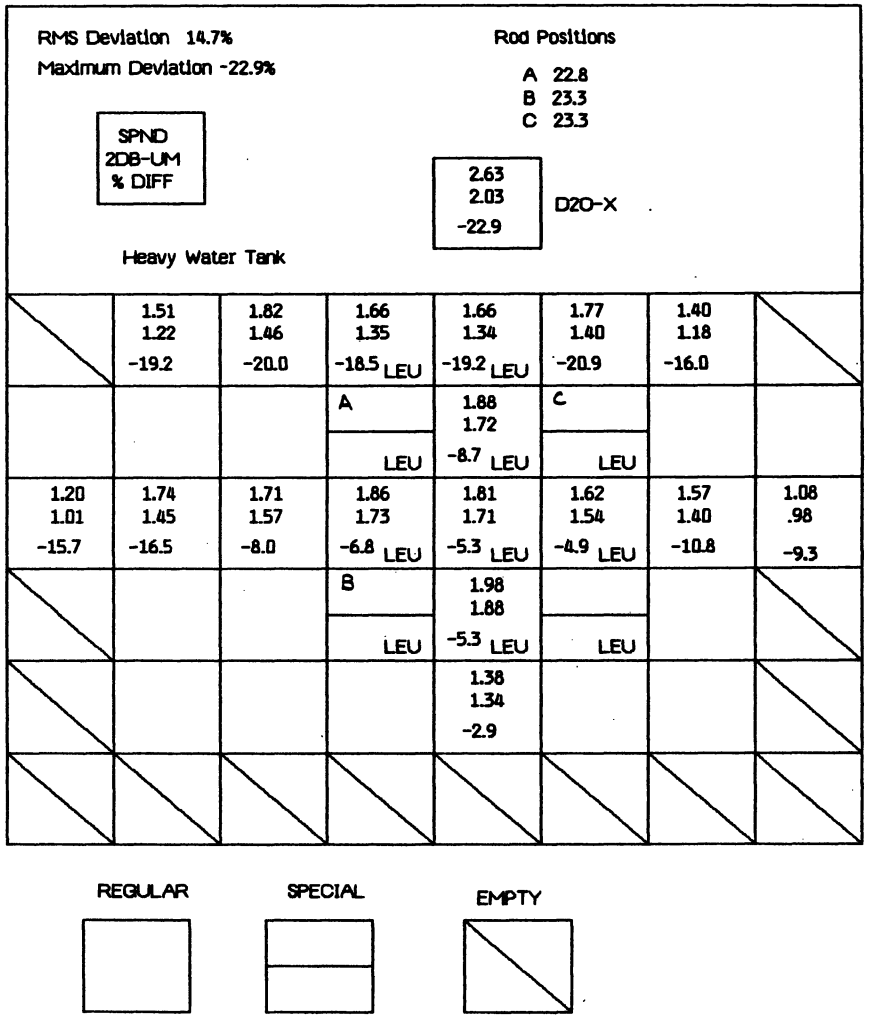


Figure 8.A SPND and 2DB-UM Absolute Subcadmium Fluxes - 10/5/83 Mixed Core

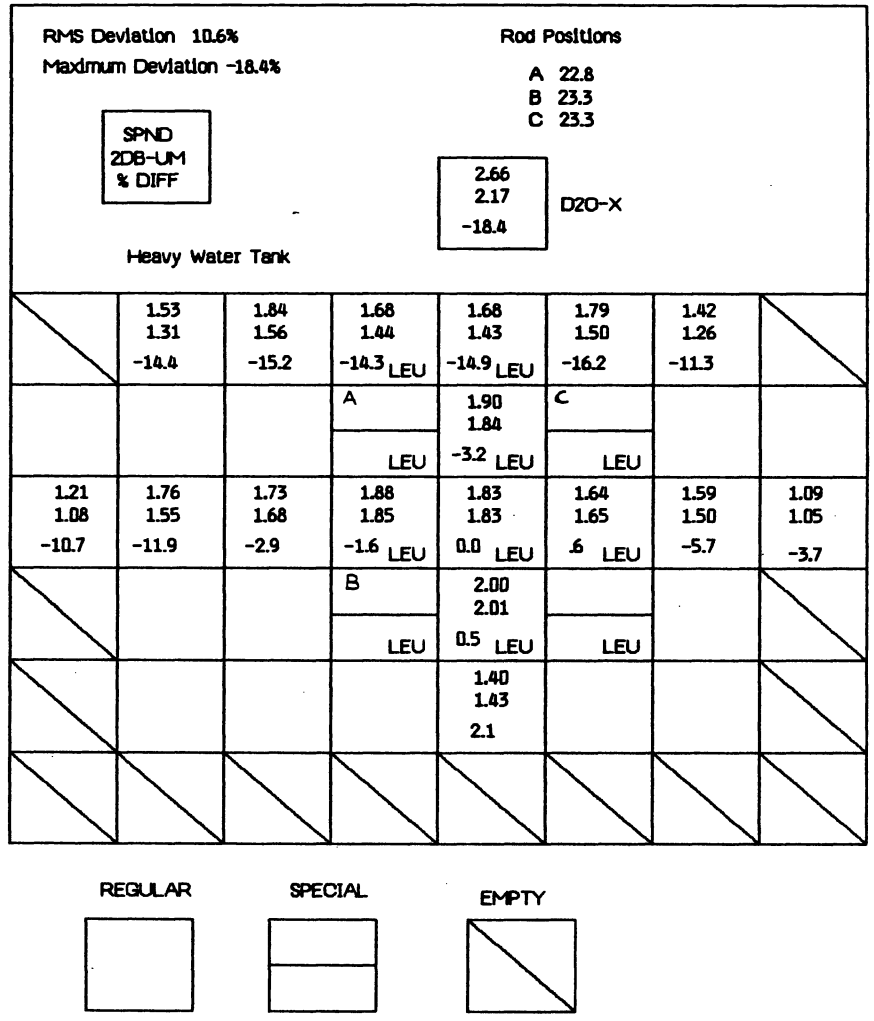


Figure 8.B SPND and 2DB-UM Absolute Subcadmium Fluxes Normalized to Iron Wire at L-37 - 10/5/83 Mixed Core

report. The SPND measurements have been made at a quarter core height.

Absolute subcadmium fluxes for comparison have been determined from 2DB-UM calculations as follows. The 2DB-UM code computes absolute subcadmium fluxes corresponding to an input linear power generation rate. The total power of the FNR is 2 MW and the core height is 23.5 inches, which corresponds to an average linear power generation rate of .0335 MW/cm. In order to convert the average flux to quarter core height flux, the ratio of the quarter core height flux to the average axial flux has been determined from iron wire activation measurements as reported in Ref. 2. This was nearly a 5% correction. The 2DB-UM calculations assumed a cadmium cutoff energy of .625 eV and a fission energy of 195 MeV/fission.

Two additional correction factors were included to compare the measured and calculated fluxes. The flux depression due to the Inconel paddle surrounding the SPND was experimentally determined to be 7%. The subcadmium flux peaking in the light water tube penetration into the heavy water tank was calculated by means of the ANISN code to be 10%. With these corrections, the measured and calculated fluxes are compared in Figures 6.A through 8.A. In order to better compare the results, the SPND and 2DB-UM absolute subcadmium fluxes have been normalized to the iron wire measurements at the core center (L-37). These results are presented in Figures 6.B through 8.B. Compared with the SPND measurements it is evident that the 2DB-UM calculated flux is tilted away from the vicinity of the $D_2O$ tank and west side of the core.

D. Non-Lattice Peaking Factor Calculation

Earlier calculations[1] have been made for the non-lattice peaking factor (NLPF) to be used as input for the LEOPARD code[12]. A fine-mesh (63x38) two-dimensional 2DB-UM calculation for a 1/4-assembly HEU special element yielded a

NLPF of 1.16. This value was subsequently used for LEOPARD analysis of LEU special elements.

Three new fuel geometries have been examined with 2DB-UM. They include: (1) the initial, clean LEU critical core of December, 1981, (2) a single LEU special element surrounded by 1/2-LEU regular elements on the sides and 1/4-LEU regular elements on the corners, and (3) a single LEU special element. Based on these calculations, a NLPF=1.35 was obtained for generation of new LEOPARD cross sections for LEU special elements. Repeating these calculations for geometries (2) and (3) with LEU elements replaced by HEU elements yields a NLPF=1.29 for HEU special elements. With the new library, the LEU critical configuration of December, 1981, was reexamined using both a 2x2 and 6x6 mesh structure. As seen in Figure 9, the new LEOPARD cross sections with NLPF=1.35 reduce the RMS difference in power fraction between the 2x2 and 6x6 mesh 2DB-UM calculations from 5.88% to 3.84%. The relative difference for shim rod C is reduced from 11.7% to 5.0%. Table 6 shows the effect of the cross section set on the calculated core eigenvalue. Using the new LEOPARD library yields a core eigenvalue of 1.0068 for the 2x2 mesh calculation, which agrees quite well with the value of 1.0071 for the 6x6 mesh. It is also noticed that the NLPF negligibly affects the core eigenvalue calculated with the 6x6 mesh geometry.

E. FNR Fuel Burnup Calculations

Four years of FNR cycles (141 cycles: September, 1979, through September, 1983) have been simulated with the 2DB-UM code with a 2x2 coarse-mesh description. This fuel burnup updating covers both HEU and LEU core configurations. Revisions to the FNR burnup data processing codes (SORT/UPSORT) permit correct burnup computations for any combination of in-core or ex-core residence times for any type of fuel element. The 2DB-UM calculation utilizes the latest ENDF/B-IV library (including the new fission product correlation and

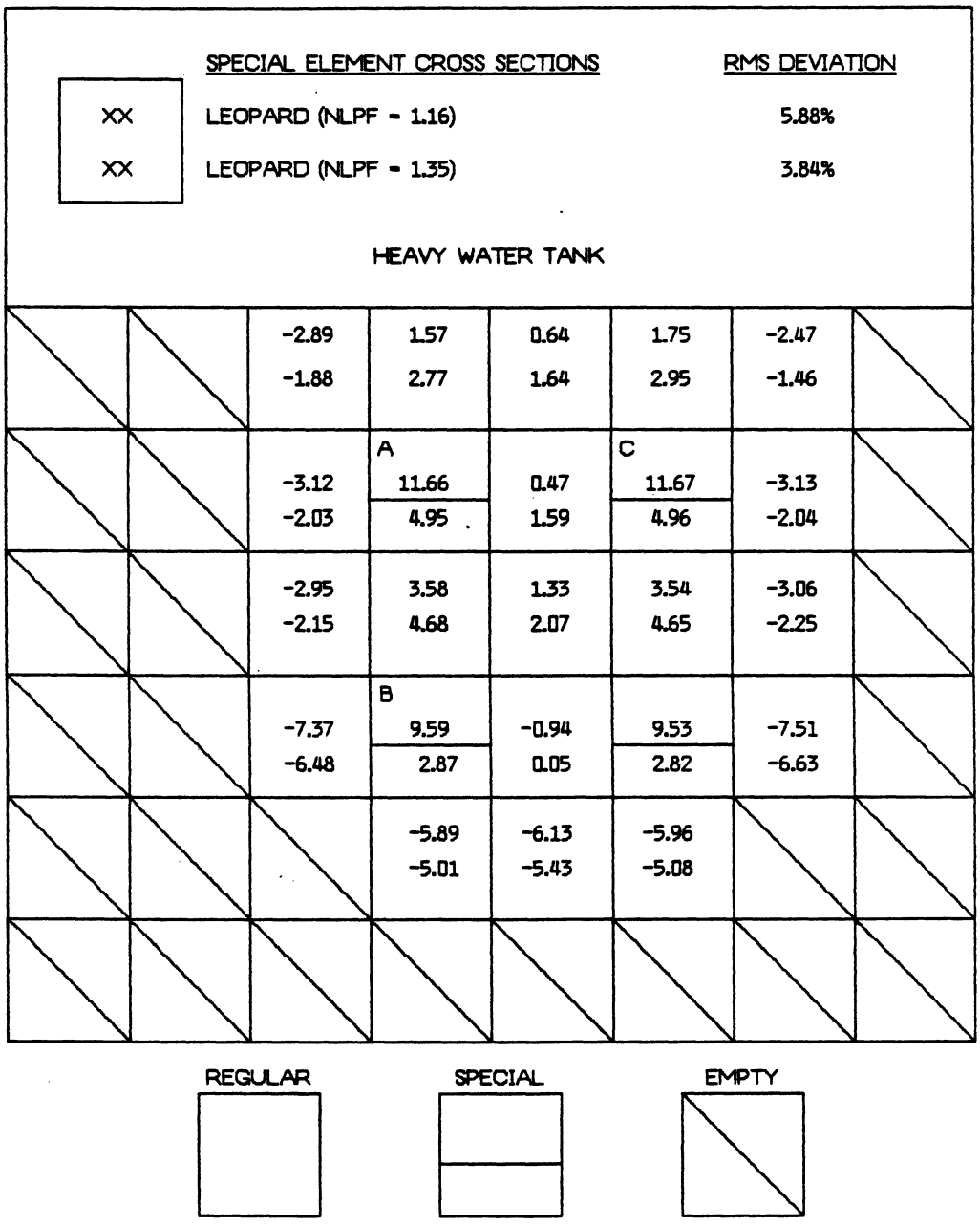


Figure 9 Relative Error in 2DB-UM Calculated Power Fractions for 2x2 Mesh versus 6x6 Mesh - December 1981 Critical LEU Core

Table 6

Effect of NLPF on Core Eigenvalue

| Cross Sections Used for Special Elements | Core Eigenvalue - 12/81 LEU Critical | |
|---|---|---|
| | 2x2 Mesh | 6x6 Mesh |
| LEOPARD (NLPF=1.16) | 1.0117 | 1.0069 |
| LEOPARD (NLPF=1.35) | 1.0068 | 1.0071 |

non-lattice peaking factors for special elements) and the XSDRN-calculated $D_2O$ cross sections discussed in Section IV.B. The comparisons of 2DB-UM power distributions in Figure 9 with a 2x2 and 6x6 mesh structure for the initial, clean LEU core of December, 1981, illustrate the general adequacy of the coarse-mesh structure in predicting fuel burnup as compared with the 6x6 structure.

F. 2DB-UM Eigenvalue Calculations for FNR Core

Based on the fuel burnups calculated by 2DB-UM, several FNR core configurations were examined using a 6x6 structure 2DB-UM calculation. Table 7 gives the comparison between the measured core eigenvalue and the calculated core eigenvalue using both 2DB-UM predicted masses and the masses predicted by the FNR burnup code, which uses an empirical expression for the FNR flux distribution. Table 7 updates the earlier 2DB-UM FNR eigenvalue calculations presented in Appendix B performed with FNR calculated fuel burnups and the ENDF/B-IV library with old NLPFs.

Before determining the absolute bias between the calculated and measured eigenvalues, two corrections must be made to some of the calculations. First, 2DB-UM performs the calculation assuming the core is at full-power. In the case of a critical loading, the eigenvalue is measured at zero-power. Therefore, a power defect correction of -0.23 $\%\Delta k/k$

Table 7

2DB-UM FNR Eigenvalue Calculations

| Core | Average Burnup (%) | | Measured $\rho_{ex}$ (%Δk/k) | 2DB-UM Eigenvalue | | Absolute Bias (%Δk/k) | |
|---|---|---|---|---|---|---|---|
| | FNR[1] | 2DB[2] | | FNR | 2DB | FNR | 2DB |
| Dec, 1981 Critical LEU | 0.00 | 0.00 | 0.45 | 1.0040 | 1.0040 | -.28[3] | -.28[3] |
| May, 1982 Full Power HEU | 13.76 | 14.36 | 3.29 | 1.0499 | 1.0464 | 1.33[4] | 1.01[4] |
| March, 1983 Critical Mixed | 12.13 | 13.14 | 0.10 | 1.0140 | 1.0101 | 1.05[3] | .67[3] |
| June, 1983 Critical LEU | 3.03 | 2.96 | 0.00 | 1.0046 | 1.0048 | .10[3,4] | .12[3,4] |
| June, 1983 Full Power LEU | 3.48 | 3.42 | 3.29 | 1.0365 | 1.0366 | .11[3,4] | .11[3,4] |
| Oct, 1983 Full Power Mixed | 12.65 | 13.31 | 3.02 | 1.0388 | 1.0364 | .59[4] | .36[4] |

[1] FNR calculated fuel burnup

[2] 2DB calculated fuel burnup

[3] Corrected for power defect, $\rho_{PD}$ = -.23 (%Δk/k)

[4] Corrected for samarium reactivity, $\rho_{Sm}$ = -.13 (%Δk/k)

(as measured for the August, 1983, LEU core) has been applied to these cases. Second, post-shutdown samarium build-up is not handled in 2DB-UM calculations. The effect of this limitation on the calculated core eigenvalue was examined by simulating the actual history of LEU fuel elements with the LEOPARD code. For the June, 1983, LEU configuration of the FNR core, it is estimated that the samarium reactivity at the beginning of the cycle is 0.13 %Δk/k. This correction factor has also been applied to the calculated eigenvalues for the May, 1982, HEU core and the October, 1983, Mixed core.

Regardless of the fuel burnup model used, these 2DB-UM calculations indicate a substantially higher eigenvalue bias for the configurations containing highly depleted HEU fuel elements than for LEU configurations with fresh or slightly depleted fuel elements. However, using 2DB burnups reduces the absolute bias by about 0.31 %Δk/k for the HEU and Mixed cores as compared with those based on FNR burnups. The variation in fuel burnups calculated by 2DB and by FNR has a minimal effect on the core eigenvalue calculated for the June, 1983, cores due to a relatively low burnup in the LEU fuel. Overall, the core eigenvalues calculated using 2DB burnups indicate a bias in the range -0.3 to +1.0 %Δk/k.

## G. Control Rod Worth Calculations

As reported in Ref. 3, the control rod worth calculations, especially for rod B, were found to be sensitive to the cross sections used for the heavy water tank. This section of the report gives the results of control rod worth calculations with the improved heavy water cross sections given in Section IV.B of this report. The rod worth calculations are compared with measurements for an HEU core, an LEU core, and a mixed HEU-LEU core.

The rod worths are calculated by computing the reactivity difference between a rod-in case and a rod-out case. The calculations are done with the 2DB-UM code with 6x6

meshes per assembly with the control rod cross sections obtained with the EPRI-HAMMER[13] and TWOTRAN[14] codes, as discussed in earlier reports.[1,2]

The rod worths are determined experimentally by measuring the worth of one half of a rod, and multiplying the result by a factor of 2. Several full-length rod worth measurements have been made with the ratio of the full-length rod worth to the half-length rod worths given in Table 8. Since full-length rod worth measurements involves considerable perturbation in the flux distribution due to swapping of shim rods, measured full-length worths are not directly used in our simulation. The extrapolated full-length rod worth data are compared with 2DB-UM calculations for three cores in Table 9. The calculations made use of both the improved heavy water cross sections determined by means of the XSDRN code as discussed in Section IV.B and the special element cross sections obtained from the LEOPARD code using the updated non-lattice peaking factors. The agreement between the measured and calculated rod worths is much better than that reported previously in Appendix B.

Table 8

Ratio of Full- to Half-Length Rod Worth

| Core | Rod | Ratio |
|---|---|---|
| 8/18/82 HEU | C | 1.88 |
| 6/21/83 LEU | A | 1.89 |
| | B | 1.90 |
| | C | 1.99 |

H. October 1983 Mixed Critical Loading

In preparation for the October 3, 1983, loading of a mixed HEU-LEU core, fuel loading calculations and rod worth

Table 9

Control Rod Worths

| Core | Rod | Measured Half-Rod | Extrapolated Full-Rod | 2DB-UM Calculated | Relative Error (%) |
|---|---|---|---|---|---|
| 9/26/82 HEU | A | 1.25 | 2.50 | 2.41 | -3.6 |
| | B | 1.06 | 2.12 | 2.04 | -3.8 |
| | C | 1.18 | 2.36 | 2.16 | -8.5 |
| 7/8/83 LEU | A | 1.42 | 2.84 | 2.72 | -4.2 |
| | B | 1.16 | 2.32 | 2.26 | -2.6 |
| | C | .955 | 1.91 | 1.75 | -8.4 |
| 10/3/83 Mixed | A | 1.36 | 2.72 | 2.66 | -2.2 |
| | B | 1.07 | 2.14 | 2.16 | 0.9 |
| | C | 1.08 | 2.16 | 1.97 | -8.8 |

calculations were performed with the 2DB-UM code (utilizing FNR burnups, the LEOPARD library with old NLPFs for the special elements and LEOPARD ex-core cross sections) to predict a full-power core configuration which would satisfy required shutdown margins. The biases in the core eigenvalue and rod worths obtained with the 2DB-UM code were estimated by comparing measured excess reactivity and rod worths for the April 12, 1983, mixed core with 2DB-UM calculations. Based on a bias factor of 0.86 %Δk/k in core eigenvalue, a 35-element core was expected to yield a 2.78 %Δk/k excess reactivity. In reality, a 34-element core consisting of 23 HEU regular, seven LEU regular, and four LEU special elements was loaded giving an excess reactivity of 3.02 %Δk/k. Repeating the 2DB-UM calculations for the actual core configuration using 2DB burnups and the new LEOPARD library gives an excess reactivity of 3.38 %Δk/k.

Several 2DB-UM calculations were performed to investigate the effect on the global flux distribution of replacing HEU special elements with LEU special elements at the control rod locations. Figures 10 and 11 compare the

respective south-north and east-west flux distributions through lattice position L-37 at the core center with HEU and LEU special elements at the control rod locations. The calculations indicate that a HEU special/LEU special exchange has a minimal affect on the flux distribution in the core.

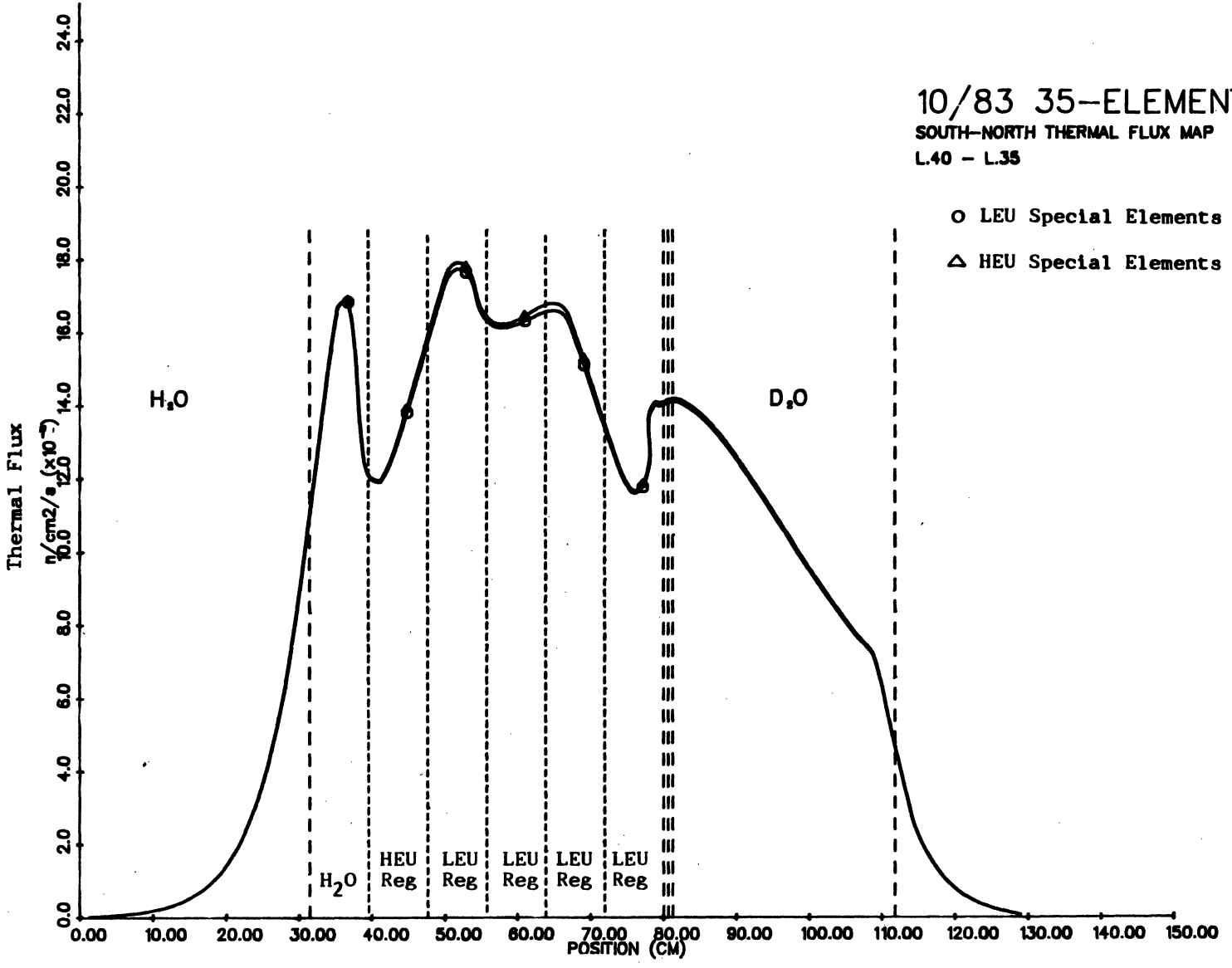


Figure 10 2DB-UM South-North Flux Distribution for the October 1983 Mixed Core

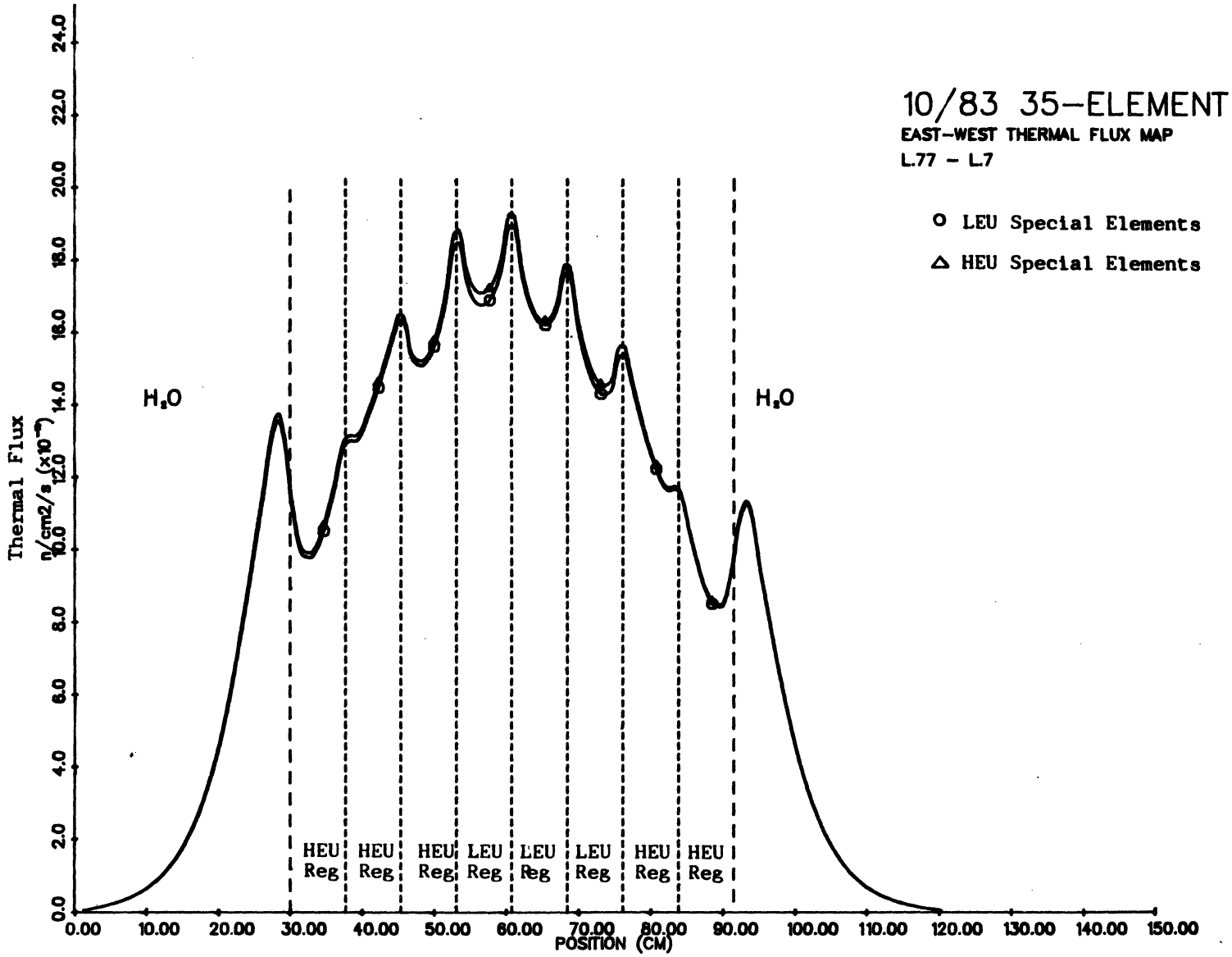


Figure 11 2DB-UM East-West Flux Distribution for the October 1983 Mixed Core

# IV. GENERIC METHODS DEVELOPMENT AND VERIFICATION

## A. IAEA Benchmark Calculation

This section discusses the results of using the University of Michigan (UM) reactor analysis code package to analyze the IAEA research reactor benchmark problem[15]. This benchmark problem was developed at the Consultants Meeting on "Preparation of a Programme on Research Reactor Core Conversions to Use LEU instead of HEU", IAEA, June 19-22, 1979 in Vienna, Austria. Its detailed specifications are given in Table 10 and in Figure 12. Briefly, it corresponds to a 10 MWth, 6X5 element core at several uniform depletion stages. The reactor core is reflected by graphite on two opposite sides and surrounded by light water. Standard MTR elements with 23 fuel plates are utilized, with uranium enrichments of 93%, 45% and 20%, corresponding to a U-235 content of 280, 320, and 390 grams per element, respectively. This benchmark problem has already been calculated by seven international research centers and their results are summarized in Ref. 15. Although we have obtained results only for the HEU case, the analysis model and procedure remain the same for the MEU and LEU cases.

### 1. Fuel and Control Element Cross Section Calculations

Macroscopic cross sections were generated as a function of burnup (in percentage loss of the number of U-235 atoms) by the LEOPARD code with the ENDF/B-IV library. The unit cell geometries for LEOPARD are based on the specifications given in Table 10. Figure 13 illustrates the unit cell geometries for both the fuel element and the control elements. The extra regions (or "non-lattice" regions) in Figure 13 for both the fuel element and the control element include the aluminum in the fuel plates beyond the width of the fuel meat, the water beyond the width of the fuel meat, the aluminum support plates, and the water surrounding the fuel element. Moreover, the non-lattice region for the control element includes the central water channel for the con-

# Table 10

## Specifications for the IAEA Research Reactor Benchmark Problem

**Aims:** Comparison of the different calculation methods and cross-section data sets used in different laboratories, limited conclusions for real conversion problems.

Specifications for the Methodical Benchmark-Problem

Data and Specifications Agreed Upon:

Active Core Height 600 mm
Extrapolation Length 80 mm (in 80 mm distance from the core, the cosine-shaped flux goes to zero)
X-Y Calculations only

Space at the grid plate per fuel element 77 mm x 81 mm

Fuel element cross-section
76 mm x 80.5 mm including support plate
76 mm x 80.0 m without support plate

Meat dimensions
63 mm x 0.51 mm x 600 mm

Aluminum-canning with $\rho_{Al} = 2.7\ g \cdot cm^{-3}$

Thickness of support plate 4.75 mm; $\rho_{Al} = 2.7\ g \cdot cm^{-3}$

Number of fuel plates per fuel element:
23 identical plates, each 1.27 mm thick

Number of fuel plates per control element:
17 identical plates, each 1.27 mm thick

Identification of the remaining plate positions of the control element:
4 plates of pure aluminum $\rho_{Al} = 1.7\ g \cdot cm^{-3}$, each 1.27 mm thick in the position of the first, the third, the twenty-first, and the twenty-third standard plate position; water gaps between the two sets of aluminum plates.

Specifications of the different fuels ($UAl_x$-Al Fuel) for HEU, MEU, LEU corresponding to the previous definitions:

HEU:
- Enrichment 93 w/o (weight %) U-235
- 280 g U-235 per fuel element, which corresponds to 12.174 g U-235 per each fuel plate
- 21 w/o of uranium in the $UAl_x$-Al
- only U-235 and U-238 in the fresh fuel

MEU:
- Enrichment 45 w/o U-235
- 320 g U-235 per fuel element (23 plates)
- 40 w/o of uranium in the $UAl_x$-Al
- only U-235 and U-238 in the fresh fuel

LEU:
- Enrichment 20 w/o U-235
- 390 g U-235 per fuel element (23 plates)
- 72 w/o of uranium in the $UAl_x$-Al
- only U-235 and U-238 in the fresh fuel

Total power: 10 $MW_{th}$ (power buildup by $3.1 \times 10^{10}$ fission/Joule)

Thermal hydraulic data:
Water temperature 20°C
Fuel temperature 20°C
Pressure at core height 1.7 bar

Xenon-State:
Homogeneous Xenon content corresponding to average-power-density

Results

$k_{eff}$; fluxes and flux ratios along the two symmetry-axes of the core in three groups and for begin of cycle (BOL) and end of cycle (EOL), respectively.

$\phi_{thermal}$ with $0\ eV < E_n < 0.625\ eV$

$\phi_{epithermal}$ with $0.625\ eV < E_n < 5.531\ keV$

$\phi_{fast}$ with $E_n > 5.531\ keV$

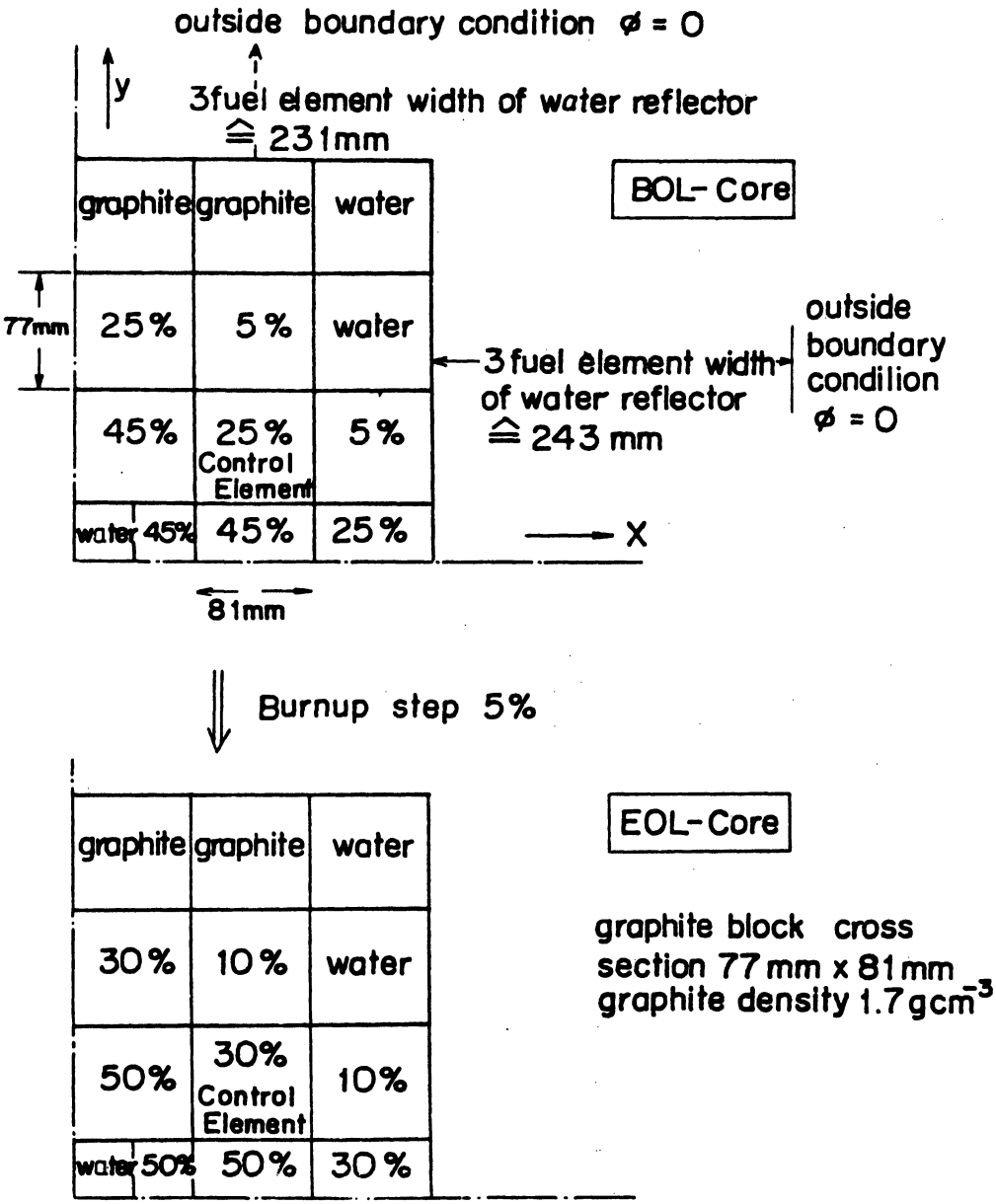


Burnup definition : (%) means the percentage of loss of the number of U 235 - Atoms

METHODICAL BENCHMARK
10 MW CASE
CORE CROSS SECTION

Figure 12 Core Cross Section for the IAEA Research Reactor Benchmark Problem

trol rod as well as the aluminum side plates forming the channel.

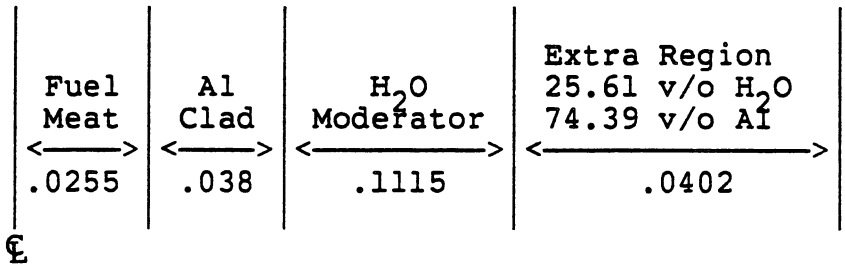


Fuel Element (cm)

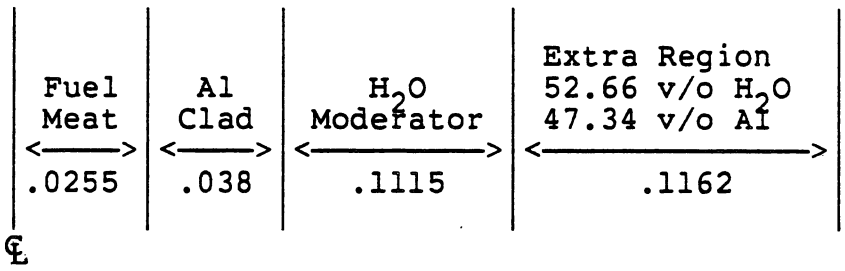


Control Element (cm)

Figure 13. Fuel and Control Element Unit Cell Geometries Used for LEOPARD Calculations

Table 11 presents the infinite multiplication factors for the fuel element as a function of U-235 burnup. The table includes results obtained by LEOPARD and by Argonne National Laboratory (ANL). The LEOPARD code uses the ENDF/B-IV library and includes a fission product correlation based on the CINDER code[16].

The data in Table 11 are plotted in Figure 14. It is evident that the LEOPARD results agree very well with the ANL predictions. This comparison seems reasonable because CINDER was utilized by ANL for burnup. Therefore, LEOPARD was used to generate the 2-group cross section libraries for both the fuel element and the control element. An earlier ENDF/B-IV version of LEOPARD with an old fission product

Table 11

Infinite Multiplication Factor for HEU Fuel versus U-235 Burnup

| U-235 Burnup (%) | Infinite Multiplication Factor | |
|---|---|---|
| | LEOPARD[1] | ANL |
| 0.0 | 1.7432 | 1.7370 |
| 5.0 | 1.6427 | 1.6370 |
| 10.0 | 1.6203 | 1.6165 |
| 15.0 | 1.5979 | 1.5953 |
| 20.0 | 1.5745 | 1.5728 |
| 25.0 | 1.5494 | 1.5485 |
| 30.0 | 1.5225 | 1.5223 |
| 35.0 | 1.4932 | 1.4936 |
| 40.0 | 1.4608 | 1.4620 |
| 45.0 | 1.4247 | 1.4269 |
| 50.0 | 1.3842 | 1.3876 |

[1] ENDF/B-IV with fission product correlation based on CINDER.

correlation tended to underestimate the infinite multiplication factor compared with the ANL result, as seen in Figure 14.

In addition to the comparison of $k_\infty$, comparisons have been made for the predicted atom densities in the fuel meat of the fuel element for the LEOPARD calculation as a function of U-235 burnup. The results are tabulated in Table 12, along with the results calculated by ANL. As can be seen, the LEOPARD results compare very well with the ANL results.

2. Reflector Cross Section Calculations

Separate LEOPARD calculations were performed to generate the macroscopic cross sections for the light water reflector, the central flux trap and the graphite reflector. The problem configuration and the corresponding unit cell used in these LEOPARD calculations are shown in Figure 15.

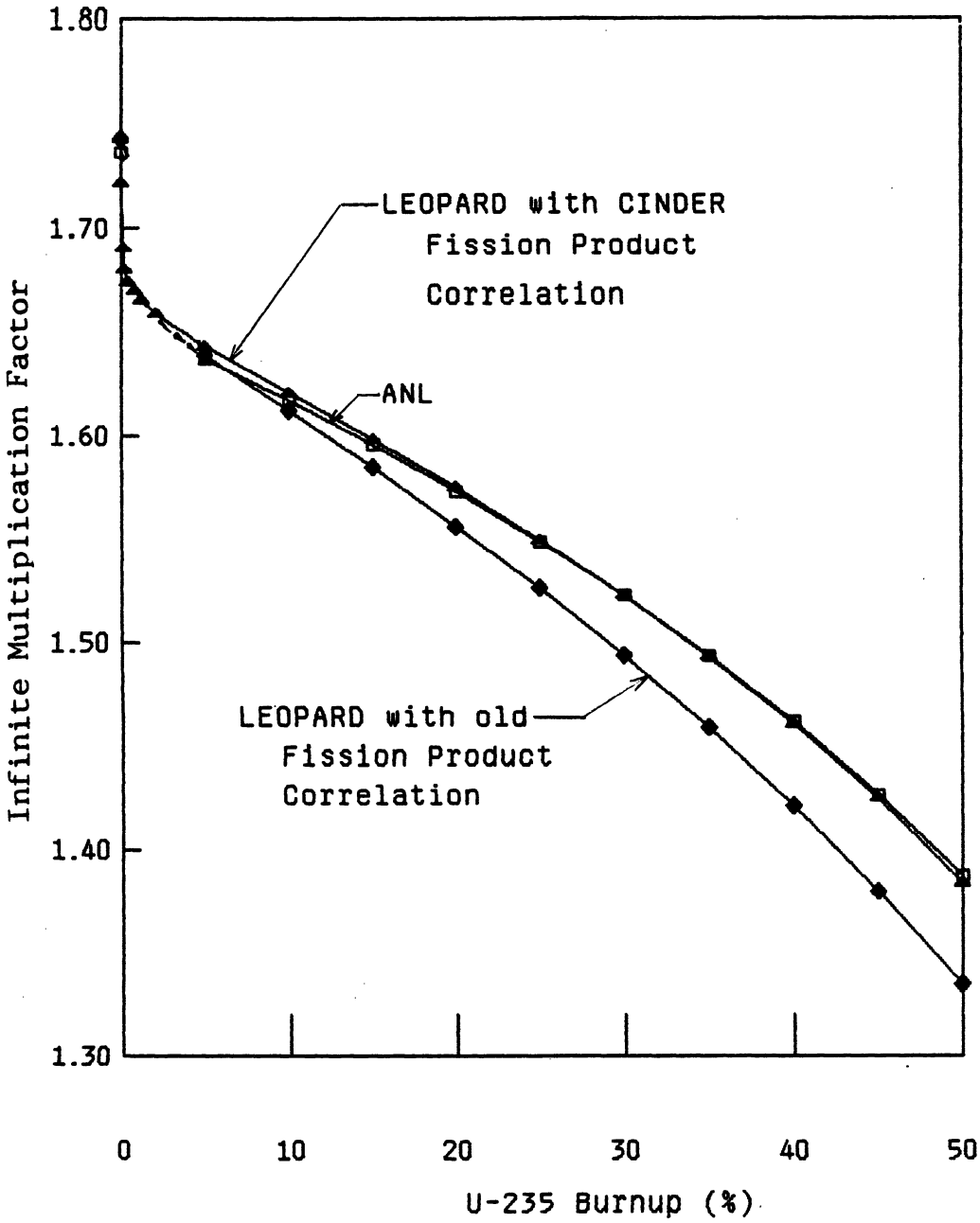


Figure 14 Infinite Multiplication Factor for HEU Fuel versus U-235 Burnup

Table 12

Atom Densities in the Fuel Meat versus U-235 Burnup

| U-235 Burnup (%) | Atom Densities $(b\text{-}cm)^{-1}$ | | | | | | | |
|---|---|---|---|---|---|---|---|---|
| | Xe-135 | Sm-149 | U-235 | U-236 | U-238 | Pu-239 | Pu-240 | Pu-241 |
| | | | | LEOPARD | | | | |
| 0.0 | 0.0 | 0.0 | 1.6179E-3 | 0.0 | 1.2020E-4 | 0.0 | 0.0 | 0.0 |
| 5.0 | 1.7072E-8[1] | 1.4167E-7 | 1.5370E-3 | 1.3485E-5 | 1.1973E-4 | 4.4223E-7 | 8.2701E-9 | 1.4831E-10 |
| 10.0 | 1.6472E-8 | 1.3831E-7 | 1.4560E-3 | 2.6911E-5 | 1.1923E-4 | 8.5342E-7 | 3.1717E-8 | 2.1173E-9 |
| 25.0 | 1.4095E-8 | 1.1567E-7 | 1.2134E-3 | 6.6279E-5 | 1.1769E-4 | 1.8227E-6 | 1.6748E-7 | 3.6986E-8 |
| 30.0 | 1.3279E-8 | 1.0815E-7 | 1.1324E-3 | 7.9144E-5 | 1.1716E-4 | 2.0612E-6 | 2.2867E-7 | 6.0327E-8 |
| 45.0 | 1.0760E-8 | 8.5706E-8 | 8.8971E-4 | 1.1677E-4 | 1.1549E-4 | 2.5373E-6 | 4.3137E-7 | 1.7023E-7 |
| 50.0 | 9.8972E-9 | 7.8257E-8 | 8.0880E-4 | 1.2900E-4 | 1.1490E-4 | 2.6169E-6 | 5.0156E-7 | 2.1671E-7 |
| | | | | ANL | | | | |
| 0.0 | 0.0 | 0.0 | 1.6179E-3 | 0.0 | 1.2020E-4 | 0.0 | 0.0 | 0.0 |
| 5.0 | 1.7094E-8 | 1.3393E-7 | 1.5370E-3 | 1.3468E-5 | 1.1973E-4 | 4.3769E-7 | 8.5690E-9 | 3.7780E-10 |
| 10.0 | 1.6416E-8 | 1.2824E-7 | 1.4561E-7 | 2.6885E-5 | 1.1923E-4 | 8.4775E-7 | 3.3247E-8 | 2.9955E-9 |
| 25.0 | 1.4034E-8 | 1.0755E-7 | 1.2134E-3 | 6.6298E-5 | 1.1768E-4 | 1.8002E-6 | 1.7889E-7 | 3.9914E-8 |
| 30.0 | 1.3219E-8 | 1.0069E-7 | 1.1325E-3 | 7.9139E-5 | 1.1715E-4 | 2.0304E-6 | 2.4357E-7 | 6.4686E-8 |
| 45.0 | 1.0709E-8 | 8.0131E-8 | 8.8985E-4 | 1.1672E-4 | 1.1546E-4 | 2.4799E-6 | 4.5967E-7 | 1.7615E-7 |
| 50.0 | 9.8497E-9 | 7.3282E-8 | 8.0895E-4 | 1.2890E-4 | 1.1486E-4 | 2.5535E-6 | 5.3381E-7 | 2.2312E-7 |

(1) Read as $1.7072 \times 10^{-8}$

The macroscopic cross sections for these regions are taken from the non-lattice edits (corresponding to the extra region in Figure 15) of LEOPARD and are assumed to be independent of burnup. Both 3-group and 2-group cross sections are given in Table 13.

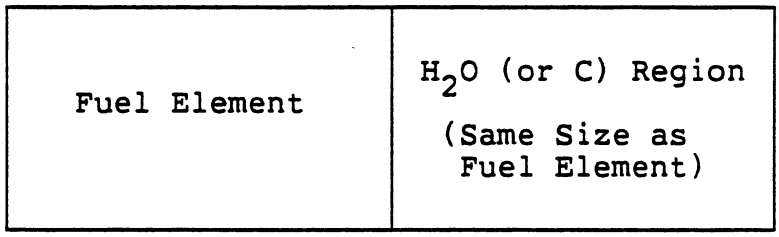


Problem Cross Section

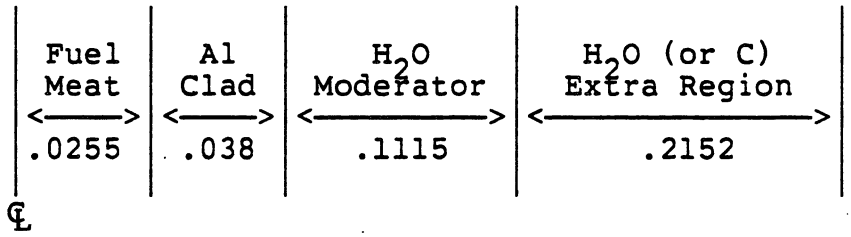


Unit Cell (cm)

Figure 15. Reflector Unit Cell Geometry Used for LEOPARD Calculations

We have also run the 1-D discrete ordinates codes XSDRN-PM and ANISN for the global 1-D (i.e. Y-direction in Figure 12) core calculations to generate another set of macroscopic cross sections for the reflectors. The results from these calculations are also given in Table 13. For the treatment of anisotropic scattering, a P-1 model was used in these calculations, based on earlier calculations which indicated very little difference between the P-1 and P-3 calculations.

The results calculated by ANL (for 3-group) and by Switzerland EIR (for 2-group) are also included in Table 13.

Table 13. 2- and 3-Group Ex-core Cross Section Comparison

| Model | Light Water Reflector | | | | | | | | | |
|---|---|---|---|---|---|---|---|---|---|---|
| | Group 1 | | Group 2 | | Group 1[4] | | Group 2 | | Group 3 | |
| | D | $\Sigma_a$ | D | $\Sigma_a$ | D | $\Sigma_a$ | D | $\Sigma_a$ | D | $\Sigma_a$ |
| XSDRN-PM[1] | 1.121 | 5.182E-4[5] | 0.153 | 1.872E-2 | 1.502 | 1.960E-4 | 0.561 | 1.019E-3 | 0.153 | 1.872E-2 |
| ANISN[2] | 0.824 | 5.183E-4 | 0.129 | 1.872E-2 | 1.186 | 1.960E-4 | 0.559 | 1.020E-3 | 0.129 | 1.872E-2 |
| LEOPARD[3] | 1.154 | 4.231E-4 | 0.168 | 1.800E-2 | 1.402 | 2.029E-4 | 0.597 | 0.918E-3 | 0.168 | 1.800E-2 |
| ANL | - | - | - | - | 1.729 | 2.271E-4 | 0.569 | 1.002E-3 | 0.147 | 1.901E-2 |
| SWITZERLAND | 1.152 | 4.876E-4 | 0.165 | 1.780E-2 | - | - | - | - | - | - |
| | Graphite Reflector | | | | | | | | | |
| XSDRN-PM[1] | 1.435 | 3.518E-5 | 0.828 | 2.048E-4 | 1.646 | 4.757E-5 | 0.942 | 1.106E-5 | 0.828 | 2.048E-4 |
| ANISN[2] | 1.193 | 3.541E-5 | 0.828 | 2.049E-4 | 1.382 | 4.791E-5 | 0.943 | 1.107E-5 | 0.828 | 2.049E-4 |
| LEOPARD[3] | 1.327 | 2.962E-5 | 0.876 | 2.134E-4 | 1.546 | 3.832E-5 | 0.873 | 1.156E-5 | 0.876 | 2.134E-4 |
| ANL | - | - | - | - | 1.334 | 1.160E-5 | 0.876 | 1.297E-5 | 0.842 | 2.510E-4 |
| SWITZERLAND | 1.402 | 0.586E-5 | 0.886 | 1.962E-4 | - | - | - | - | - | - |

[1] Diffusion coefficient obtained by collapsing the transport cross section through leakage spectrum weighting.

[2] Diffusion coefficient based on flux-weighted transport cross section.

[3] Diffusion coefficient collapsed through flux weighting.

[4] Energy Boundaries

| | XSDRN-PM/ANISN | LEOPARD/ANL/SWITZERLAND |
|---|---|---|
| Group 1: | 3.0 keV < $E_n$ < 20.0 MeV | 5.53 keV < $E_n$ < 10.0 MeV |
| Group 2: | 0.8 eV < $E_n$ < 3.0 keV | 0.625 eV < $E_n$ < 5.53 keV |
| Group 3: | 0.01 meV < $E_n$ < 0.8 eV | 0 eV < $E_n$ < 0.625 eV |

[5] Read as $5.182 \times 10^{-4}$.

In general there is reasonable agreement between the ANISN and XSDRN-PM results except for the diffusion coefficients (D), where the different weighting schemes have a large effect on the resultant coefficients. Also, the agreement between LEOPARD and ANL is reasonable, except for $\Sigma_{a,1}$ for the graphite. Since this cross section has very little effect on the overall results, we have not examined this in more detail. Overall, the comparison seems reasonable.

3. Reactor Core Calculations

The quarter core (shown in Figure 12) calculations were performed with the 2DB-UM code. The fluxes were normalized to a power of 2.5 MW for the quarter core, represented by 12 mesh intervals in the X-direction and 13 in the Y-direction.

Table 14 presents the 2DB-UM calculated effective multiplication factors for the core at three different burn-up stages: the fresh core, beginning-of-life (BOL) core, and end-of-life (EOL) core (which are shown in Figure 12). Since more than one set of cross sections are available for reflectors, there are three cases examined in Table 14: the LEOPARD results were used for both reflectors in case 1, the XSDRN-PM results for both reflectors in case 2, and the LEOPARD results for light water reflector, while the XSDRN-PM results for graphite reflector in case 3. It has been noted that the eigenvalue differences between case 2 and case 3 are larger than those between case 1 and case 3, indicating that the light water reflector has more of an effect on the core calculations than the graphite reflector, as expected.

The effective multiplication factors calculated by the seven international research centers are given in Table 15, in which the results for case 3 in Table 14 are included. Following the lead of Ref. 15 wherein the German results are chosen as the reference case, the comparison of the effective multiplication factors is shown in Table 16. As can be seen, the deviations from each other are small, typically

Table 14

2DB-UM Eigenvalue Calculation for IAEA Benchmark Core

| Burnup Stage | 2DB-UM Eigenvalue | | |
|---|---|---|---|
| | Case 1 LEOPARD[1] | Case 2 XSDRN-PM[2] | Case 3 LEOPARD/XSDRN-PM[3] |
| Fresh | 1.1877 | 1.1709 | 1.1842 |
| BOL | 1.0355 | 1.0204 | 1.0323 |
| EOL | 1.0132 | 0.9985 | 1.0101 |

[1] LEOPARD calculated $H_2O$ and graphite reflector cross sections.

[2] XSDRN-PM calculated $H_2O$ and graphite reflector cross sections.

[3] LEOPARD calculated $H_2O$ reflector cross sections. XSDRN-PM calculated graphite reflector cross sections.

less than 1%$\Delta\rho$.

4. Conclusion

The results for the IAEA benchmark core using the UM code package agree very well with the results of the seven international research centers.

B. Ex-Core Cross Section Generation with the XSDRN Code

This section of the report describes the calculation of the ex-core cross sections used for the analysis of the FNR HEU and LEU cores. Previous reports described the determination of ex-core cross sections with the LEOPARD code. It was found in subsequent calculations that the in-core and ex-core power distributions as well as the core eigenvalue depend sensitively upon the values used for the heavy-water tank cross sections, so this work was begun to determine more accurate ex-core cross sections by means of a one-

Table 15

Summary of Effective Multiplication Factors

| Burnup Stage | Eigenvalue Calculation | | | | | | | |
|---|---|---|---|---|---|---|---|---|
| | 2DB-UM | Germany (INTERATOM) | USA (ANL) | Switzerland (EIR) | Austria (OSCAE) | France (CEA) | Argentina (CNEA) | Japan (JAERI) |
| Fresh | 1.1842 | 1.1888 | 1.1834 | 1.1939 | 1.1966 | 1.2020 | 1.2002 | 1.1810 |
| BOL | 1.0323 | 1.0328 | 1.0233 | 1.0368 | 1.0320 | 1.0404 | 1.0377 | 1.0420 |
| EOL | 1.0101 | 1.0101 | 1.0004 | 1.0138 | 1.0090 | 1.0170 | 1.0143 | 1.0220 |

Table 16

Comparison of Effective Multiplication Factors

| Burnup Stage | Germany (INTERATOM) | Absolute Bias (%$\Delta\rho$) | | | | | | |
|---|---|---|---|---|---|---|---|---|
| | | 2DB-UM | USA (ANL) | Switzerland (EIR) | Austria (OSCAE) | France (CEA) | Argentina (CNEA) | Japan (JAERI) |
| Fresh | 1.1888 | -0.39 | -0.45 | 0.43 | 0.66 | 1.11 | 0.96 | -0.66 |
| BOL | 1.0328 | -0.05 | -0.92 | 0.39 | -0.08 | 0.74 | 0.47 | 0.89 |
| EOL | 1.0101 | 0.0 | 0.96 | 0.37 | -0.11 | 0.68 | 0.42 | 1.18 |

dimensional transport calculation with the XSDRN code.

The structure of the heavy water tank is shown in Figures B-1 through B-7 of Ref. 1. As can be seen from the figure, the structure of the heavy water tank is complicated by numerous beam tube void cans and cylindrical penetrations filled with light water. The calculation of the core power distributions with the 2DB-UM code requires region-averaged, 2-group cross sections for each of the ex-core zones.

The region-averaged cross sections have been determined by means of several codes in the SCALE package. The CSAS code is used initially to set up the input for the remaining codes in the package. The geometrical configuration of the problem is shown in Figure 16. In the core region, the core is homogenized by volume averaging the number densities for a batch HEU and a batch LEU core from the data given in Table C-2 of Ref. 2. The core and reflector regions are then modelled in one-dimensional slab geometry, as is shown in Figure 16. A 30 cm region of light water simulates the moderator on the south side of the core. The core region consists of a homogenized mixture of LEU or HEU fuel, clad, and moderator, with a region thickness corresponding to the thickness of a five tier core in the north-south direction. The water gap between the core and the heavy water tank, and the aluminum wall of the heavy water tank are then represented. The heavy water tank is approximately modelled by dividing it into three zones of equal volume, and volume averaging the voids throughout the tank. The actual void fractions for the three heavy water zones in the south-north direction are .126, .090 and .058, respectively. A three zone model of the heavy water tank was used to account more accurately for the spatial distribution of the voids, and to account for the spatial dependence of the neutron spectrum, which was found to vary quite drastically with penetration into the tank. The light water reflector on the north side of the core is included as a 20 cm region of light water.

The cylindrical light water penetrations into the heavy water tank are neglected in the generation of average cross sections for the heavy water tank, but are included later in the modelling of the SPND and wire activation measurements described in Section II of this report.

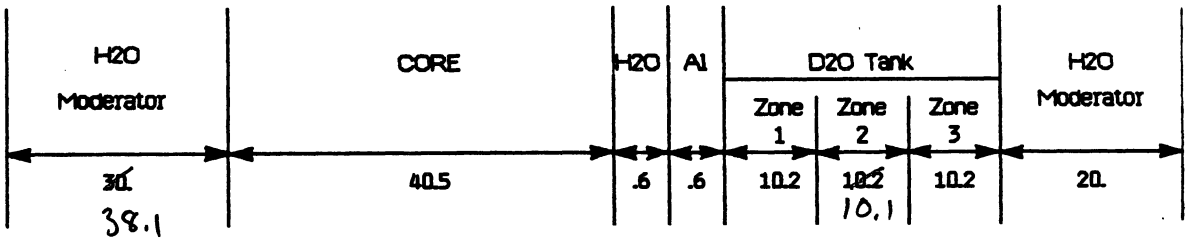


Unit Cell (cm)

Figure 16. $D_2O$-Core Geometry Used for XSDRN Calculation

The NITAWL code is used to perform the resonance calculations for the uranium isotopes by means of the Nordheim Integral Treatment. The NITAWL code also processes the master cross section libraries into a format accessible by the XSDRN code, a one-dimensional transport theory code. The master library contains 123 energy groups, 93 fast groups and 30 thermal groups.

The spectral calculations and the cross section weighting are performed by the XSDRN code. The geometry for the calculation is shown in Figure 16. A P-3, S-8 calculation is performed in 123 energy groups with a total of 35 spatial meshes including 12 meshes in the core and 9 meshes in the heavy water tank. Transverse leakage is accounted for by a geometric buckling. XSDRN determines weighted cross sections by spectrally and spatially weighting the microscopic cross sections over the calculated fine group flux distribution. XSDRN produces a set of coarse group, microscopic cross sections for each isotope for each spatial zone of the problem. The group structures are defined as follows. For

the 2-group cross section generation, group 1 extends from 14.918 MeV to .6552 eV, and group 2 extends from .6552 eV to .004742 eV. For the 4-group cross section generation, group 1 extends from 14.92 MeV to .8209 MeV, group 2 from 820.9 keV to 5.531 keV, group 3 from 5.531 keV to .6552 eV, and group 4 from .6552 eV to .004742 eV.

The XSDRN code produces fine-group transport cross sections by integrating the $P_1$ component of the scattering cross section over the current as follows:

$$\sigma_{tr}(E) = \sigma_t(E) - \frac{1}{3} \frac{\int_0^\infty dE' \; \sigma_1(E \leftarrow E') \; J(E')}{J(E)} \tag{1}$$

A zone-averaged leakage spectrum is defined as follows for the determination of the fine- and coarse-group transport cross sections:

$$L_{j,g} = \frac{\int_j d\underline{r} \int_g dE \; L(\underline{r},E)}{\int_j d\underline{r}} \tag{2}$$

where g is the fine group index, j is the zone index and $L(\underline{r},E)$ is the leakage spectrum calculated by the code. Coarse-group transport cross sections are then determined for each zone j by weighting the fine group transport cross sections over the leakage spectrum as follows:

$$\sigma_{tr,G} = \frac{\sum_g L_g \sigma_{tr,g}}{\sum_g L_g} \tag{3}$$

where G is the coarse group index and the sum is taken over all of the fine groups contained in the coarse group.

Macroscopic reflector cross sections are then determined for input to the 2DB-UM code by multiplying the microscopic cross sections by the appropriate number densities for each zone. The 2-group cross sections for the ex-core regions computed with the XSDRN code are compared with those calculated with the LEOPARD code in Table 17.

Several differences can be noted in the cross section comparisons given in Table 17. The fast group absorption cross sections for aluminum, light water, and heavy water are significantly overpredicted by the old LEOPARD library. The use of the ENDF/B-IV library with the LEOPARD code has improved the results for aluminum and light water, but LEOPARD is still inaccurate in computing heavy water cross sections. The downscattering cross section for aluminum is significantly underpredicted in the LEOPARD calculations. The most significant discrepancy occurs in the heavy water tank cross sections. The fast group absorption cross section for heavy water is overpredicted by an order of magnitude by the LEOPARD code. This is partly due to the inclusion of voids in the XSDRN calculations, and partly due to the spatial dependence of the spectral effects, which cannot be adequately modelled with the LEOPARD code. The downscattering cross section for heavy water was found to be strongly dependent on the flux spectrum, and much larger when computed with the XSDRN code, as compared with the LEOPARD calculations.

The decrease in the fast absorption cross section of heavy water and the increase in the downscattering cross section of heavy water led to a large change in the thermal flux distribution in the heavy water tank, as can be seen in Figure 17. The thermal flux peak is significantly larger in the $D_2O$ tank when the XSDRN cross sections are used in the 2DB-UM calculations.

Table 17. 2-Group Ex-core Cross Section Comparison ($cm^{-1}$)

| Zone | Code | Group 1 | | | Group 2 | | |
|---|---|---|---|---|---|---|---|
| | | $\Sigma_a$ | $\Sigma_{tr}$ | $\Sigma_{s,g-1\to g}$ | $\Sigma_a$ | $\Sigma_{tr}$ | $\Sigma_{s,g-1\to g}$ |
| HEU, Aluminum | LEO OLDLIB | 7.803E-4[1] | .1138 | 0.0 | 9.556E-3 | .09088 | 5.515E-5 |
| | LEO ENDF/B-IV | 3.498E-4 | .1085 | 0.0 | 9.586E-3 | .08780 | 1.463E-4 |
| | XSDRN 123 GP | 3.933E-4 | .1164 | 0.0 | 1.051E-2 | .09367 | 2.296E-4 |
| HEU, Light Water | LEO OLDLIB | 8.691E-4 | .2776 | 0.0 | .01853 | 2.112 | .05267 |
| | LEO ENDF/B-IV | 4.914E-4 | .2932 | 0.0 | .01830 | 2.073 | .05314 |
| | XSDRN 123 GP | 5.372E-4 | .2726 | 0.0 | .01845 | 2.867 | .05963 |
| HEU, Heavy Water | LEO OLDLIB | 4.698E-4 | .1803 | 0.0 | 6.651E-5 | .3075 | 5.465E-3 |
| | LEO ENDF/B-IV | 3.312E-4 | .1823 | 0.0 | 6.535E-5 | .2957 | 5.473E-3 |
| | XSDRN 0-10cm | 5.785E-5 | .2045 | 0.0 | 5.817E-5 | .3373 | 6.746E-3 |
| | XSDRN 10-20cm | 4.084E-5 | .2265 | 0.0 | 6.222E-5 | .3528 | 1.113E-2 |
| | XSDRN 20-30cm | 4.286E-5 | .2416 | 0.0 | 6.668E-5 | .3682 | 1.568E-2 |
| LEU, Aluminum | LEO OLDLIB | 7.719E-4 | .1141 | 0.0 | 1.041E-2 | .09172 | 4.844E-5 |
| | LEO ENDF/B-IV | 3.528E-4 | .1088 | 0.0 | 1.051E-2 | .08872 | 1.317E-4 |
| | XSDRN 123 GP | 3.847E-4 | .1169 | 0.0 | 1.043E-2 | .09355 | 2.169E-4 |
| LEU, Light Water | LEO OLDLIB | 7.415E-4 | .2636 | 0.0 | .01781 | 2.009 | .04738 |
| | LEO ENDF/B-IV | 4.318E-4 | .2760 | 0.0 | .01781 | 1.992 | .04731 |
| | XSDRN 123 GP | 5.320E-4 | .2704 | 0.0 | .01841 | 2.869 | .05856 |
| LEU, Heavy Water | LEO OLDLIB | 4.721E-4 | .1800 | 0.0 | 6.513E-5 | .3058 | 5.391E-3 |
| | LEO ENDF/B-IV | 3.335E-4 | .1820 | 0.0 | 6.467E-5 | .2947 | 5.388E-3 |
| | XSDRN 0-10cm | 5.814E-5 | .2044 | 0.0 | 5.768E-5 | .3366 | 6.514E-3 |
| | XSDRN 10-20cm | 4.080E-5 | .2265 | 0.0 | 6.217E-5 | .3517 | 1.103E-2 |
| | XSDRN 20-30cm | 4.275E-5 | .2417 | 0.0 | 6.633E-5 | .3672 | 1.565E-2 |

(1) Read as $7.803 \times 10^{-4}$

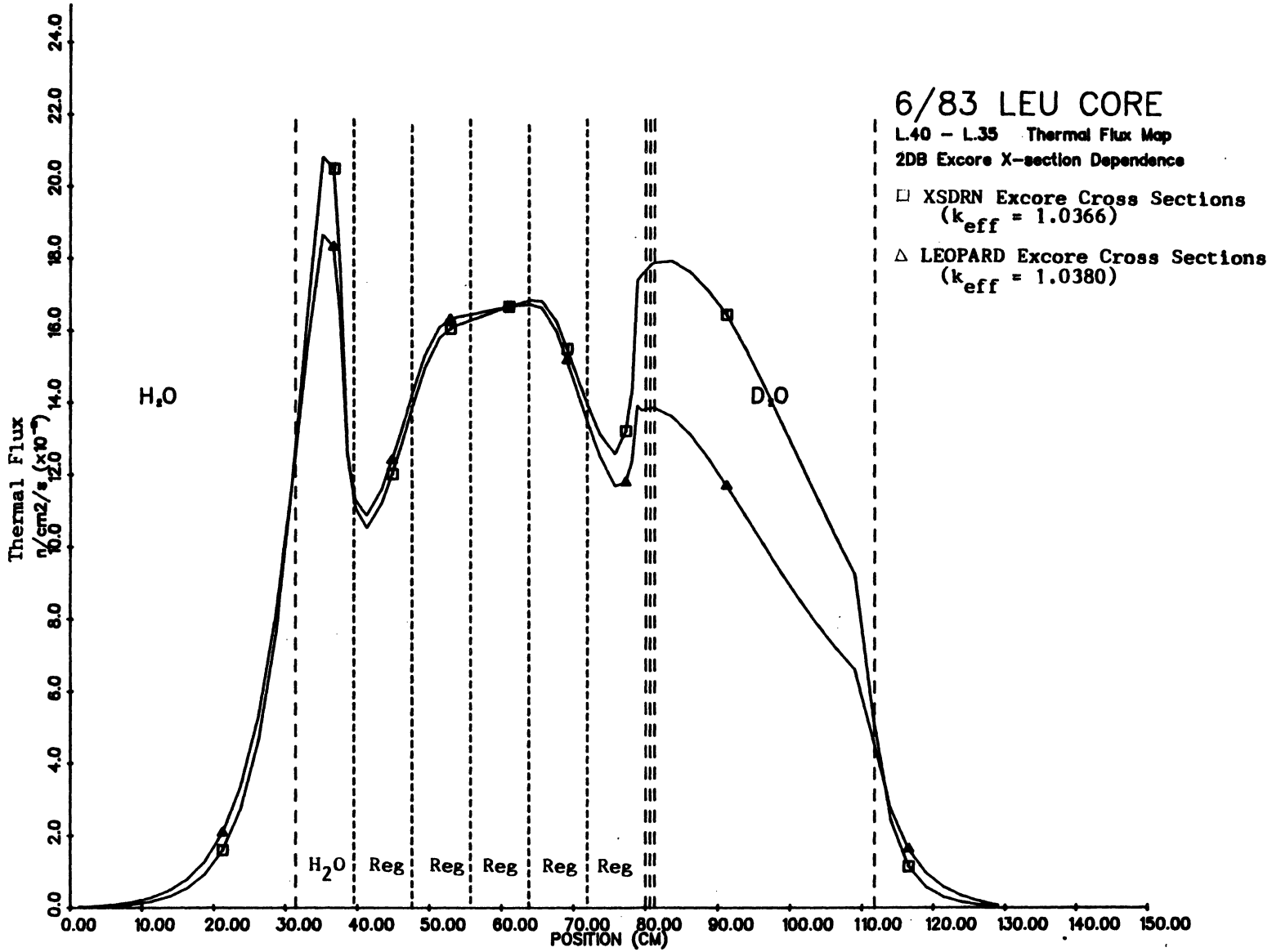


Figure 17 $D_2O$-Core Thermal Flux Distribution

## C. Three-Dimensional Capability for 2DB-UM

Effort has been expended over the past two years to develop a three-dimensional version of the two-dimensional diffusion theory code 2DB-UM. This capability is needed to analyze control rod worths, axial depletion effects, and flux distributions in the core and $D_2O$ tank. Because the 2DB-UM code has been a successful tool for 2-D global diffusion-depletion calculations of the FNR it was decided to incorporate the three dimensional capability into 2DB-UM rather than modifying an existing 3-D code (e.g., PDQ-7[17], VENTURE[18], and 3DB[19] are operational on MTS) to include the various enhancements that have been made to 2DB-UM over the years, such as the macroscopic depletion scheme.

The approach is similar to the 3DB algorithm. Planes have been added to account for the third dimension and another iteration over planes is included to converge the 3-D solution. The inner iterations still involve calculation for one plane, with the appropriate terms added to account for the interaction with the neighboring planes. Extensive changes were needed for the input routines to allow the specification of axial zones as well as changes to the output routines to allow edits over the axial zones. The modified code, named UMDIF, has been tested extensively, including comparisons with the original version of 3DB, benchmark calculations of an IAEA test problem, and comparisons with 2DB-UM for a mid-core FNR problem. These test calculations are described in more detail below.

### 1. Comparisons with 3DB

The 3DB code has been operational on MTS for several years and can be used for static 3-D analysis. The 3DB code package received from the Argonne Code Center included a sample case for a simple 1/8-reactor consisting of a homogeneous fast reactor core with a blanket. A two group description was used and three different meshes were calculated -- 2x2x2, 4x4x4, and 10x10x10. The results are tabu-

lated in Table 18, where it is evident that the codes compare very well. Although only multiplication factors are compared in Table 18, the point-wise fluxes also agree to within 4 decimal points for all cases.

Table 18

Comparison of Multiplication Factors
UMDIF Versus 3DB

| Mesh | $k_{eff}$ | |
|---|---|---|
| | UMDIF | 3DB |
| 2x2x2 | 1.15890 | 1.15890 |
| 4x4x4 | 1.06187 | 1.06188 |
| 10x10x10 | 1.02167 | 1.02172 |

2. IAEA Test Problem

The Argonne Benchmark Problem Book[20] contains benchmark problems for many different neutronic configurations, including a 3-D static diffusion theory problem. This problem is a severe test of a 3-D code, since it consists of a quarter core with several fully inserted control rods and one partially inserted control rod, reflected by water on all sides. Figure 18, taken from Ref. 20, depicts the configuration.

Table 19 summarizes the results for the benchmark problem. The UMDIF calculation predicts a multiplication factor that agrees to within .01% of the reference VENTURE solution, which utilized a Richardson-extrapolation of several VENTURE runs, as summarized in Table 19. The UMDIF calculation employed a relatively crude mesh (17x17x29) and the lack of edits for that particular run did not allow a determination of a local quantity such as the peak-to-

BENCHMARK SOURCE SITUATION

Identification: 11

Date Submitted: June 1976 By: R. R. Lee (CE)
D. A. Meneley (Ontario Hydro)
B. Michaelsen (Risø-Denmark)
D. R. Vondy (ORNL)
M. R. Wagner (KWU)
W. Werner (GRS-Munich)

Date Accepted: June 1977 By: H. L. Dodds, Jr. (U. of Tenn.)
M. V. Gregory (SRL)

Descriptive Title: Multi-dimensional (x-y-z) LWR Model

Suggested Functions: Designed to provide a severe test for the capabilities of coarse mesh methods and flux synthesis approximations

Configuration: Three-dimensional configuration including space dimensions and region numbers: 2 Figures

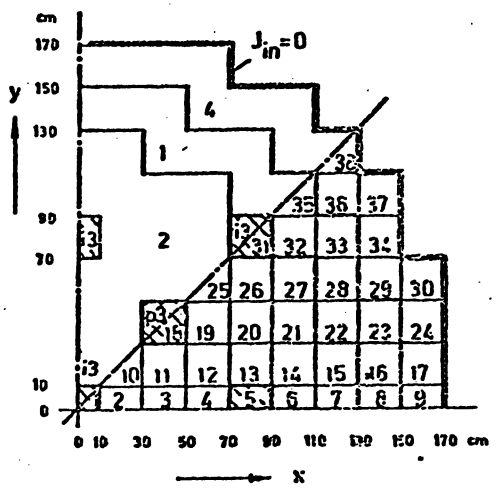


Horizontal Cross Section

Upper Octant: Region Assignments

Lower Octant: Fuel Assembly Identification

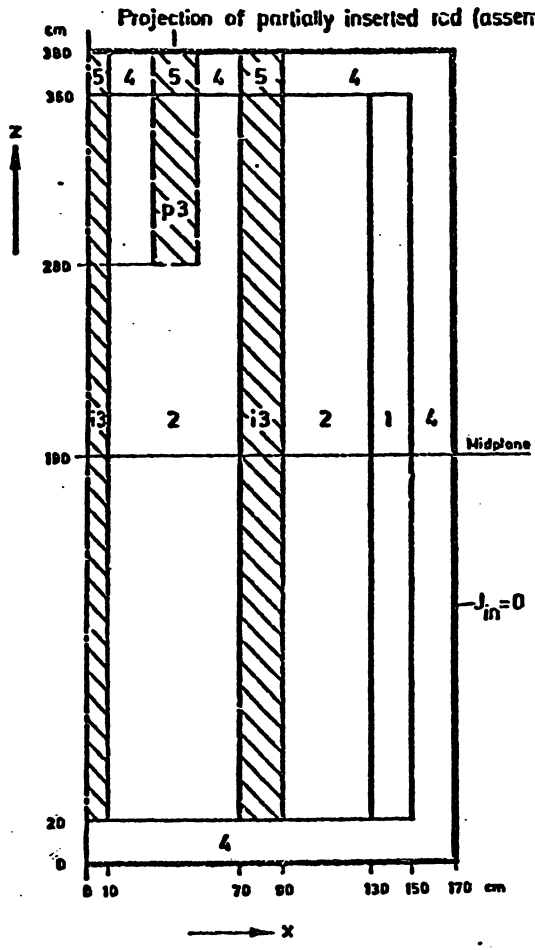


Vertical Cross Section, y = 0

Boundary Conditions:

External Boundaries: Vacuum, no incoming current
Symmetry Boundaries: Reflection, no net current

Figure 18 IAEA Benchmark Problem Configuration

average power density. Although we have concluded that the UMDIF code yields correct results for the test problem discussed above, we would like to include some additional comparisons for completeness, including a finer mesh calculation (to compare with the 34x34x38 VENTURE calculation in Table 19) and a comparison of the peak-to-average power density and perhaps other local quantities such as relative flux levels.

Table 19

3-D, 2-Group IAEA Benchmark Problem Results
(Non-Return External Boundary Conditions)

| Mesh Points (Total Unknowns) | Multiplication Factor | Peak-to-Average Power Density | IBM-360/91 Processor Time (min) |
|---|---|---|---|
| VENTURE | | | |
| 9x9x10 (1,620) | 1.03176 | 2.3765 | 0.3 to 1 |
| 17x17x19 (10,982) | 1.02913 | 2.5672 | 1.6 to 5 |
| 34x34x38 (87,856) | 1.02864 | 2.5035 | 49 |
| 68x68x76 (702,848) | 1.02887 | 2.4081 | 192 |
| 102x102x114 (2,372,112) | 1.02896 | 2.3780 | 360[1] |
| Extrapolated | 1.02903 | 2.354 | |
| UMDIF | | | |
| 17x17x29 (16,762) | 1.02897 | - | 4[2] |

[1] IBM 195

[2] Amdahl 5860

## 3. FNR Test Problem

Since the objective of the 3-D capability is the analysis of the FNR, UMDIF has been applied to a typical FNR configuration which has been calculated with 2DB-UM. The particular configuration examined was an LEU core on September 16, 1983 (Cycle 229A). The UMDIF thermal fluxes were normalized to yield the same core average as calculated by 2DB-UM. Figure 19 summarizes the resultant assembly-averaged thermal flux distribution for the core and reflectors ($D_2O$ and $H_2O$) as well as fast-to-thermal flux ratios for selected regions. As can be seen, the agreement is very good within the core and significant deviations between 2DB-UM and UMDIF do not occur until well into the $D_2O$ tank, where one might expect differences between 2-D and 3-D predictions due to the non-separability of the flux in the $D_2O$ tank. As a further indication of the non-separability of the flux in the reflectors, Figure 20 summarizes the quarter-height and half-height thermal fluxes predicted by UMDIF in the core and reflectors. As can be seen, the difference in the thermal flux at these two axial locations is significantly larger in the reflector regions (5-10%) than in the core regions (0-2%). This indicates a substantial difference in the axial profiles in the reflector regions and core regions, hence indicating the importance of the 3-D capability.

Effort is still being made to analyze a fine mesh (6x6) model of the above core, in addition to the relatively coarse mesh (2x2) summarized above. This met with some difficulties due to the large demand on computer memory, and this is currently under investigation.

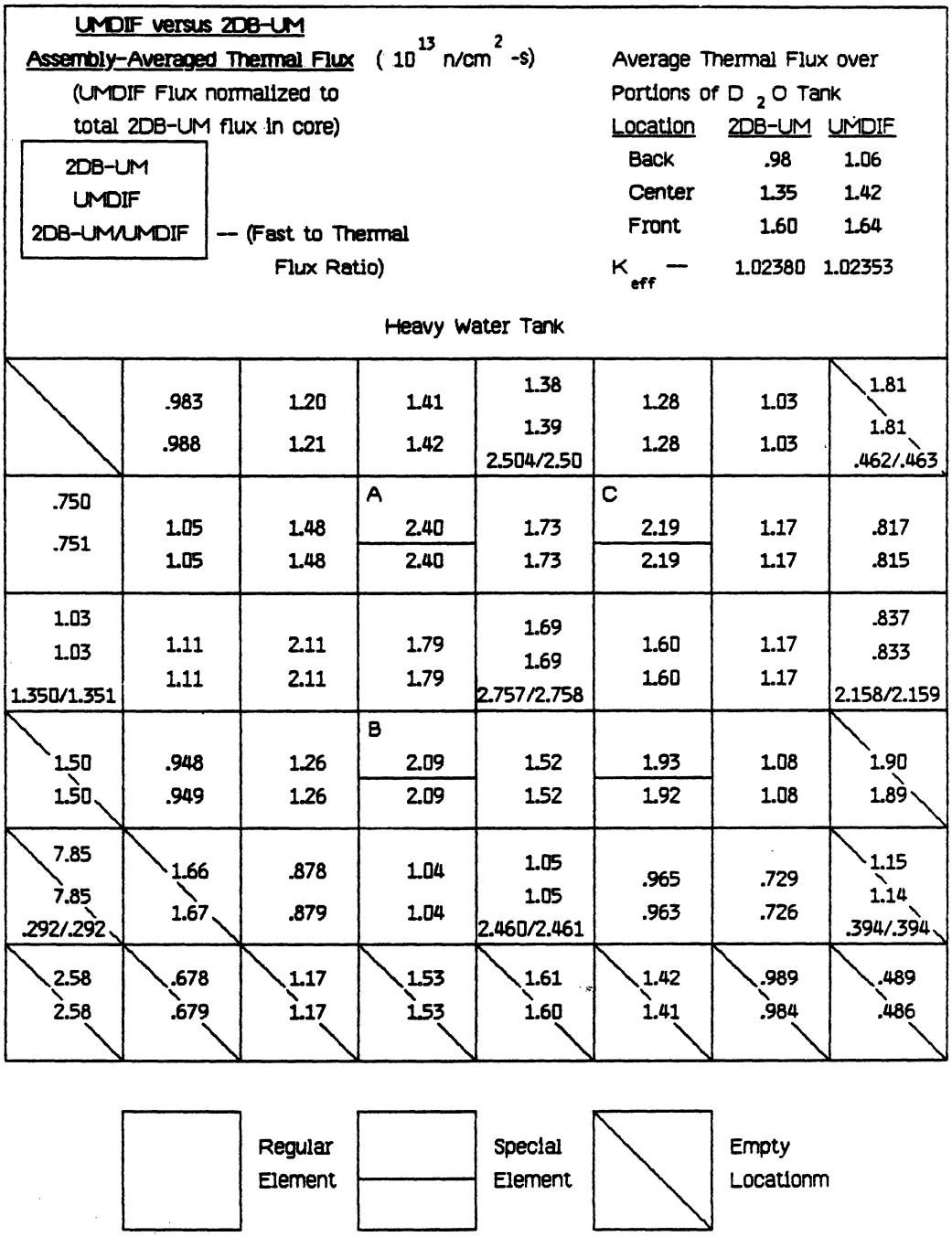


Figure 19 Assembly-Averaged Thermal Flux Distribution - UMDIF versus 2DB-UM

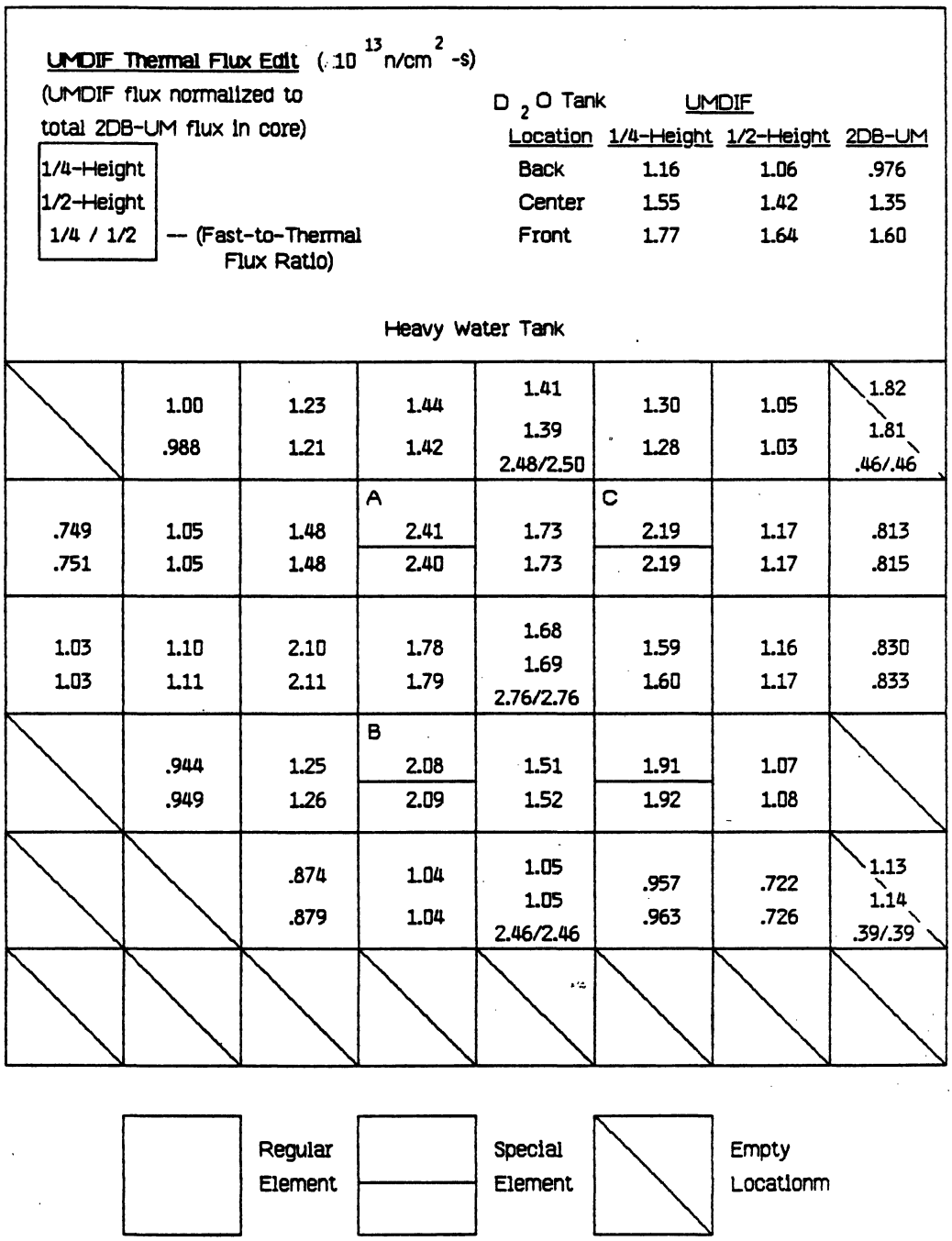


Figure 20 UMDIF Calculated Thermal Fluxes

# V. SUMMARY AND RECOMMENDATIONS FOR FUTURE WORK

A major emphasis during the past two to three years in the experimental portion of the project has focused on the unfolding of the FNR neutron flux spectra through multiple foil activations. During the present reporting period, unfolded flux spectra have been obtained both for LEU and HEU configurations. This effort covered the entire energy range of interest including thermal and fast energies. The unfolded flux spectra indicate hardening of the neutron flux in the LEU configurations as compared with that in the HEU environment. This is in agreement with saturation activity data obtained with wire and foil samples. A comparison of subcadmium fluxes measured with different activation materials has also been made as part of the incore flux measurement effort.

Comparison of the subcadmium flux data obtained with Rh SPNDs and iron wire activations has taken considerable effort during this reporting period. To determine the subcadmium sensitivity factor for the SPNDs, measurements of the flux depression due to the detector paddle was made in addition to measurements of the subcadmium current fraction and flux perturbation due to the detector itself. The SPND response, calibrated against iron activations, indicates considerable sensitivity to the detector environment.

Further measurement and analysis of the SPND response are underway to better understand this observation regarding the SPND sensitivity. Measurement of excore flux spectra at selected beam ports and further comparisons of different detector materials for subcadmium flux determination are also desirable.

Calculated incore and excore flux distributions are rather sensitive to few-group cross sections for the heavy water tank. An attempt has been made to represent approximately material heterogeneities in the tank in space-dependent flux spectrum calculations for generation of heavy

water cross sections. FNR operation over a period of four years has been simulated with the 2DB-UM code to provide a better estimate of fuel burnup for calculation of flux distributions and core eigenvalues. As part of the ongoing effort for validation of our neutronic analysis package used for the LEU project, an IAEA benchmark problem for an HEU configuration was analyzed.

Current effort in the simulation of experimental data centers around evaluation of three-dimensional effects in the calculated flux distributions and core eigenvalues. This includes study of the effects of distributed fuel burnup, and representation of shim and regulating rods partially inserted into the core. Another emphasis will be made in simulation of measured reactivity parameters including temperature coefficient of reactivity and power defect of reactivity. Analysis of an LEU configuration is also under consideration as part of the IAEA benchmark study.

Additional tasks in the project include completion and documentation of UM code package, and preparation of a final report for the LEU project. These efforts in the last phase of the project should be of considerable benefit to the research reactor community.

REFERENCES

1. W. Kerr, et. al., "Low Enrichment Fuel Evaluation and Analysis Program, Summary Report for the Period January, 1979 - December, 1979", Department of Nuclear Engineering and Michigan-Memorial Phoenix Project Report, The University of Michigan (January 1980).

2. W. Kerr, et. al., "Low Enrichment Fuel Evaluation and Analysis Program, Summary Report for the Period January, 1980 - December, 1980", Department of Nuclear Engineering and Michigan-Memorial Phoenix Project Report, The University of Michigan (March 1981).

3. W. Kerr, et. al., "Low Enrichment Fuel Evaluation and Analysis Program, Summary Report for the Period January, 1981 - December, 1982", Department of Nuclear Engineering and Michigan-Memorial Phoenix Project Report, The University of Michigan (January 1983).

4. D. K. Wehe, et. al., "Subcadmium Flux Measurements in HEU and LEU Cores Using Rhodium SPND and Wire Activations ", Presented at the International Symposium on the Use and Development of Low and Medium Flux Research Reactors, Massachusetts Institute of Technology (October 17-19, 1983).

5. D. K. Wehe, C. R. Drumm, W. R. Martin, and J. C. Lee, "Operating Experience, Measurements, and Analysis of the LEU Whole Core Demonstration at the FNR", Presented at the International Conference on Reduced Enrichment for Research and Test Reactors, Tokyo (October 1983).

6. D. K. Wehe, "Measurements of Neutron Spectra in HEU and LEU Fuels," Ph.D. Dissertation, The University of Michigan (1984).

7. R. M. Westfall et al., "SCALE: A Modular Code System for Performing Standardized Computer Analysis for Licensing Evaluation," NUREG CR-0200, Radiation Shielding Information Center, Oak Ridge National Laboratory (1980).

8. N. M. Greene and C. W. Crave, Jr., "XSDRN: A Discrete Ordinates Spectral Averaging Code", ORNL-TM-2500, Oak Ridge National Laboratory (July 1969).

9. W. W. Engle, Jr., "ANISN, A One-Dimensional Discrete Ordinates Transport Code with Anisotropic Scattering", K-1693, Oak Ridge National Laboratory (March 1966).

10. L. J. Milton and R. N. Blomquist, "VIM User's Guide", Argonne National Laboratory Report (March 1983).

11. W. W. Little, Jr. and R. W. Hardie, "2DB User's Manual-Revision 1", BNWL-831 REV1, Battelle Pacific Northwest Laboratory (February 1969).

12. R. F. Barry, "LEOPARD-A Spectrum Dependent Non-Spatial Depletion Code", WCAP-3269-26, Westinghouse Electric Corporation (September 1963).

13. J. Barhen, W. Rothenstein, E. Taviv, "The HAMMER Code System", NP-565, Electric Power Research Institute (October 1978).

14. K. D. Lathrop and F. W. Brinkley, "TWOTRAN-II - An Interfaced Exportable Version of the TWOTRAN Code for Two-Dimensional Transport", LA-4848-MS, Los Alamos Scientific Laboratory (1973).

15. "Research Reactor Core Conversion from the Use of Highly Enriched Uranium to the Use of Low Enriched Uranium Fuels Guidebook", IAEA-TECDOC-233, International Atomic Energy Agency (August 1980).

16. T. R. England, "CINDER--A One-Point Depletion and Fission Product Program", WAPD-TM-334, Bettis Atomic Power Laboratory (August 1962).

17. W. R. Cadwell, "PDQ-7 Reference Manual", WAPD-TM-678, Westinghouse Electric Corporation (January 1967).

18. D. R. Vondy, T. B. Fowler and G. W. Cunningham, "VENTURE: A Code Block for Solving Multigroup Neutronics Problems Applying the Finite-Difference Diffusion Theory Approximation to Neutron Transport", ORNL-5062, Oak Ridge National Laboratory (1975).

19. R. W. Hardie and W. W. Little, Jr., "3DB, A Three-Dimensional Diffusion Theory Burnup Code", BNWL-1264, Battelle Northwest Laboratory (1970).

20. "Argonne Code Center: Benchmark Problem Book", ANL-7416 Supplement 2, Argonne National Laboratory (June 1977).

# APPENDIX A

## Subcadmium Flux Measurements in HEU and LEU Cores Using Rhodium SPND and Wire Activations

# SUBCADMIUM FLUX MEASUREMENTS IN HEU AND LEU CORES

# USING RHODIUM SPND AND WIRE ACTIVATIONS

D.K. Wehe, C.R. Drumm, J.C. Lee, J.S. King, W.R. Martin
The University of Michigan
Ann Arbor, Michigan
M.M. Bretscher
Argonne National Laboratory
Argonne, Illinois

## ABSTRACT

The sensitivity of a rhodium self-powered neutron detector (SPND) was measured in an MTR core and found to be significantly smaller than the measurements and calculations of Warren would indicate. An analytic model which incorporates empirical beta escape data was developed, and the calculations tend to support these lower measured values.

---

## INTRODUCTION

As part of the Reduced Enrichment for Research and Test Reactors program, the 2 MW Ford Nuclear Reactor (FNR) at the University of Michigan (UM) is currently comparing high enriched uranium (HEU) and low enriched uranium (LEU) MTR type fuels. As a part of the measurements, flux maps using rhodium SPNDs have been made on a variety of HEU, LEU and mixed cores. However, when the SPND flux maps were compared with fluxes obtained from wire activations, differences were noted both in intensity and shape. Since the absolute fluxes determined from the activations are believed to be correct, the sensitivity of the detector, S, must be different from the generally accepted values. In order to explain this difference, a simple model for calculating S was developed, and the results of the calculations are shown to support the revised values of S determined from the measurements.

## DETECTOR AND CORE CHARACTERISTICS

The FNR core consists of MTR regular fuel assemblies (18 fuel plates) and special fuel assemblies (9 fuel plates with a central waterhole). The physical dimensions of the HEU and LEU elements are identical, although the LEU fuel has approximately 20% more U-235 per assembly. The core is surrounded on three faces with a light water reflector, and is bounded by a heavy water reflector on the fourth face.

The operating characteristics of a rhodium SPND are discussed in reference (1). The SPND's used in these experiments have .020" diameter rhodium emitters, $Al_2O_3$ and MgO insulators, and .062" outer diameters. A background lead running the length of the detector cable was used to determine the background signal strength. Each detector is mounted on a 36" x .625" x .093" inconel paddle for structural support. A 1.5" x .25" hole around the emitter reduces the perturbation caused by paddle.

## MEASUREMENTS OF THE DETECTOR SENSITIVITY

The SPND produces a direct current as its output signal. The net current signal is proportional to the reaction rate in the emitter, which in turn is proportional to the flux. The amount of current produced per unit flux is defined to be the sensitivity of the detector. More specifically, if $f'_{sc}$ is the fraction of the net detector current ($I_{net}$) which would be produced by placing the detector into a flux with a subcadmium component $\phi_{sc}$, then the subcadmium sensitivity is defined by:

$$S_{sc} \equiv \frac{f'_{sc} I_{net}}{\phi_{sc}}$$

To determine the detector sensitivity, the values of $\phi_{sc}$, $f'_{sc}$, and $I_{net}$ were independently measured at the same location. These measurements were performed in the core and $D_2O$ reflector, for both HEU and LEU fuels.

The net equilibrium current was determined by directly measuring the current (~50 nanoamps) coming from the emitter lead and subtracting the current measured at the background lead. Two rhodium SPND detectors with similar mountings were used during the course of these measurements. Calibrations performed in the core showed the detectors' measured net currents were in good agreement.

The subcadmium current fraction was measured by activating bare and cadmium covered rhodium wires with the same diameter as the detector emitter. The wires were counted on a GeLi detector, and

it can be shown that[2]:

$$f'_{sc} \sim f_{sc} \equiv 1 - 1/CR$$

where CR is the cadmium ratio of rhodium.

The subcadmium flux was determined by activating bare and cadmium covered iron wires, and then counting the activities using a GeLi detector and ND6600 analyzer. Absolute efficiencies are determined from an NBS mixed radionuclide standard. The conversion from saturated activities per unit nucleus (A) to subcadmium flux is made using an LEU spectrum-averaged cross section calculated by a one-dimensional transport code. Since,

$$\phi_{sc} = \frac{A^{bare} - A^{cadmium}}{\bar{\sigma}}$$

the sensitivity is directly proportional to this cross section, which in turn depends on the spectrum. While it is conventional to use a 2200 m/sec cross section to obtain a sensitivity ($S_{2200}$) which is a current per "2200 m/sec flux", the subcadmium flux is the true quantity of interest. Hence, a spectrum-averaged, subcadmium group cross section is used in the analysis.

To make these results more generally applicable, experiments were performed to separate out the effect of the paddle on the sensitivity. Inconel paddles which duplicated the detector support paddles were constructed and bare iron wires were attached. The loaded paddles were irradiated and the results of the activation were compared with bare iron wires irradiated without the paddle. The results show a 7% flux depression at the emitter caused by the paddle. Since the current from the emitter would be 7% larger without the paddle, the measured sensitivities have been increased by this amount.

Table I shows the sensitivity determined from the measurements for the 2.54 cm long emitter with the effect of the support paddle removed. The subcadmium sensitivities measured in the HEU and LEU cores agree reasonably well. Since the HEU spectrum is softer in the core, this agreement would be even better if an HEU spectrum averaged cross section were used in the analysis. The subcadmium sensitivities measured in the heavy water reflector for HEU and LEU cores differ by ~16%, which is larger than expected. Comparing the average value of the sensitivity measured in the core to the average value measured in the heavy water reflector, it is clear that the detector is significantly more sensitive (~42%) in the reflector. Interestingly, this conclusion is still true even if the values were converted to conventional $S_{2200}$ sensitivities.

## COMPARISON WITH PREVIOUS MEASUREMENTS

Table III shows a compilation of previous measurements and calculations of the conventional $S_{2200}$ sensitivity for rhodium SPNDs similar to the ones used in these experiments. These values are also converted into subcadmium sensitivities for comparison with our measured values. These conversions were made by using the individual author's interpretation of the 2200 m/sec flux, and multiplying by the appropriate ratio $\phi_{2200}/\phi_{sc}$.

The present measurements of the LEU core sensitivity are considerably lower than Warren's[5] measurement (22%) and calculation (29%), and about 10% lower than the measurements reported in references (4), (6), and (7). In the heavy water reflector, the present LEU measurement is about 9 % lower than Warren's measurement, but about 6-10% larger than the values in references (4), (6), and (7). Thus in general, the heavy water sensitivity agrees reasonably well with previous measurements, but the sensitivity measured in the core is significantly lower (10-22%) than previously reported.

## CALCULATION OF THE DETECTOR SENSITIVITY

The measured values for the sensitivity of the detector in the core disagrees significantly both from Warren's calculations, and the present measurement in the $D_2O$ reflector. In order to identify the source of theese differences, an analytical model of the detector is developed below. If the detector is placed in a neutron flux, a net equilibrium signal will be produced which can be written as:

$$I_{net} = Ne \int_V P_\beta(\underline{r}) \int_o^\infty \sigma(E)\phi_p(\underline{r},E)\, dE d\underline{r}$$

where e = electron charge, N = number density of nuclei in the emitter, $\sigma(E)$ = the Rh-103 activation cross section. $\phi_p(\underline{r},E)$ is the actual (perturbed) flux in the emitter at point $\underline{r}$ and energy E, $p_\beta(\underline{r})$ is the probability averaged over the beta spectrum that a beta emitted at point $\underline{r}$ will contribute to the detector current, and the spatial integral is over the volume V of the detector.

Since the ultimate goal is to determine the average unperturbed subcadmium flux $\langle\phi_{sc}\rangle$ at the emitter's position without the detector present, it is convenient to define:

$$\overline{\beta}_{sc} \equiv \frac{\int_V P_\beta(\underline{r}) \int_o^{E_{cc}} \sigma(E)\phi_p(\underline{r},E)\, dE d\underline{r}}{\int_V \int_o^{E_{cc}} \sigma(E)\phi_p(\underline{r},E)\, dE d\underline{r}}$$

= average probability that a beta born in the emitter from a subcadmium reaction will contribute to the current

$$f'_{sc} = \frac{\int_v P_\beta(\underline{r}) \int_o^{Ecc} \sigma(E)\phi_p(\underline{r},E)\,dE d\underline{r}}{\int_v P_\beta(\underline{r}) \int_o^{\infty} \sigma(E)\phi_p(r,E)\,dE d\underline{r}} = \text{subcadmium current fraction}$$

$$f_p = \frac{\int_v \int_o^{Ecc} \phi_p(\underline{r},E)\,dE d\underline{r}}{\int_v \int_o^{Ecc} \phi_o(\underline{r},E)\,dE d\underline{r}} = \text{flux perturbation factor}$$

where $\phi_o(\underline{r},E)$ is the unperturbed flux which would be present at position $\underline{r}$ and energy E without the detector present, and

$$\bar{\sigma} = \frac{\int_v \int_o^{Ecc} \sigma(E)\phi_p(\underline{r},E)\,dE d\underline{r}}{\int_v \int_o^{Ecc} \phi_p(\underline{r},E)\,dE d\underline{r}} = \text{subcadmium group cross section}$$

Using these definitions,

$$I_{net} = \frac{(NVe)\bar{\beta}_{sc}\bar{\sigma}f_p}{f'_{sc}} \langle\phi_{sc}\rangle$$

where $\langle\phi_{sc}\rangle = \frac{1}{v}\int_v \int_o^{Ecc} \phi_o(\underline{r},E)\,dE d\underline{r}$.

Thus,

$$\langle\phi_{sc}\rangle = \frac{f'_{sc} I_{net}}{(NVe)\bar{\beta}_{sc}\bar{\sigma}f_p} \equiv \frac{f'_{sc} I_{net}}{S_{sc}}$$

where $S_{sc}$ is defined to be the detector sensitivity. To calculate the sensitivity, one must then calculate the factors in:

$$S_{sc} = (NVe)\cdot\bar{\beta}_{sc}\cdot\bar{\sigma}\cdot f_p$$

for the detector.

(1) $\bar{\beta}_{sc}$. Measurements[6] and calculations[3,7] of the beta escape probability indicate a value of .46 is appropriate for our spectrum and emitter geometry. This value is considerably smaller than Warren's[5] calculated value. The SPND insulator space charge effect is calculated[3,5] to reduce this value by about 20%, which is reasonable since measurements[2] on an 18-mil emitter show a 14% reduction. Thus, $\bar{\beta}_{sc}$=.37 is adopted.

(2) $\bar{\sigma}, f_{sc}, f_p$ have been calculated using one-dimensional transport theory (ANISN)[8], and three-dimensional Monte Carlo simulations (VIM)[9], and are shown in Table II for an LEU core. Because of the three dimensional capability, the VIM results are recommended, and compared in Table III with previous calculations. On an absolute basis, the model overpredicts the core sensitivity by 6% and underpredicts the $D_2O$ sensitivity by 11%. This agreement is quite

reasonable, and tends to support a measured core sensitivity which is lower than one would predict on the basis of Warren's model. The principal improvement comes from the lower values of $\beta_{sc}$ and $\sigma$.

## CONCLUSION AND RESULTS

As shown in Table I, the sensitivity of the rhodium SPNDs measured in the FNR core ($.67 \times 10^{-21}$ amps/$\phi_{sc}$-cm) is lower than values reported in the literature for similar detectors. The sensitivities measured in HEU and LEU fuels agree reasonably well in the core (6% difference), but are 16% different in the D20 reflector for reasons which are not known. The sensitivity measured in the core was substantially smaller than the value measured in the heavy water reflector.

The analytic model predicts sensitivities which are in reasonable agreement with the measurements, although it underestimates the observed sensitivity change between core and $D_2O$ reflector. Comparing these results with the results of other approaches, this model offers an effective method for predicting subcadmium sensitivities of SPNDs.

## REFERENCES

1. J.W. Hilborn, Nucleonics, 22, 2, 69 (1964).

2. M.N. Baldwin, R.H. Clark, and J.E. Rogers, Final report, BAW-3647-13(1969). (See also BAW-3647-7).

3. T. Laaksonen and J. Saastamoinen, AECL-5124, 111 (1975).

4. J. Kroon, AECL-5124, 135 (1975).

5. H.D. Warren, NSE, 48, 331-342 (1972).

6. M.N. Baldwin and J.E. Rogers, IEEE Trans. Nucl. Sci., NS-16, 171 (1969).

7. R.P. Debair, M. Grin, and O. Simoni, EVR 4775e, Joint Nuclear Research Center, Ispra Establishment-Italy (1972).

8. W.W. Engle, Jr., K-1693, Oak Ridge Gaseous Diffusion Plant (March 1967).

9. F.L. Filmore, ANL ZPR-TM-121, Sept. 20, 1972.

10. N.P. Goldstein, IEEE Trans. Nucl. Sci., NS-20, 549 (1973).

TABLE I. Measured SPND Sensitivities for HEU and LEU Fuel[3]

| Location Fuel Type | Iron Wire | | Rh Wire | SPND | $S_{sc}$ [2] |
|---|---|---|---|---|---|
| | $\sigma$ (barns) | $\phi_{sc}$ ($10^{13}$) | $f_{sc}$ | $I_{net}$ ($10^{-9}$amps) | ($10^{-21}$amps/$\phi_{sc}$ -in) |
| Core Regular Element | | | | | |
| HEU[1] . . . . . | .844 | 2.52 | .81 | 47.78 | 1.64 |
| LEU . . . . . | .844 | 1.99 | .75 | 43.32 | 1.75 |
| $D_2O$ Reflector | | | | | |
| HEU[1] . . . . . | .907 | 1.96 | .90 | 52.67 | 2.60 |
| LEU . . . . . | .907 | 2.44 | .89 | 56.97 | 2.22 |

(1). Cross section calculated for LEU spectrum is used for HEU case.
(2). Measured sensitivity increased by 7% to account for support paddle.
(3). Rhodium emitters were 2.54 cm long and .0508 cm diameter.

Table II. Calculated SPND Sensitivities for LEU Fuel

| Location | $\bar{\sigma}$(barns) | | $f_p$ | | $f_{sc}$ | | | $S_{sc}$ ($10^{-21}$amps/$\phi_{sc}$) | |
|---|---|---|---|---|---|---|---|---|---|
| | ANISN | VIM | ANISN | VIM | ANISN | VIM | MEAS. | ANISN | VIM |
| Core | | | | | | | | | |
| LEU Fuel . | 114.0 | 114.1 | .747 | .730 | .80 | .83 | .75 | 1.90 | 1.86 |
| $D_2O$ Reflector | 120.0 | 115.8 | .719 | .768 | .89 | .93 | .89 | 1.92 | 1.98 |
| $H_2O$ Reflector | | 120.6 | | .733 | | .95 | .91 | | 1.97 |

Table III. Comparisons with Previously Quoted Values

| Author | Emitter Dia. (mils) | $S_{2200}$ ($10^{-21}$amps/$\phi_{2200}$-cm) | $S_{sc}$ ($10^{-21}$amps/$\phi_{sc}$-cm) | |
|---|---|---|---|---|
| | | | Core | $D_2O$ |
| **Measurements** | | | | |
| Warren . . . . . | .020 | 1.20 | .89 | .95 |
| Kroon . . . . . | .018 | .91 | | |
| | .020 | .99 | .76 | .80 |
| Debair . . . . . | .020 | 1.01 | | |
| Baldwin . . . . . | .018 | .96[1] | | |
| | .020 | 1.04[1] | .77 | .83 |
| This work (LEU) . . | .020 | .93 | .69 | .87 |
| $D_2O$ . . . . . | .020 | 1.10 | | |
| **Calculations** | | | | |
| This work (VIM-LEU) | .020 | .99 | .73 | .78 |
| $D_2O$ . . . . . | | .98 | | |
| Warren . . . . . | .020 | 1.31[2] | .97 | 1.04 |
| Laaksonen . . . . . | .018 | .75[3] | | |
| | .020 | .88[3] | .64 | .68 |
| Goldstein . . . . . | .020 | 1.51 | 1.12 | 1.20 |

(1). Extrapolated to 20 mils based on Kroon's experiment.
(2). Value interpolated off graph at $E_T$=.030 eV.
(3). Extrapolation based on Laaksonen's estimate.

# APPENDIX B

## Operating Experience, Measurements, and Analysis of the LEU Whole Core Demonstration at the FNR

# Operating Experience, Measurements, and Analysis of the LEU Whole Core Demonstration at the FNR

by
D. K. Wehe, C. R. Drumm, J. S. King, W. R. Martin, J. C. Lee
Department of Nuclear Engineering
University of Michigan
Ann Arbor, MI 48109

## Abstract

The 2-MW Ford Nuclear Reactor at the University of Michigan is serving as the demonstration reactor for the MTR-type low enrichment (LEU) fuel for the Reduced Enrichment for Research and Test Reactor program. Operational experience gained through six months of LEU core operation and seven months of mixed HEU-LEU core operation is presented. Subcadmium flux measurements performed with rhodium self-powered neutron detectors and iron wire activations are compared with calculations. Measured reactivity parameters are compared for HEU and LEU cores. Finally, the benchmark calculations for several HEU, LEU, and mixed HEU-LEU FNR cores and the International Atomic Energy Agency (IAEA) benchmark problem are presented.

## Introduction

The University of Michigan Department of Nuclear Engineering and the Michigan-Memorial Phoenix Project have been engaged in a cooperative effort with Argonne National Laboratory to test and analyze low enrichment fuel in the Ford Nuclear Reactor (FNR). The effort was begun in 1979, as part of the Reduced Enrichment Research and Test Reactor (RERTR) Program, to demonstrate on a whole-core basis, the feasibility of enrichment reduction from 93% to below 20% in MTR-type fuel designs.

The first low enrichment uranium (LEU) core was loaded into the FNR and criticality was achieved on December 8, 1981. The critical loading was followed by a period of about six weeks of low power testing and 3 months of high power testing during which time control rod worths, full core flux maps, and in-core and ex-core spectral measurements were made.

The initial period of LEU operation was followed by a period of high enriched uranium (HEU) operation (from 5/82 to 12/82), a period of mixed HEU-LEU core operation (from 12/82 to 6/83), and a second period of LEU operation (from 6/83 to 9/83). During these time periods additional measurements were taken to characterize and compare the HEU and LEU fuel performance, including incore and excore subcadmium flux measurements with rhodium self-powered neutron detectors (SPND's) and wire activations, in-core and

ex-core spectral measurements with spectral unfolding, control rod worths, and measurements of various reactivity coefficients.

Previous reports have described the demonstration experiments program (1) and the analytical effort (2) to develop and verify the calculational methods used for analyzing the FNR HEU and LEU configurations. Preliminary experimental and analytical results for the LEU core were presented at the 1982 RERTR meeting (3-5) at Argonne National Laboratory (ANL). This paper will focus on experience gained through an extended period of LEU and mixed core operation, and the work which has been performed to resolve some of the uncertainties identified in the previous papers.

The first section of this paper discusses the operational experience that has been gained with the LEU and mixed HEU-LEU cores. The next section of the paper describes the demonstration experiments and measurements program with the LEU and mixed HEU-LEU cores. The final section of the paper discusses the analysis of the LEU and mixed HEU-LEU core configurations and comparisons with measured data.

## Operational Experience

After six months of operation with LEU fuel, and seven months of operation with a mixed LEU-HEU core, the LEU fuel elements have reached an average burnup of 6.4% and a maximum burnup of 9.7%. The operational experience gained by the utilization of LEU fuel in these cycles will be presented in this section.

Overall, there have been few problems, and few operational changes required by the use of LEU fuel in place of HEU fuel. The mechanical performance of the LEU fuel has been excellent and no fuel has been rejected due to leakage or contamination.

The LEU fuel was designed to be similar to the HEU fuel, hence all existing fuel handling equipment and procedures can be used with the LEU fuel. The similarity in the fuel design greatly simplified the HEU to LEU fuel conversion. The water gap thickness and number of plates per fuel element were unchanged, so that the thermal-hydraulic performance of the fuels was essentially identical. The enrichment reduction from 93% to 20% was accomplished by increasing the U-238 loading from 8.04 grams to 691 grams per element, and the loading of U-235 from 140.6 grams to 167.3 grams per element to account for the resulting reactivity loss. The extra fuel was accommodated by increasing the fraction of uranium in the meat from 14.2% to 42.0%, increasing the fuel density from 2.9 gm/cc to 3.8 gm/

cc, and increasing the meat thickness from .056 cm to .081 cm, with a resulting decrease in clad thickness.

The LEU fuel has in general behaved as expected. The predicted critical mass of the initial critical loading compared well (within 1%) with the actual critical mass. Control rod worths, temperature and void coefficients of reactivity, and power defect are measurably different with the LEU fuel, as predicted, but the changes have been small enough to allow the reactor operators to use existing procedures and techniques for routine reactor operation.

Only minimal administrative changes were required for the use of LEU fuel in the FNR core. The only technical specification requiring revision was a license change to allow the use of 20% enriched fuel. Existing security and emergency plans for the facility were adequate for the LEU fuel although fuel accounting procedures had to be broadened to include plutonium production.

Overall, the conversion of the FNR from HEU to LEU fuel has been smooth without surprises. Additional experience will be gained with the approach to an equilibrium LEU core.

## Demonstration Experiments

Subcadmium fluxes have been measured in the FNR with a rhodium SPND. The rhodium SPND is mounted on an Inconel paddle and produces a current which is proportional to the neutron flux incident on the rhodium emitter wire. In order to convert the measured current to an unperturbed subcadmium flux, several factors must be determined, including the sensitivity of the detector to subcadmium neutrons, the fraction of the rhodium activation which is due to subcadmium neutrons, and the flux depression caused by the detector and the Inconel paddle. The fraction of the activation which is due to subcadmium neutrons is determined by the activation of bare and cadmium covered rhodium wires. The flux depression caused by the Inconel paddle was determined by comparing the activations of iron wires mounted both on the Inconel paddle and an aluminum paddle. The flux was found to be depressed by the Inconel paddle by about 7%. The determination of the detector sensitivity and flux depression due to the rhodium emitter wire are considered in the next section of this report.

The absolute subcadmium flux has also been determined by activation of bare and cadmium covered iron wires. The separation distance between the bare and cadmium covered wires was chosen to be large enough so that the flux depression caused by the cadmium sheath does not affect the activation of the bare wire. The counting of the activated samples is performed using GeLi detectors. Wire samples are counted between two oppositely facing detectors multiplexed

together. The sample is positioned by an automatic sample changer into a rotating, cylindrical plexiglass holder. Pulse pileup losses are accounted for with a precision pulser fed into the GeLi preamplifier. The amplified and multiplexed signals are counted using an ND 570 ADC and fed into an ND 6620 analyzer/computer for analysis. Absolute efficiencies are determined with a cross-calibration technique at a separate GeLi detector station. Background interference is made negligible for most gamma ray energies with 2"-6" of lead shielding around all detectors. The saturated activity of the sample is determined from the count rate, corrected for the irradiation and wait times. (4)

The void coefficient of reactivity was determined by measuring the reactivity change due to the insertion of an aluminum slat into a fuel element. The void coefficient for the nearly fresh LEU core is compared with previous measurements made on an equilibrium HEU core in Figure 1.

## Analysis and Comparison with Experimental Data

The analysis of the subcadmium flux measurements and the reactivity measurements will be covered in this section. The computational methods that have been used to analyze the FNR core have been reported previously (2), and will be summarized here. Burnup dependent 2-group and 4-group cross sections for the HEU and LEU MTR-type fuel assemblies have been calculated with the LEOPARD code, which is a zero dimensional unit cell spectrum code with an ENDF/B-IV data base (6).

Burnup-dependent cross sections for the control elements have been determined by the EPRI-HAMMER code, which is a 1-dimensional integral transport theory code, and TWOTRAN, which is a 2-dimensional discrete ordinates transport theory code. The EPRI-HAMMER code was used to generate cross sections for the TWOTRAN code. The TWOTRAN code was then used to compute reaction rates, which were matched with those generated by the 2DB-UM code, by adjusting the fast and thermal absoprtion and removal cross sections for the control regions. The 2DB-UM code is a substantially revised version of the two-dimensional diffusion code 2DB, which has been modified to account for spatially-dependent burnup by interpolation of a depletion dependent library of macroscopic cross sections generated by LEOPARD. The 2DB-UM code has been used for the global analysis of the core. The feature that makes the 2DB-UM code particulaly useful for the analysis of the FNR core is its flexibility and ease of use. With the 2DB-UM code it is quite easy to simulate several years of FNR operation, including bi-weekly startups and shutdowns, and fuel shuffles.

Cross sections for the reflector regions have been

calculated with the LEOPARD code, assuming a 50% non-lattice fraction, and a non-lattice peaking factor of 2. This procedure was found to be adequate for the light water reflector and aluminum regions. For the heavy water reflector it was found that the fast absorption and slowing down cross sections were very sensitive to the spectrum, necessitating a more detailed treatment of the heavy water tank, which is difficult because of the complicated structure of the tank (2).

In order to determine 2-group and 4-group heavy water cross sections for input to the 2DB-UM code, the entire FNR core and reflector regions were modelled with the XSDRN code in 1-dimensional slab geometry and 123 energy groups. The XSDRN code is a 1-dimensional, discrete ordinates, transport theory code. Two-group and four-group heavy water cross sections were determined by collapsing the fine-group cross sections over the XSDRN calculated spectra. In order to account for the beam tube voids, the heavy water tank was divided into 3 regions, and the density of the materials in each region of the tank was uniformly reduced by the volume fraction of voids in that region.

The effect of the water filled irradiation tubes was approximately determined in a separate, cylindrical geometry, 1-dimensional transport calulation with the ANISN transport theory code. The geometry of the irradiation tube was modelled exactly, and the surrounding region was approximated to simulate the environment around the tube. The flux was found to peak by about 10% in the irradiation tube penetrations.

A comparison of the use of the LEOPARD generated reflector cross sections with the use of XSDRN calculated reflector cross sections revealed significant differences in the global flux distributions. The use of the LEOPARD generated heavy water cross sections caused an underprediction of the flux in the heavy water tank, which caused an in-core flux tilt away from the heavy water tank, as compared with the calculation with the XSDRN heavy water cross sections. The flux tilt affected the control rod worth calculations, causing the worth of rod B, which is farthest from the heavy water tank, to be overpredicted by the 2DB-UM code.

The conversion of the SPND current measurements to subcadmium flux was found to be a difficult modelling problem. The method used here has been reported previously (7) and the results will be presented here.

The subcadmium flux, $\phi_{sc}$, can be determined from SPND measured net current, $I_{net}$, by the following:

$$\phi_{sc} = 1.07 \frac{I_{net} f_{sc}}{S} \qquad (1)$$

The subcadmium sensitivity factor, S, is proportional to the product of the β escape probability, the effective subcadmium absorption cross section for rhodium, σ-Rh, and the rhodium flux depression factor, fp. The β escape probability is based on a measured value, while σ-Rh and fp have been determined analytically at Argonne National Laboratory (ANL) with the VIM Monte-Carlo code and at UM with the ANISN code. The sensitivity values are tabulated in Table 1. The factor of 1.07 in equation (1) accounts for the flux depression due to the Inconel paddle surrounding the SPND detector. Figures 2-4 compare the measured subcadmium flux with the 2DB-UM results for an equilibrium HEU core, a nearly fresh LEU core, and a mixed HEU-LEU core.

The conversion of iron wire activation data to subcadmium flux is much simpler:

$$\phi_{sc} = \frac{Ab - Acd}{\sigma_{Fe}} \qquad (2)$$

where Ab and Acd are the measured saturated activities per Fe-58 nucleus for bare and cadmium covered iron wires. The effective subcadmium Fe-58 cross sections, σ-Fe, have been spectrally weighted over ANISN calculated spectra in the core and reflector regions by assuming a 1/v cross section shape for Fe-58, and a 2200 m/s cross section value of 1.18b.

Absolute subcadmium fluxes for iron wire activations and rhodium SPND measurements and 2DB-UM calculations are compared in Table 2. The ratios of the flux in the heavy water tank to the flux in the core are compared in Table 3. The measurements have been made in lattice position L-37, which is at the core center, and in the heavy water tank penetration X. Measurements and calculations have been extrapolated to a quarter core height.

Rod worth measurements for an equilbrium HEU core, a mixed HEU-LEU core, and a nearly fresh LEU core are presented and compared with 2DB-UM calculations in Table 4. Full length rod worths have been determined by multiplying measured half rod worths for the bottom half of the core by a factor of 2.

In order to benchmark the LEOPARD and the 2DB-UM codes for the neutronics analysis of HEU and LEU fuel in the FNR, the calculated eigenvalue has been compared with measurements for several HEU, mixed HEU-LEU, and LEU cores in Table 5. A part of the difference between the 2DB-UM

calculation and the measurements was believed to be due to the buildup of samarium in fuel elements that have been removed from the core for some time. Calculations with the LEOPARD code indicate that the maximum reactivity change due to the samarium buildup is about .13% $\Delta k/k$.

As a further benchmark of the LEOPARD code and the 2DB-UM code, the IAEA research reactor benchmark problem has been solved . The configuration considered was a 10 MW(th) MTR-type research reactor which contains a 6 x 5 array of fuel elements, and is reflected by graphite on two faces and is surrounded by light water. Fuel enrichments of 93%, 45%, and 20% were modelled, corresponding to HEU, medium enriched uranium (MEU), and LEU fuels, respectively and the results are summarized in Table 6. Figure 5 compares the infinite multiplication factor for the HEU fuel as a function of burnup for the cross section generation code LEOPARD with the results obtained by ANL. As can be seen, the LEOPARD results compare very well with the ANL prediction for $k_\infty$. Finally, Table 6 contains the 2DB-UM calculated effective multiplication factors for the core at three different burnup states--a fresh core, a partially depleted core at beginning of life (BOL), and a depleted core at end of life (EOL). Also tabulated in the same table are the eigenvalue predictions by several other installations. As can be seen, our results fall within the range of the other predictions, and should be considered acceptable.

References


1. D. K. Wehe and J. S. King, "The RERTR Demonstration Experiments Program at the Ford Nuclear Reactor", presented at the International Meeting on Research and Test Reactor Core Conversion from HEU to LEU fuels, Argonne National Laboratory (November 12-14, 1980).

2. D. C. Losey et al., "Core Physics Analysis in Support of the FNR HEU-LEU Demonstration Experimenst", op. cit.

3. D. K. Wehe and J. S. King, "FNR Demonstration Experiments Part I: Beam Port Leakage Currents and Spectra", Presented at the International Meeting on Research and Test Reactor Core Conversions from HEU to LEU Fuels, Argonne National Laboratory (November 8-10, 1982).

4. D. K. Wehe and J. S. King, "FNR Demonstration Experiments Part II: Subcadmium Neutron Flux Measurements", op. cit.

5. J. A. Rathkopf, C. R. Drumm, W. R. Martin, and J. C. Lee, "Analysis of the Ford Nuclear Reactor LEU Core", op. cit.

6. J. Rathkopf, "Development of ENDF/B-IV Cross Section Library for the LEOPARD Code", M.S. Project Report, Department of Nuclear Engineering, The University of Michigan (November 1981).

7. D. K. Wehe, et. al., "Subcadmium Flux Measurements in HEU and LEU Cores Using Rhodium SPND and Wire Activations", presented at the International Symposium on Use and Development of Low and Medium Flux Research Reactors, Massachusetts Institute of Technology (October 1983).

Table 1

Calculated SPND Sensitivity Factors and Fe-58 Subcadmium Cross Sections

| Environment | S($10^{-21}$ Amp/$\phi_{sc}$) | σ-Fe(b) |
|---|---|---|
| LEU Core . . | 1.85 | .850 |
| HEU Core . . | 1.85 | .854 |
| $D_2O$ Reflector | 1.98 | .913 |

Table 2

Measured and Calculated Absolute Subcadmium Flux

| Core | Subcadmium Flux($10^{13}$ n/cm$^2$/sec) | | | | | |
|---|---|---|---|---|---|---|
| | L-37 | | | $D_2O$-X | | |
| | Fe | SPND | 2DB-UM | Fe | SPND | 2DB-UM |
| 10/1/82 HEU . | 2.52 | 2.32 | 1.96 | 1.96 | 2.56 | 2.02 |
| 6/27/83 LEU . | 1.99 | 1.88 | 1.75 | 2.44 | 2.74 | 2.13 |
| 10/5/83 MIXED | 1.83 | 1.81 | 1.65 | 1.95 | 2.63 | 2.01 |

Table 3

Measured and Calculated Absolute Subcadmium Flux Ratios $D_2O$-X to L-37

| Core | Iron Wire | Rhodium SPND | 2DB-UM |
|---|---|---|---|
| 5/29/82 HEU . | - | 1.12 | .98 |
| 10/1/82 HEU . | .78 | 1.10 | 1.04 |
| 6/27/83 LEU . | 1.23 | 1.46 | 1.22 |
| 9/16/83 LEU . | - | 1.55 | 1.23 |
| 10/5/83 MIXED | 1.07 | 1.45 | 1.22 |

Table 4

Control Rod Worths

| Core | Rod | Measurement* | Calculation | %Difference |
|---|---|---|---|---|
| 9/26/82 HEU | A | 2.50 | 2.35 | -6.0 |
| | B | 2.12 | 1.97 | -7.1 |
| | C | 2.36 | 2.11 | -10.6 |
| 2/1/83 MIXED | A | 2.44 | 2.29 | -6.1 |
| | B | 2.06 | 1.98 | -3.9 |
| | C | 2.12 | 1.91 | -9.9 |
| 7/8/83 LEU . | A | 2.84 | 2.84 | 0.0 |
| | B | 2.32 | 2.35 | 1.3 |
| | C | 1.91 | 1.96 | 2.6 |

* Estimated to be 2x measured half rod worths

Table 5

2DB-UM FNR Eigenvalue Calculations

| Core | Average Burnup (%) | FNR $\rho_{ex}$ (%Δk/k) | 2DB-UM Eigenvalue* | Absolute Bias (%Δk/k) |
|---|---|---|---|---|
| Dec, 1981 Critical LEU . | 0.0 | 0.45 | 1.0063 | 0.18 |
| Apr, 1983 Critical MIXED | 12.1 | 0.10 | 1.0111 | 1.01 |
| Jun, 1983 Critical LEU . | 3.0 | 0.00 | 1.0073 | .73 |
| Jun, 1983 Full Power LEU | 3.5 | 3.29 | 1.0383 | 0.40 |
| Jul, 1983 Full Power LEU | 4.3 | 3.21 | 1.0384 | 0.49 |
| Aug, 1983 Full Power LEU | 5.2 | 3.26 | 1.0389 | 0.48 |

* Reflector cross sections from LEOPARD

Table 6

IAEA Benchmark Eigenvalues

| Core | UM | Germany (INTRATOM) | USA (ANL) | Switz. (EIR) | Austria (OSGAE) | France (CEA) | Japan (JAERI) |
|---|---|---|---|---|---|---|---|
| BOL . | 1.0346 | 1.0328 | 1.0233 | 1.0368 | 1.0320 | 1.0404 | 1.0420 |
| EOL . | 1.0122 | 1.0101 | 1.0004 | 1.0138 | 1.0090 | 1.0170 | 1.0220 |
| Fresh | 1.1877 | 1.1888 | 1.1834 | 1.1939 | 1.1966 | 1.2020 | 1.1810 |

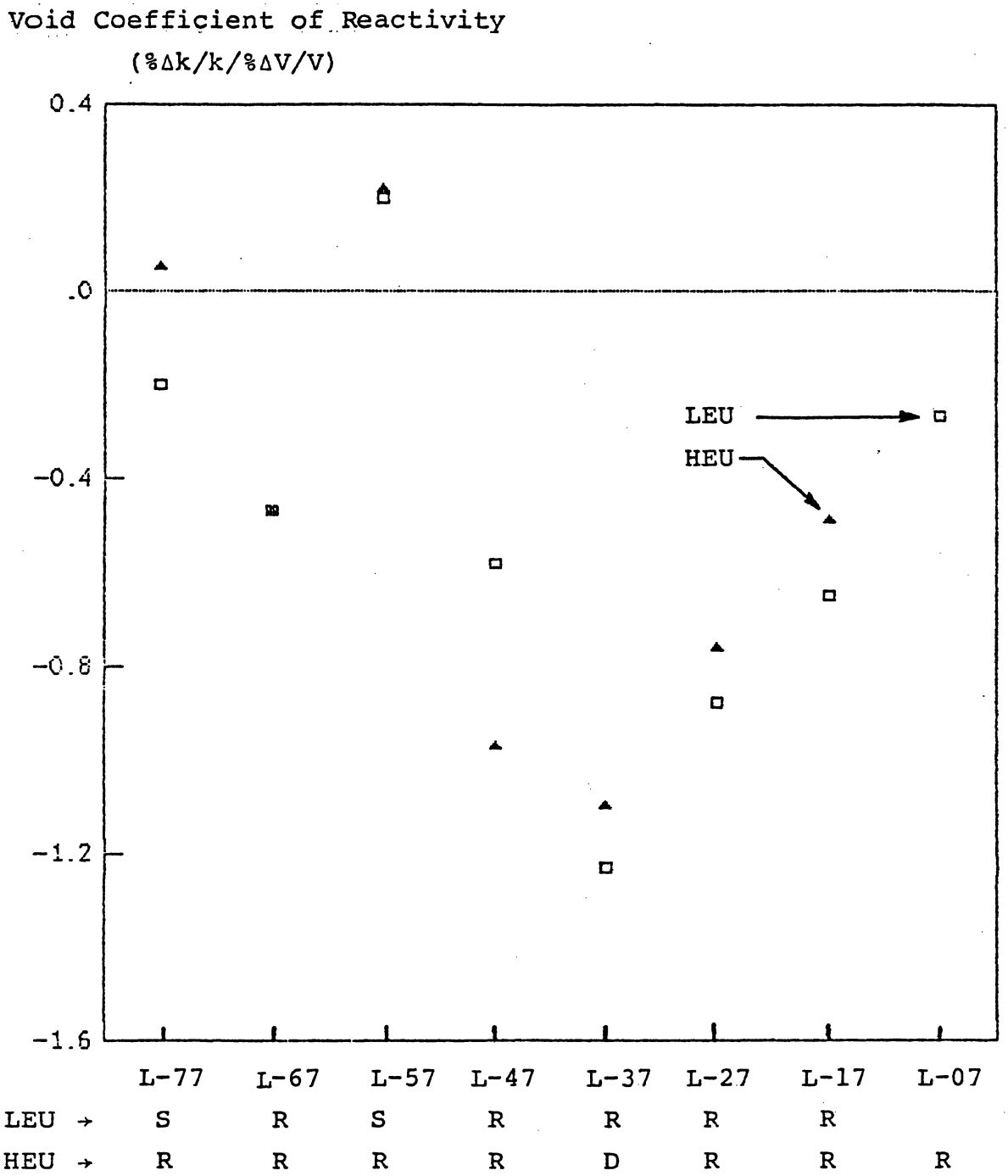


R = Regular
S = Special
D = Dispersion (HEU only)

Figure 1. Void Coefficient of Reactivity across an East-West Traverse of the FNR Core for LEU and HEU Fuels (center of core)

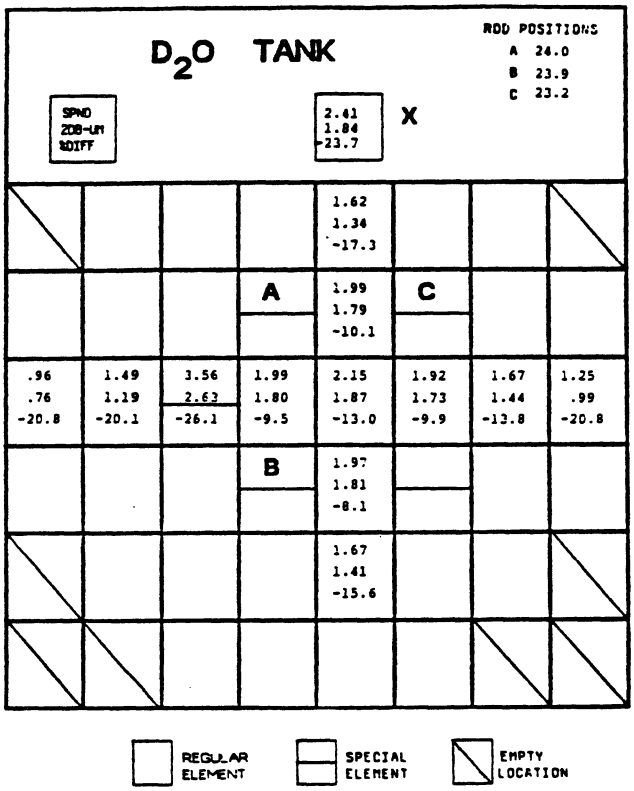


Figure 2. SPND and 2DB-UM Absolute Subcadmium Fluxes for the 5/29 82 HEU Core (Quarter Core Height)

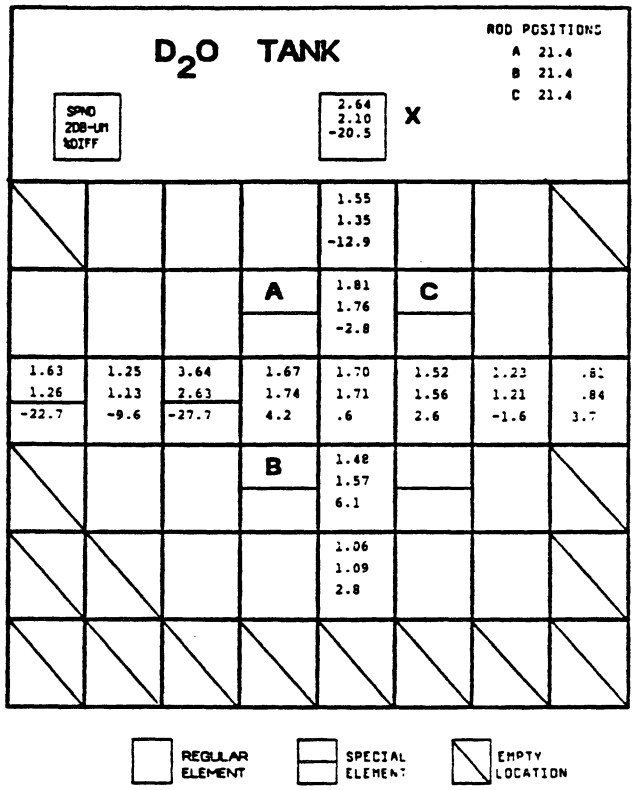


Figure 3. SPND and 2DB-UM Absolute Subcadmium Fluxes for the 9 16 83 LEU Core (Quarter Core Height)

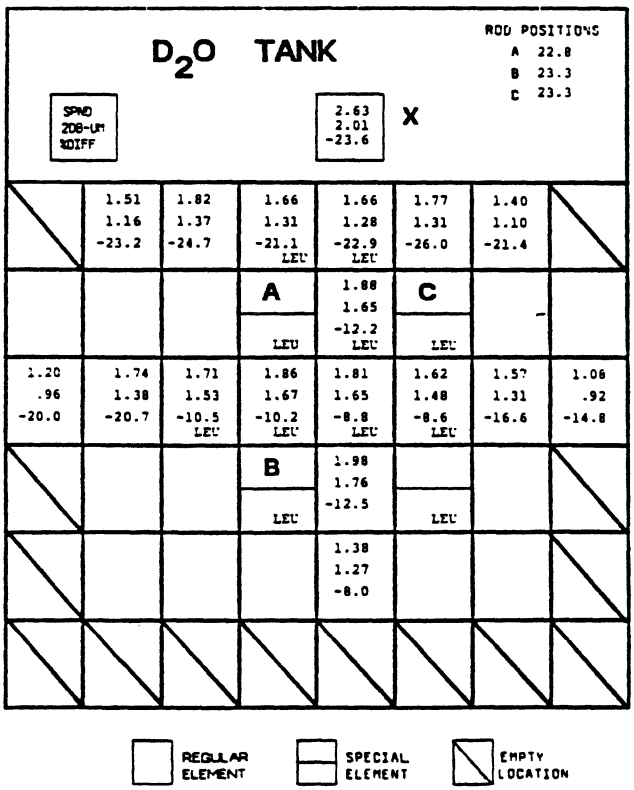


Figure 4. SPND and 2DB-UM Absolute Subcadmium Fluxes for the 10/5 /83 HEU-LEU Core (Quarter Core Height)

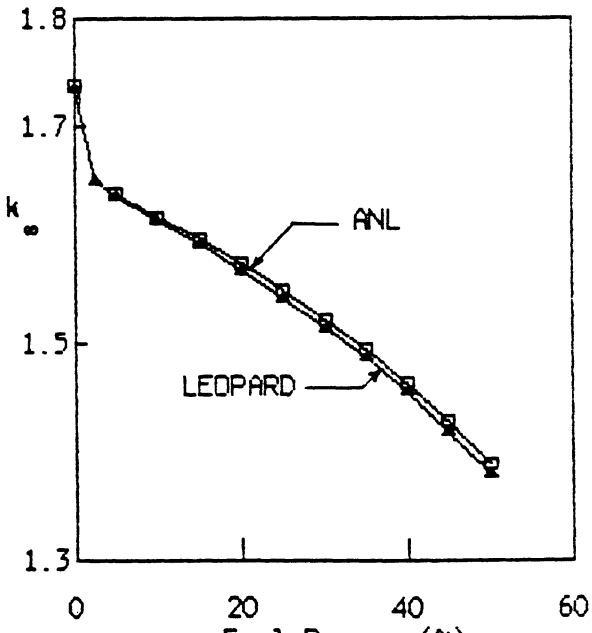


Figure 5. Infinite Multiplication Factor for HEU Fuel

# APPENDIX C

## Results of In-Core Spectral Measurements

TABLE OF CONTENTS

LIST OF FIGURES

LIST OF TABLES

In this Appendix, we present the unfolded HEU and LEU spectra. Since the refined saturated activities may be more important to some readers than even the unfolded results, some comments on these data are also presented. Although we have a variety of unfolding approaches at our disposal, we shall limit our discussion to two unfolding techniques -- the semi-empirical method and the integral unfolding method.

## 1. Thermal and Epithermal Flux Reaction Rate Data Measured in HEU and LEU Cores

Multiple foil activations were performed at a sample holder in both the HEU and the LEU cores. Prior to presenting the data, a few words of caution are necessary. Figure 1 shows the core configurations present for these measurements. Note that the HEU measurements were made in a large, equilibrium core. In contrast, the LEU measurements were made in a small, clean core, also shown in Figure 1. Because of the differences in the core sizes, one must be careful not to erroneously attribute the absolute differences in flux intensities (or activities) solely to the enrichment differences.

Table 1.A shows the saturated activities per unit target nucleus for non-threshold reactions measured at the sample holder in an HEU core. The uncertainties in these values are difficult to determine precisely. This is because the expressions used to determine the saturated activity are nonlinear, and can be quite complicated. However, the major factors which contribute to the uncertainty can be separated out, and the following expression can be used to obtain approximate values for the errors of a straightforward isotope production and decay scheme:

$$\delta A \simeq [\delta m^2+\delta C^2+\delta P_s{}^2+\delta F^2+\delta L^2+\delta \epsilon_p{}^2+\delta S_{ik}{}^2+\delta f^2+\delta Y^2+\delta \lambda^2]^{.5} + \delta_s$$

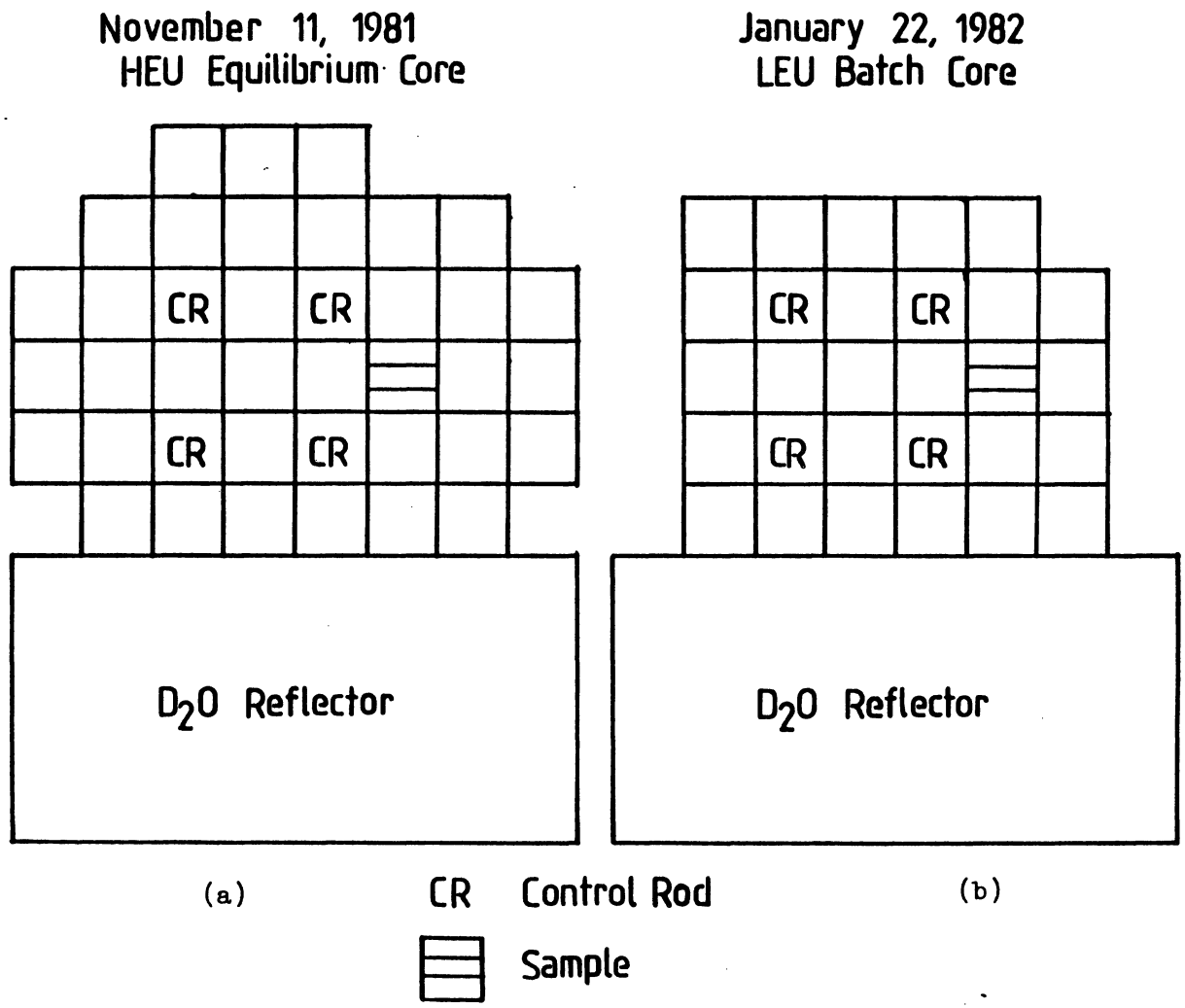


Figure 1 Core configurations for HEU and LEU special holder measurements.

Table 1.A

Saturated Activities for Reactions Dominated by
the Thermal/Epithermal Flux
HEU Special Assembly Sample Holder

| REACTION | BARE FOILS | | CADMIUM COVERED FOILS | | |
|---|---|---|---|---|---|
| | ACTIVITY (per sec.) | UNCERTAINTY (percent) | ACTIVITY (per sec.) | CADMIUM THICKNESS (mils) | UNCERTAINTY (percent) |
| $Fe^{58}(n,\gamma)$. (FP) | .287-10 | 4 | .209-11 | 20. | 4 |
| $Co^{59}(n,\gamma)$. (FP) | .813-09 | 5 | .113-09 | 20. | 5 |
| $Au^{197}(n,\gamma)$ | .400-08 | 8 | .220-08 | 20. | 4 |
| $Cu^{63}(n,\gamma)$. (FP) | .833-10 | 5 | .668-11[1] | 20. | 7 |
| $Mn^{55}(n,\gamma)$ | .249-09 | 5 | - | - | - |
| $Ag^{109}(n,\gamma)$ | .101-09 | 8 | .273-10 | 20. | 8 |
| $Ta^{181}(n,\gamma)$ | - | - | .622-09 | 20. | 8 |
| $W^{186}(n,\gamma)$ | .828-09 | 8 | .239-09 | 20. | 8 |
| $U^{238}(n,\gamma)$ | .270-09 | 9 | .234-09 | 20. | 9 |
| $Na^{23}(n,\gamma)$ | - | - | .484-12 | 40. | 11 |
| $U^{235}$(n,fission) | .106-07 | 10 | - | - | - |

| REACTION | BARE FOILS | | CADMIUM COVERED FOILS | | |
|---|---|---|---|---|---|
| | ACTIVITY (per sec.) | UNCERTAINTY (percent) | ACTIVITY (per sec.) | CADMIUM THICKNESS (mils) | UNCERTAINTY (percent) |
| $Pu^{239}(n,fission)$ | .185-07 | 10 | - | - | - |
| $Th^{232}(n,\gamma)$ | - | - | .720-10 | 20. | 8 |
| $Sc^{45}(n,\gamma)$ | .470-09 | 8 | .167-10 | 20. | 7 |
| $Lu^{176}(n,\gamma)$ | .724-07 | 7 | .130-08 | 20. | 6 |
| $Dy^{164}(n,\gamma)$ | .414-07 | 6 | .571-09 | 20. | 7 |
| $Dy^{156}(n,\gamma)$ | .167-08 | 5 | .106-08 | 20. | 5 |
| $Mo^{98}(n,\gamma)$ | - | - | .108-10 | 20. | 10 |
| $Zr^{94}(n,\gamma)$ | - | - | .547-12 | 20. | 4 |
| $Zn^{64}(n,\gamma)$ | - | - | .250-11 | 20. | 5 |
| $Zn^{68}(n,\gamma)$ | - | - | .352-12 | 20. | 10 |
| $Zr^{96}(n,\gamma)$ | - | - | .810-11 | 20. | 10 |

(1) The $Cu^{64}$ branching ratio is uncertain by 10-30% according to the literature. Our evaluations have shown this uncertainty must be much lower. The cadmium ratio should be reliable since it is independent of the branching ratio.

Table 1.B

Saturated Activities for Reactions Dominated by the Thermal/Epithermal Flux at the LEU Special Assembly Sample Holder

| REACTION | BARE FOILS | | CADMIUM COVERED FOILS | | |
|---|---|---|---|---|---|
| | ACTIVITY (per sec.) | UNCERTAINTY (percent) | ACTIVITY (per sec.) | CADMIUM (mils) | UNCERTAINTY (percent) |
| $Fe^{58}(n,\gamma)$. (FP)[1] | .263-10 | 5 | .219-11 | 25. | 5 |
| $Co^{59}(n,\gamma)$. (FP) | .806-09 | 5 | .120-09 | 25. | 5 |
| $Cu^{63}(n,\gamma)$. (FP) | - | - | .778-11 | 25. | 6 |
| $Mn^{55}(n,\gamma)$. (FP) | .261-09 | 7 | .243-10 | 25. | 5 |
| $Au^{197}(n,\gamma)$ | .373-08 | 8 | .224-08 | 20. | 8 |
| $Ag^{109}(n,\gamma)$ | .103-09 | 8 | .341-10 | 20. | 8 |
| $U^{238}(n,\gamma)$ | - | - | .232-09 | 25. | 6 |
| $U^{235}$(n,fission) | .960-08 | 8 | .470-09 | 25. | 8 |
| $Pu^{239}$(n,fission) | .180-07 | 8 | .590-09 | 25. | 8 |
| $Th^{232}(n,\gamma)$ | - | - | .800-10 | 25. | 5 |
| $Sc^{45}(n,\gamma)$ | .499-9 | 6 | - | - | - |

(1) The abbreviation "FP" means the measurements were made at full power (2MW).

Table 1.C

Saturated Activities for Reactions Dominated by
the Thermal/Epithermal Flux
LEU Special Assembly Sample Holder (Modified Core)

| REACTION | BARE FOILS | | CADMIUM COVERED FOILS | | |
|---|---|---|---|---|---|
| | ACTIVITY (per sec.) | UNCERTAINTY (percent) | ACTIVITY (per sec.) | CADMIUM THICKNESS (mils) | UNCERTAINTY (percent) |
| $Au^{197}(n,\gamma)$ | .428-8 | 8 | .209-8 | 20. | 8 |
| $Ag^{109}(n,\gamma)$ | .906-9 | 8 | .216-10 | 20. | 8 |
| $Ta^{181}(n,\gamma)$ | .905-9 | 6 | .566-9 | 20. | 6 |
| $W^{186}(n,\gamma)$ | .947-9 | 6 | - | - | - |
| $Sc^{45}(n,\gamma)$ | .519-9 | 7 | .168-10 | 20. | 7 |
| $Lu^{176}(n,\gamma)$ | .751-7 | 6 | - | - | - |
| $Dy^{164}(n,\gamma)$ | .430-7 | 6 | .462-9 | 20. | 6 |
| $In^{115}(n,\gamma)$ | - | - | .292-8 | 20. | 8 |
| $Cu^{63}(n,\gamma)$ | .792-10 | 5 | .624-11 | 20. | 7 |
| $Mn^{55}(n,\gamma)$ | .242-9 | 5 | .166-10 | 20. | 7 |

Table 2

Factors Used in Assessing the Uncertainty in the Activities

| Consideration | Symbol | Typical Error (%) |
|---|---|---|
| Irradiation Conditions | | |
| 1. Power reproducibility (full power) | $\delta P_s$ | 2% |
| Power calibration (low power) | | 6% |
| 2. Power ramp corrections | $\delta F$ | 1-2% |
| 3. Foil positioning errors | | 1-2% |
| Nuclear Parameters | | |
| 1. Half-life | $\delta\lambda$ | 1% |
| Effective half-life ($Co^{58}$) | | 4% |
| 2. Gamma branching ratios | $\delta f$ | 1-20% |
| 3. Number densities, isotopic abundance | $\delta N_i$ | 1% |
| 4. Fission yields | $\delta Y$ | 6-20% |
| Mass Determination | $\delta m$ | |
| 1. Mass measurements | | 0-1.2% |
| 2. Fissile/fertile material composition | | 1-3% |
| 3. Alloy compositions | | 1-2% |
| Counting Parameters | | |
| 1. Counting Statistics | $\delta C$ | 1-6% |
| 2. Absolute efficiency of detector | $\delta \epsilon^p$ | 6% |
| 3. Count rate corrections | $\delta L$ | <3-6% |
| 4. Sample geometry corrections | $\delta S$ | 1-10% |
| 5. Irradiation, counting, and wait times | | <1% |

Note: Errors are quoted for the 95% confidence level.

The symbols are defined in Table 2 , and the prefix $\delta$ implies the relative error in the quantity. In accordance with the ICRU guidelines, the term $\delta_s$ is defined to be the maximum conceivable systematic uncertainty in the measurement. Table 2 shows the factors considered in assessing the magnitudes of the uncertainties, along with representative values. Note that we have chosen to quote the uncertainties at the 95% confidence level, so that these values correspond to approximately twice (1.96) the conventional standard error. These estimates may appear significantly too large since several completely independent measurements of the same activity normally agreed to well within the quoted uncertainties. But for the determination of an absolute activity, both the relatively large systematic uncertainty in the absolute efficiency of the detector and the absolute power level can dominate. In addition, while many of the other factors are frequently small, the quadrature sum of several of these uncertainties together may not be insignificant. In light of our experiences, it would be quite surprising to find absolute activity measurements quoted with uncertainties on the order of one or two percent. Table 1.A also shows the estimated uncertainties in the measured activities. The full power measurements are noted using the initials "FP". Since these measurements do not require a power calibration factor, they have lower uncertainties associated with them. As mentioned above, the absolute copper activities should be viewed with caution since the gamma branching ratio has a large uncertainty quoted in the literature.

The saturated activities presented in Table 1.A are used directly for our unfolding of the flux. For some readers, the saturated activities may be most useful since these can be used as benchmarks for other unfolding approaches. However, recall that we have incorporated the ef-

fects of self-shielding in the cross sections instead of correcting the activities. Thus, users wishing to employ these activities in their own calculations must apply self-shielding corrections.

Table 1.B presents the activities which were measured in the clean LEU core presented in Figure 1, along with an estimate of the uncertainty in these values. Note that we have chosen to present only those reactions which were used in the unfoldings. That is, we have not included those reactions whose decay schemes or cross sections have very large uncertainties (such as the $Dy^{157}$ capture reaction). Table 1.C presents the activities measured in an even more compact LEU core. In this case, the four fuel elements along the far right column of the LEU core shown in Figure 1 were removed. Since the larger LEU core shown in Figure 1 is more comparable to the HEU core, we have chosen the data of Table 1.B as being representative of the LEU fuel.

Table 3 presents a comparison of the measured cadmium ratios for six reactions measured in HEU and LEU fuel. Through comparison of the HEU and LEU measured values, it is apparent that the LEU spectrum is measurably harder than the HEU spectrum. This can also be seen in the final column of Table 3 which shows the ratio of the HEU to LEU cadmium fractions. The cadmium fraction is the cadmium ratio minus one, and is crudely representative of the ratio of the sub-cadmium to epicadmium fluxes. Since the ratio of the cadmium fractions is a ratio of ratios, the uncertainty in these values is rather large, i.e. 10-15%. Nevertheless, the data consistently indicates the harder nature of the LEU spectrum.

Table 3 also shows the cadmium ratios which are predicted from the spectra calculated with the HAMMER code. The effects of self-shielding have been included in these calculations, so the measured and calculated cadmium ratios can be directly compared. These comparisons are quite

Table 3

Comparison of Cadmium Ratios for HEU and LEU
Foils Measured at the Sample Holder

| REACTION | POWER (FP/LP)[1] | HEU CADMIUM RATIO | | LEU CADMIUM RATIO | | CADMIUM FRACTION RATIO (HEU/LEU) | |
|---|---|---|---|---|---|---|---|
| | | MEASURED | PREDICTED | MEASURED | PREDICTED | MEASURED[3] | PREDICTED |
| $Fe^{58}(n,\gamma)$ | FP | 13.7 | 9.0 | 12.0 | 8.0 | 1.15 | 1.14 |
| $Co^{59}(n,\gamma)$ | FP | 7.2 | 6.5 | 6.7 | 5.9 | 1.08 | 1.12 |
| $Au^{197}(n,\gamma)$ | LP | 1.8 | 1.74 | 1.7 | 1.66 | 1.23 | 1.12 |
| $Ag^{109}(n,\gamma)$ | LP | 3.7 | 3.3 | 3.0 | 3.0 | 1.34 | 1.14 |
| $Mn^{55}(n,\gamma)$ | LP | 15.2[2] | 12.9 | 10.7 | 10.3 | 1.46 | 1.28 |
| $Cu^{63}(n,\gamma)$ | LP | 12.5 | 10. | 10.3[4] | 8.9 | 1.23 | 1.16 |

[1] The abbreviations FP and LP stand for full-power and low-power measurements.

[2] The $Mn^{55}$ HEU cadmium ratio has a large uncertainty due to a 15% uncertainty in the cadmium covered activity. This activity was not used for unfolding.

[3] The low power values have a larger uncertainty (12-15%) due to the additional uncertainty introduced in the power calibration.

[4] The LEU bare copper data have a large uncertainty and are not used for unfolding.

interesting since they show that the calculated spectrum is too hard compared to what the measurements indicate. This is most likely due to deficiencies in our analytic model. The HAMMER code performs a unit cell calculation with reflective boundary conditions. As a result, the effect of leakage on the spectrum is neglected. Since leakage tends to soften a spectrum, the calculated spectrum should be too hard. This is precisely what is observed. Since it is not critical that our calculated spectra agree precisely with our measurements, we have not pursued this further. However, it would be interesting to perform a similar calculation (for example, using ANISN) with a vacuum boundary condition for comparison.

Table 4.A presents a comparison of bare and cadmium covered saturated activities measured at the center of an HEU core in a regular fuel element, and in the special sample holder in an HEU core. The HEU core center measurements were made at 1 MW in the core configuration shown in Figure 2(a). Since these two sets of measurements were made at different core positions in cores with different fuel configurations, the absolute activities cannot be meaningfully compared. However, from an examination of the cadmium ratios, the spectrum can be seen to be slightly harder at the core center, as correctly predicted by the HAMMER calculations. The second half of Table 4.A shows threshold reaction data. While we shall compare the HEU and LEU threshold reaction data in Section 2 below, it is interesting to compare the data measured in a regular fuel element to that measured in the special fuel assembly sample holder. The HEU core center data has been normalized to the special sample holder data for comparison. The normalization factor was chosen to be the average value of the ratio of measured activity at the holder to the activity measured at the core center. If the fast spectrum is the same at both of these locations, then the normalized activities should be the same for the holder and core center measurements. The agreement

Table 4.A

Comparison of HEU Saturated Activities
at the Special Assembly Holder
Versus Core Center

| REACTION | HEU HOLDER | | HEU CORE CENTER[1] | |
|---|---|---|---|---|
| | BARE | CADMIUM COVERED | BARE | CADMIUM COVERED |
| NON-THRESHOLD REACTIONS | | | | |
| $Fe^{59}(n,\gamma)$ | .287-10 | .209-11 | .141-10 | .152-11 |
| $Cu^{63}(n,\gamma)$ | .833-10 | .668-11 | .453-10 | .467-11 |
| $Ag^{109}(n,\gamma)$ | .101-09 | .273-10 | .540-10 | - |
| NORMALIZED THRESHOLD REACTIONS | | | | |
| $Ti^{46}(n,p)$ | - | .157-12 | - | .160-12 |
| $Ti^{47}(n,p)$ | - | .273-12 | - | .239-12 |
| $Ti^{48}(n,p)$ | - | .422-14 | - | .439-14 |
| $Fe^{54}(n,p)$ | - | .117-11 | - | .116-11 |
| $Al^{27}(n,\alpha)$ | - | .961-14 | - | .937-14 |
| $Zr^{90}(n,2n)$ | - | .105-14 | - | .104-14 |
| $Ni^{58}(n,p)$ | - | .151-11 | - | .150-11 |
| $Ni^{58}(n,2n)$ | - | - | - | .309-16 |

[1] These measurements were made on another (see Figure 2(a)) equilibrium HEU core, but at 1 Megawatt. The measured saturated activities at the center of this core are normalized to the sample holder data as described in the text.

Table 4.B

Comparison of LEU Saturated Activities at the Special Assembly Sample Holder Versus Core Center

| REACTION | LEU HOLDER | | LEU CORE CENTER[1] | |
|---|---|---|---|---|
| | BARE | CADMIUM COVERED | BARE | CADMIUM COVERED |
| NON-THRESHOLD REACTION MEASUREMENTS | | | | |
| $Fe^{58}(n,\gamma)$ | .263-10 | .219-11 | .251-10<br>.217-10[4] | .293-11<br>.279-11[4] |
| $Co^{59}(n,\gamma)$ | .806-09 | .120-09 | .808-09[2]<br>.838-09 | .158-09[2]<br>.175-09 |
| THRESHOLD REACTION MEASUREMENTS[3] | | | | |
| $Fe^{54}(n,p)$ | - | .128-11 | - | .127-11 |
| $Co^{59}(n,p)$ | - | .217-13 | - | .226-13 |
| $Co^{59}(n,2n)$ | - | .301-14 | - | .306-14 |
| $Ti^{46}(n,p)$ | - | .174-12 | - | .185-12 |
| $Ti^{47}(n,p)$ | - | .330-12 | - | .303-12 |
| $Ti^{48}(n,p)$ | - | .445-14 | - | .490-14 |
| $Ni^{58}(n,p)$ | - | .178-11 | - | .181-11 |

[1] These LEU measurements were made on a different LEU core (2/9/84) by B. Heuser (see Figure 3).

[2] These LEU measurements were made on a different LEU core (5/10/83) B. Heuser (see Figure 3).

[3] The saturated activities for the core were decreased by a factor of .595 in order to compare with the sample holder values. The core activities have an uncertainty of 5-10%.

[4] These LEU measurements were made on a different LEU core (10/7/83) by B. Heuser. Other LEU iron cadmium ratios measured at the core center (6/27/83) vary from 8.0-8.3.

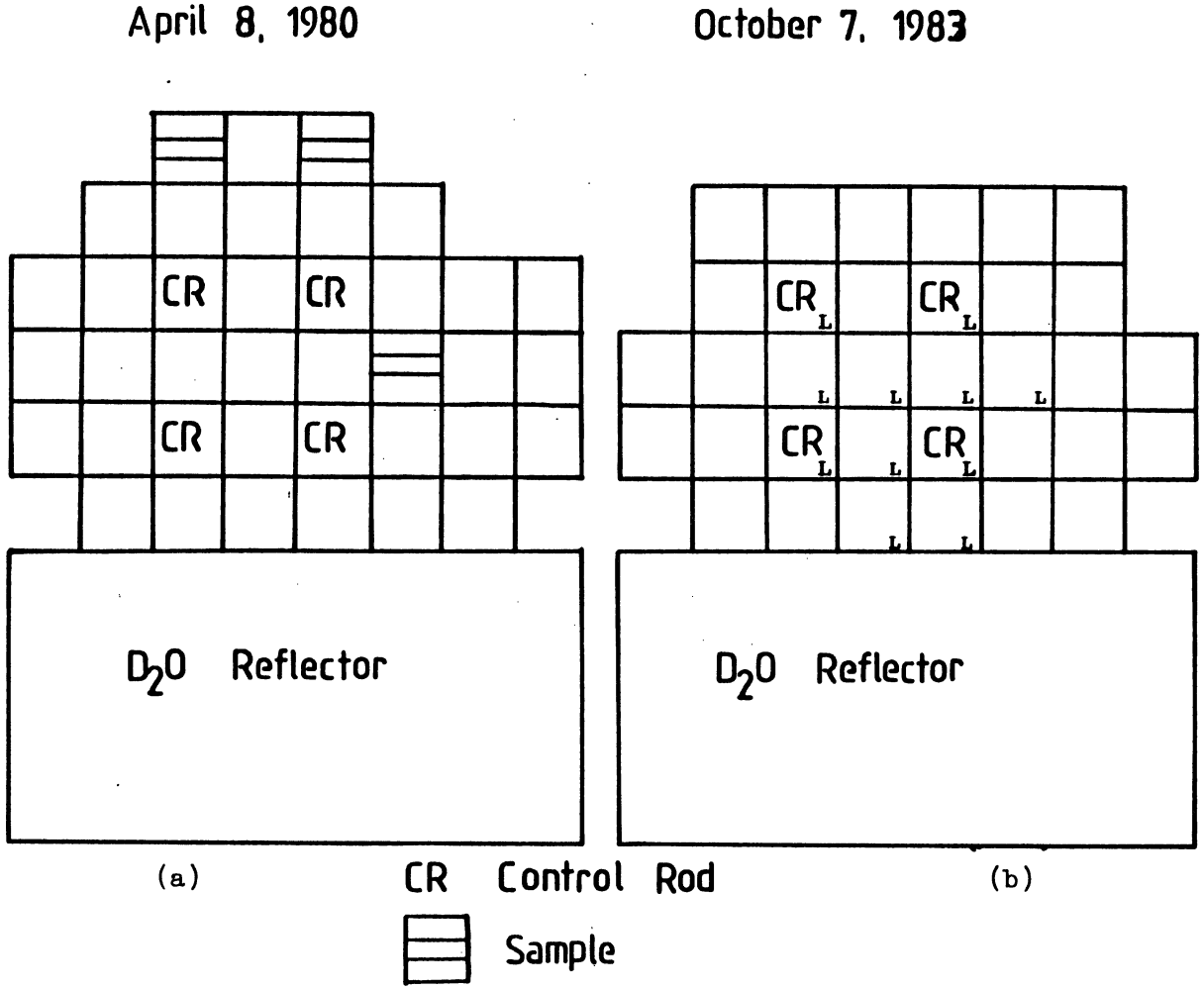


Figure 2 Core configuration for HEU and LEU regular assembly measurements.

between these data is remarkably good, and indicates that above a few MeV the fast spectrum in the special holder cannot be very different from the fast spectrum in a regular fuel element. While this is also expected based on the HAMMER results, it is nevertheless an experimental verification of our assumptions, as well as adding credibility to the accuracy of the measurements.

Table 4.B presents a comparison of bare and cadmium covered saturated activities measured at the center of an LEU core (shown in Figure 3(a)) and at the special assembly sample holder in the LEU core shown in Figure 1. These measurements also confirm that the spectrum is slightly harder at the core center, as expected. The measured threshold reaction data for the center of the LEU core was normalized to the LEU special holder data as described above. The LEU core center data have a greater uncertainty than the corresponding LEU holder data due to a larger uncertainty in the absolute detector efficiency. As a result, the 3.1% root-mean-squared difference between the LEU core center and LEU special holder of the threshold reaction data is larger than for the equivalent HEU data discussed above. Nevertheless, this data provide another verification that the spectrum above a few MeV will not be different from the spectrum at the core center.

Table 5 shows the average iron cadmium ratios for both HEU and LEU cores measured in the sample holder, at the core center, and in the heavy and light water reflectors. It is significant that the ratio of the HEU to LEU cadmium fractions are the same for the core and the sample holder. This corroborates our expectation that any spectral shift present at the core center will also be present at the special holder. Note that there is no spectral change observed in the heavy water reflector, and it is doubtful that any change would be observed in the light water reflector.

Table 6 compares the subcadmium fluxes measured in the

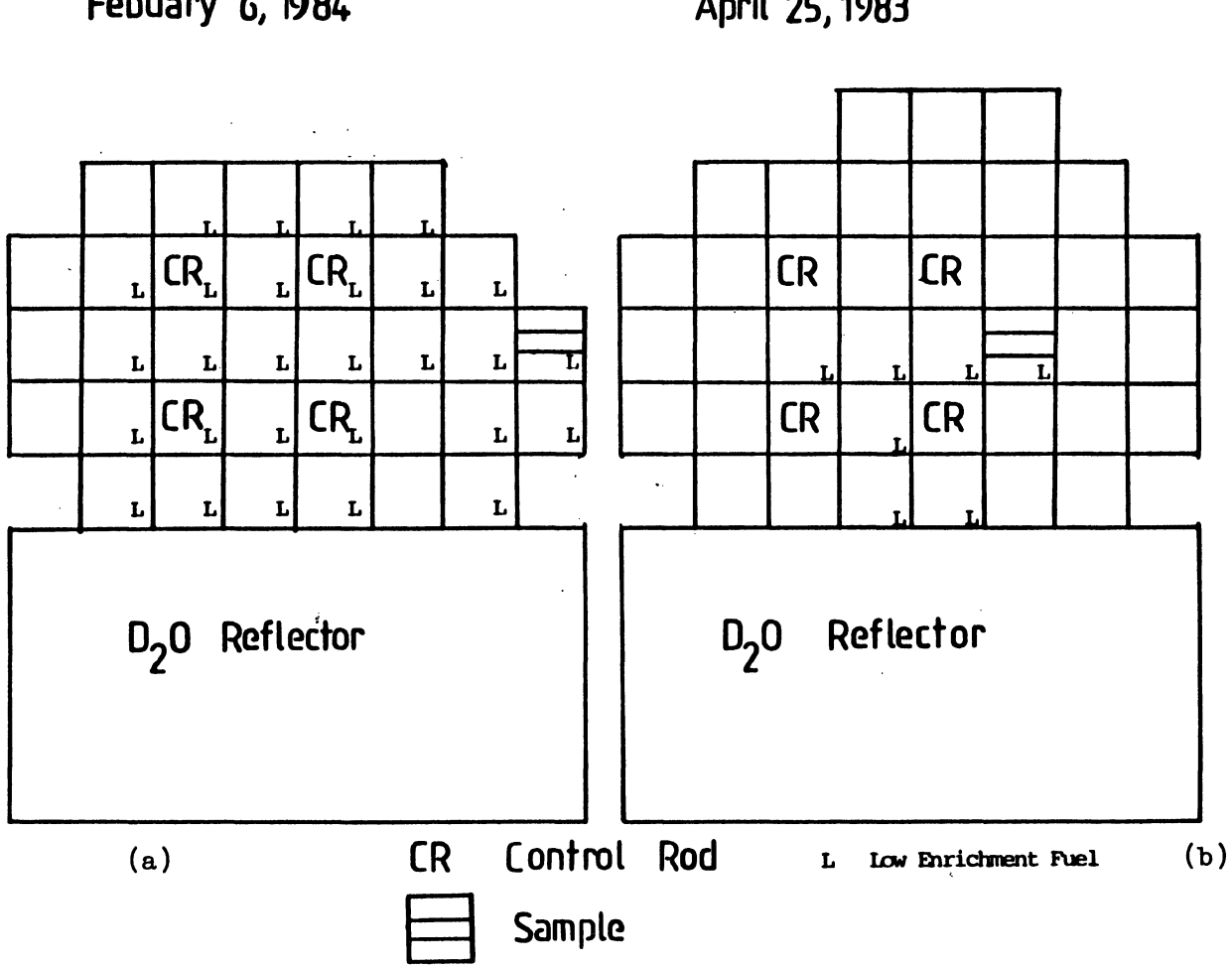


Figure 3 Core configurations for additional LEU measurements.

Table 5

Average Iron Cadmium Ratios
for HEU and LEU Cores

| Core Fuel | Sample Holder | Core[1] | $D_2O$[2] Reflector | $H_2O$[3] Reflector |
|---|---|---|---|---|
| HEU Fuel | 13.7 | 9.5 | 20. | - |
| LEU Fuel | 12.0[5] | 8.4 | 20. | 26. |
| Cad. Fraction[4] Ratio (HEU/LEU) | 1.15 | 1.15 | 1.0 | - |

[1] Measured between fuel plates of a regular fuel element in the center of the core. Quoted cadmium ratios are an average of 3 HEU and 2 LEU measurements made in the core.

[2] The heavy water reflector is adjacent to the edge of the core. Measurements were made 5 cm. radially into the heavy water reflector.

[3] Measurements were made 2.5 cm. away from the core boundary in the light water reflector.

[4] The cadmium fraction is the cadmium ratio minus one.

[5] For comparison, the cadmium ratio in the center of a water-filled special assembly was measured to be 20.

sample holder, using each of six capture reactions. The purpose here is to compare the consistency of the cross sections and flux measurements. The measured to calculated ratio is determined from:

$$\frac{A_b - A_c}{\int_0^\infty \sigma(E)G(E)(1-E_2(t(E)))\phi(E)dE}$$

Table 6

Comparison of Subcadmium Fluxes
Measured by Different Reactions

| REACTION | HEU MEASURED/CALCULATED | LEU MEASURED/CALCULATED |
|---|---|---|
| $Fe^{58}(n,\gamma)$ | 1.11 | 1.14 |
| $Co^{59}(n,\gamma)$ | 1.01 | 1.02 |
| $Au^{197}(n,\gamma)$ | .97 | .95 |
| $Ag^{109}(n,\gamma)$ | 1.02 | 1.02 |
| $Mn^{55}(n,\gamma)$ | - | 1.02 |
| $Cu^{64}(n,\gamma)$ | .97 | - |

where $A_b$ and $A_c$ are the measured bare and cadmium covered saturated activities per unit target nucleus, $\sigma(E)$ is the reaction cross section, G(E) is the self-shielding factor, t(E) is the thickness of the cadmium cover measured in mean free paths, $E_2$ is an exponential integral, and $\phi(E)$ is energy-dependent flux calculated by HAMMER. Note that to within a multiplicative constant, the denominator is the effective subcadmium cross section. While the resulting agreement shown in Table 6 is remarkably good between the reactions, we do find that iron is displaced from the average by about 10%. This difference is also corroborated by measurements made at the center of HEU and LEU cores which showed the iron subcadmium flux to be 16% larger than predicted by copper, and 7% larger than the value determined from cobalt. All of our previous measurements[1-2] which have made use of the iron cross section will give a subcadmium flux which is about 10% too high. Thus, we conclude that the ENDF-IV iron capture cross section may be approximately 10% too small at thermal energies.

## 2. Fast Flux Reaction Rate Data Measured in HEU and LEU Cores

Threshold reaction data have already been presented in Tables 4.A and 4.B for the center of the HEU and LEU cores. We have seen that there is negligible evidence that the fast spectrum will be different in the sample holder than in a regular fuel element. In this section, we shall compare HEU and LEU threshold reaction data measured in the sample holder, and can assume these comparisons are valid for regular fuel elements. Table 7 presents a comprehensive set of threshold reaction data for measurements made in the special assembly sample holders for the HEU and LEU cores shown in Figure 1. After normalizing the HEU and LEU solid holder data, the data agree to within a standard deviation of 5%. This is significant because it again confirms that down to approximately .5 MeV, there will be very little spectral difference between the HEU and LEU cores.

Also shown in Table 7 is data taken in the air-filled sample holder in the LEU core shown in Figure 2(b). This data has a larger uncertainty associated with it, but includes the interesting $Pt^{195}(n,n')$ reaction. This reaction has a very low threshold energy (~.1 MeV), and will be helpful in defining the spectrum below 1 MeV when the cross section is known to greater precision. If the hollow holder data are normalized to the LEU solid holder data, the two data sets agree to within a standard deviation of 8.8%. While this agreement is not as impressive as the comparison above, it implies that the solid aluminum around the threshold foils does not significantly perturb the fast spectrum. But recall the shielding correction is given by:

$$G(E) = \frac{(1-2E_3(\Sigma(E)t))}{2\Sigma(E)t}$$

Table 7

Saturated Activities
for Reactions Dominated by the
Fast Flux

| REACTION | HEU SOLID HOLDER | LEU SOLID HOLDER | LEU HOLLOW HOLDER |
|---|---|---|---|
| $Fe^{54}(n,\alpha)$ | .115-13 | .132-13 | - |
| $Fe^{54}(n,p)$ | .117-11 | .128-11 | .101-11 |
| $Fe^{56}(n,p)$ | - | .173-13 | .108-13 |
| $Al^{27}(n,\alpha)$ | .961-14 | .112-13 | .742-14 |
| $Ti^{46}(n,p)$ | .157-12 | .174-12 | .120-12 |
| $Ti^{47}(n,p)$ | .273-12 | .330-12 | .236-12 |
| $Ti^{48}(n,p)$ | .422-14 | .445-14 | .308-14 |
| $Zn^{64}(n,p)$ | .484-12 | .503-12 | .322-12 |
| $Mg^{24}(n,p)$ | .215-13 | .225-13 | .135-13 |
| $Ni^{58}(n,p)$ | .151-11 | .178-11 | .112-11 |
| $Zr^{90}(n,2n)$ | .105-14 | .117-14 | - |
| $Np^{237}(n,fission)$ | .234-10 | .265-10 | - |
| $U^{238}(n,fission)$ | .432-11 | .490-11 | - |
| $Th^{232}(n,fission)$ | .113-11 | .132-11 | - |
| $In^{115}(n,n')$ | - | .307-11 | .279-11 |
| $Pt^{195}(n,n')$ | - | - | .518-12 |
| $V^{51}(n,\alpha)$ | - | .290-15 | - |
| $Co^{59}(n,p)$ | - | .217-13 | - |
| $Mn^{55}(n,2n)$ | - | .390-14 | - |
| $Ni^{60}(n,p)$ | .251-13[1] | .405-13 | - |
| $Ni^{58}(n,2n)$ | - | .532-16 | - |

| REACTION | HEU SOLID HOLDER | LEU SOLID HOLDER | LEU HOLLOW HOLDER |
|---|---|---|---|
| $Co^{59}(n,2n)$ | - | .301-14 | - |
| $Cu^{63}(n,\alpha)$ | .600-14 | - | - |
| $Al^{27}(n,p)$ | - | .635-13 | - |
| $Rh^{103}(n,p)$ | .155-15 | - | - |

(1) Measured value has a 20% uncertainty associated with it.

where $\Sigma(E)$ is the macroscopic total cross section for aluminum, and t is the mean chord length for the solid holder. Using this expression, one can show that the perturbation of the solid aluminum holder on the fast flux should be negligibly small. Thus, the agreement between the hollow holder data and the solid holder data is not unexpected.

3. Thermal and Epithermal Unfolded Spectra

The unfolded HEU and LEU spectra are presented in this section. The semi-empirical unfolding technique was chosen for the deconvolutions since this approach allows the experimentalist to construct the unfolded spectrum on a foil-by-foil basis. The advantage of this approach is clearly shown in the discussion of the LEU spectrum below. Since both the LEU and HEU deconvolutions share the same unfolding parameters, we shall discuss our unfolding philosophy once prior to the presentation of both sets of results.

The semi-empirical technique iteratively refines the spectrum until the specified convergence criteria are met. Based on experience, we have chosen to limit the maximum number of allowed iterations to convergence to 15, and have defined convergence to occur when the average deviation between the measured and calculated activities is 5% or less. These criteria may appear too relaxed since the fitting residue would continue to decrease if the number of iterations were allowed to increase. However, our experience has shown that past a certain point, the unfolded spectra may develop spurious structure by radically changing the flux in energy groups which have relatively little impact on the foil activities -- such as between 10 keV and .5 MeV. In order to compensate for these unphysical peaks and/or valleys, the spectra are normally "smoothed" (sometimes quite heavily) since one expects the flux to be fairly smooth. For instance, the flux at an energy group may be defined to be the average of several points on either side of the

group. While the smoothing washes out these erroneous excursions, the resulting spectrum may not necessarily be a better approximation to the true spectrum. However, by limiting the maximum number of iterations, and defining convergence to have occurred when the average difference between the measured and calculated (based on the unfolded spectrum) activity is 5%, the generation of spurious structure caused by the unfolding technique can be avoided. Because of this conservative approach, the spectra do not need to be heavily "smoothed" to remove unphysical features.

In the spectra which are presented below, we have chosen to use Monte Carlo error analysis techniques. In this approach, the activities, cross sections, and input spectrum are randomly perturbed to within predefined limits, and then this new unfolding problem is solved. This scheme is repeated 10-20 times, and the results are used to generate the estimates of the uncertainties in the unfolded flux. While the limits of the perturbations on the cross sections and activities are the known uncertainties in these values, appropriate uncertainty limits for the input spectrum are more difficult. It is our belief that the input flux at any one group is known a priori to within a factor of 2-10. This is an order of magnitude smaller than the inverse sensitivity method would predict. By limiting the input flux perturbations to these lower limits, our quoted uncertainties are believed to be more realistic.

We have chosen to unfold the detailed fast spectrum separately from the thermal and epithermal spectrum. This is desirable since there is too much activation data to perform a complete flux unfolding with an associated error analysis. This will not affect the accuracy of the thermal and epithermal fluxes which are presented. We have performed the thermal and epithermal flux unfoldings with all the measured threshold reactions, but without the error analysis, and then compared this result to the unfoldings

with only a few threshold reactions. The addition of these threshold reactions does not change the HEU thermal and epithermal results presented below. For the LEU thermal and epithermal spectrum below, the inclusion of all measured threshold reactions increased the integral fast flux above 1 MeV by 4.0% above the result quoted below, but does not alter the shape or the magnitude of the spectrum below 1 MeV.

The results of the HEU thermal and epithermal unfoldings are shown in Tables 8 and 9 and Figure 4. Table 8 shows the non-threshold reactions which were used and the energy span in which 90% of the activity is produced. Also shown is a comparison of the measured activity to the activity calculated with the unfolded spectrum. The final column shows the percentage deviation of the measured activity from the calculated activity. Note that with very few exceptions, this agreement is quite acceptable (<5%). One particularly interesting result is the $Fe^{58}(n,\gamma)$ cadmium covered data shown in the first row of Table 8. This datum is fit reasonably well by the unfolded spectrum. This implies that the iron capture reaction inconsistency shown in Table 6 is probably not related to an error in the isotopic abundance, but is more likely attributable to the cross section we have used. Kirk[3] et. al. have also noted the limited accuracy of the $Fe^{58}(n,\gamma)$ cross section.

Figure 4 shows the measured HEU spectrum with the lethargy dependent flux plotted on a linear scale. This spectrum is harder than the HAMMER calculated spectrum, as expected. We shall defer comments about the physical meaning of the small fluctuations in the resonance energy region until after presenting the LEU results. However, without the rather substantial corrections discussed for self-shielding, gamma counting, and power calibrations, the spectrum would have large oscillations which would require considerable smoothing to remove. Table 9 presents the values for the measured HEU differential and integral

Table 8. Comparison of HEU Unfolded Activities with Measured Activities

| REACTION | FOIL COVER TYPE | ENERGY LIMITS 90% ACTIVITY | | CALCULATED UNFOLDED ACTIVITY | RATIO MEASURED TO CALCULATED ACTIVITIES | DEVIATION MEASURED FROM CALCULATED |
|---|---|---|---|---|---|---|
| | | LOWER (MEV) | UPPER (MEV) | | | |
| FE58(N,G)FE59 | CADMIUM | 8.291E-07 | 3.509E-04 | 2.140E-12 | 0.9768 | -2.32 |
| CO59(N,G)CO60 | BARE | 9.315E-09 | 1.079E-04 | 7.993E-10 | 1.0172 | 1.72 |
| CO59(N,G)CO60 | CADMIUM | 1.476E-06 | 1.488E-04 | 1.143E-10 | 0.9885 | -1.15 |
| AU197(N,G)AU198 | BARE | 1.626E-08 | 6.016E-06 | 4.062E-09 | 0.9848 | -1.52 |
| AU197(N,G)AU198 | CADMIUM | 4.324E-06 | 1.725E-05 | 2.231E-09 | 0.9859 | -1.41 |
| U238(N,G)U239 | BARE | 4.288E-08 | 1.231E-04 | 2.760E-10 | 0.9780 | -2.20 |
| U238(N,G)U239 | CADMIUM | 6.963E-06 | 1.426E-04 | 2.210E-10 | 1.0600 | 6.00 |
| TH232(N,G)TH233 | CADMIUM | 2.237E-05 | 1.882E-03 | 7.176E-11 | 1.0033 | 0.33 |
| CU63(N,G)CU64 | BARE | 8.689E-09 | 3.934E-07 | 8.938E-11 | 0.9711 | -2.89 |
| MN55(N,G)MN56 | BARE | 8.620E-09 | 2.507E-07 | 2.564E-10 | 0.9711 | -2.89 |
| SC45(N,G)SC46 | BARE | 8.361E-09 | 1.496E-07 | 4.831E-10 | 0.9729 | -2.71 |
| SC45(N,G)SC46 | CADMIUM | 5.184E-07 | 3.425E-05 | 1.721E-11 | 0.9702 | -2.98 |
| LU176(N,G)LU177 | BARE | 1.882E-08 | 1.618E-07 | 7.652E-08 | 0.9462 | -5.38 |
| LU176(N,G)LU177 | CADMIUM | 1.315E-06 | 9.030E-05 | 1.352E-09 | 0.9614 | -3.86 |
| DY164(N,G)DY165M | BARE | 7.923E-09 | 1.118E-07 | 4.308E-08 | 0.9609 | -3.91 |
| DY164(N,G)DY165M | CADMIUM | 3.895E-07 | 4.106E-06 | 5.483E-10 | 1.0414 | 4.14 |
| NA23(N,G)NA24 | CADMIUM | 7.758E-07 | 3.164E-03 | 4.817E-13 | 1.0049 | 0.49 |
| U235(N,F)FSPR | BARE | 7.657E-09 | 1.480E-07 | 1.065E-08 | 0.9956 | -0.44 |
| PU239(N,F)FSPR | BARE | 1.042E-08 | 3.176E-07 | 1.797E-08 | 1.0296 | 2.96 |
| AG109(N,G)AG110M | BARE | 1.148E-08 | 5.926E-06 | 9.801E-11 | 1.0305 | 3.05 |
| AG109(N,G)AG110M | CADMIUM | 2.738E-06 | 2.933E-04 | 2.762E-11 | 0.9884 | -1.16 |
| TA181(N,G)TA182 | CADMIUM | 3.252E-06 | 2.386E-04 | 6.188E-10 | 1.0051 | 0.51 |
| W186(N,G)W187 | BARE | 1.072E-08 | 1.847E-05 | 9.007E-10 | 0.9192 | -8.08 |
| W186(N,G)W187 | CADMIUM | 6.513E-06 | 2.854E-05 | 2.345E-10 | 1.0193 | 1.93 |
| NP237(N,F)FSPR | CADMIUM | 6.754E-01 | 4.171E+00 | 2.343E-11 | 0.9990 | -0.10 |

Table 9

HEU Unfolded Sample Holder Flux
Thermal and Epithermal

| GROUP | ENERGY (MEV) | DIFFERENTIAL FLUX | | INTEGRAL FLUX | | | |
|---|---|---|---|---|---|---|---|
| | | | | ABOVE E | | BELOW E | |
| | | ($n/cm^2$-sec-MeV) | δ(%) | ($n/cm^2$-sec) | δ(%) | ($n/cm^2$-sec) | δ(%) |
| 1 | 1.00E-10 | 9.803E+18 | 9.1 | 6.355E+13 | 6.6 | 8.917E+09 | 9.1 |
| 2 | 1.00E-09 | 1.020E+20 | 7.2 | 6.355E+13 | 6.6 | 9.399E+11 | 7.2 |
| 3 | 1.00E-08 | 2.255E+20 | 5.8 | 6.262E+13 | 6.7 | 3.922E+12 | 6.1 |
| 4 | 2.30E-08 | 2.435E+20 | 4.6 | 5.963E+13 | 7.0 | 1.059E+13 | 5.1 |
| 5 | 5.00E-08 | 1.736E+20 | 2.8 | 5.296E+13 | 7.7 | 1.514E+13 | 4.1 |
| 6 | 7.60E-08 | 8.782E+19 | 7.8 | 4.842E+13 | 8.4 | 1.851E+13 | 2.9 |
| 7 | 1.15E-07 | 3.545E+19 | 10.5 | 4.505E+13 | 9.0 | 2.041E+13 | 2.6 |
| 8 | 1.70E-07 | 1.510E+19 | 15.9 | 4.315E+13 | 9.4 | 2.167E+13 | 2.8 |
| 9 | 2.55E-07 | 7.429E+18 | 17.5 | 4.189E+13 | 9.5 | 2.262E+13 | 3.1 |
| 10 | 3.80E-07 | 4.240E+18 | 9.1 | 4.093E+13 | 9.5 | 2.340E+13 | 3.1 |
| 11 | 5.50E-07 | 2.698E+18 | 8.0 | 4.016E+13 | 9.6 | 2.425E+13 | 3.0 |
| 12 | 8.40E-07 | 1.656E+18 | 10.0 | 3.931E+13 | 9.7 | 2.497E+13 | 3.1 |
| 13 | 1.27E-06 | 1.006E+18 | 19.1 | 3.859E+13 | 9.9 | 2.555E+13 | 3.3 |
| 14 | 1.90E-06 | 6.744E+17 | 6.2 | 3.801E+13 | 10.2 | 2.615E+13 | 3.3 |
| 15 | 2.80E-06 | 4.411E+17 | 10.4 | 3.741E+13 | 10.4 | 2.676E+13 | 3.2 |
| 16 | 4.25E-06 | 2.860E+17 | 4.9 | 3.680E+13 | 10.6 | 2.735E+13 | 3.1 |
| 17 | 6.30E-06 | 1.958E+17 | 8.0 | 3.620E+13 | 10.7 | 2.791E+13 | 3.1 |
| 18 | 9.20E-06 | 1.343E+17 | 12.1 | 3.564E+13 | 10.9 | 2.843E+13 | 3.2 |
| 19 | 1.35E-05 | 8.374E+16 | 21.2 | 3.513E+13 | 11.1 | 2.905E+13 | 3.0 |
| 20 | 2.10E-05 | 5.481E+16 | 15.7 | 3.450E+13 | 11.1 | 2.955E+13 | 2.8 |
| 21 | 3.00E-05 | 3.986E+16 | 5.7 | 3.400E+13 | 11.1 | 3.016E+13 | 2.7 |
| 22 | 4.50E-05 | 2.564E+16 | 14.6 | 3.339E+13 | 11.3 | 3.080E+13 | 2.5 |
| 23 | 6.90E-05 | 1.739E+16 | 13.4 | 3.276E+13 | 11.4 | 3.134E+13 | 2.3 |

| GROUP | ENERGY (MEV) | DIFFERENTIAL FLUX | | INTEGRAL FLUX | | | |
|---|---|---|---|---|---|---|---|
| | | | | ABOVE E | | BELOW E | |
| | | (n/cm$^2$-sec-MeV) | δ(%) | (n/cm$^2$-sec) | δ(%) | (n/cm$^2$-sec) | δ(%) |
| 24 | 1.00E-04 | 1.341E+16 | 7.8 | 3.221E+13 | 11.5 | 3.181E+13 | 2.3 |
| 25 | 1.35E-04 | 1.062E+16 | 6.5 | 3.174E+13 | 11.7 | 3.218E+13 | 2.3 |
| 26 | 1.70E-04 | 7.718E+15 | 10.5 | 3.137E+13 | 11.8 | 3.255E+13 | 2.2 |
| 27 | 2.20E-04 | 6.116E+15 | 29.3 | 3.101E+13 | 11.9 | 3.285E+13 | 2.1 |
| 28 | 2.80E-04 | 4.802E+15 | 26.9 | 3.071E+13 | 12.3 | 3.317E+13 | 2.1 |
| 29 | 3.60E-04 | 3.725E+15 | 11.6 | 3.038E+13 | 12.6 | 3.349E+13 | 2.0 |
| 30 | 4.50E-04 | 2.912E+15 | 18.1 | 3.007E+13 | 12.6 | 3.383E+13 | 2.0 |
| 31 | 5.75E-04 | 2.322E+15 | 17.3 | 2.972E+13 | 12.6 | 3.426E+13 | 1.9 |
| 32 | 7.60E-04 | 1.816E+15 | 16.2 | 2.930E+13 | 12.6 | 3.461E+13 | 1.9 |
| 33 | 9.60E-04 | 1.449E+15 | 19.1 | 2.895E+13 | 12.7 | 3.504E+13 | 2.0 |
| 34 | 1.27E-03 | 1.174E+15 | 22.0 | 2.851E+13 | 12.7 | 3.540E+13 | 2.0 |
| 35 | 1.60E-03 | 1.034E+15 | 24.8 | 2.816E+13 | 12.6 | 3.575E+13 | 2.1 |
| 36 | 2.00E-03 | 9.497E+14 | 31.5 | 2.780E+13 | 12.6 | 3.626E+13 | 2.3 |
| 37 | 2.70E-03 | 7.179E+14 | 29.6 | 2.729E+13 | 12.7 | 3.665E+13 | 2.6 |
| 38 | 3.40E-03 | 4.550E+14 | 18.6 | 2.690E+13 | 12.8 | 3.711E+13 | 2.7 |
| 39 | 4.50E-03 | 3.126E+14 | 11.6 | 2.645E+13 | 12.8 | 3.742E+13 | 2.8 |
| 40 | 5.50E-03 | 2.211E+14 | 12.4 | 2.614E+13 | 12.9 | 3.780E+13 | 2.8 |
| 41 | 7.20E-03 | 1.691E+14 | 11.1 | 2.576E+13 | 13.1 | 3.815E+13 | 2.8 |
| 42 | 9.20E-03 | 1.397E+14 | 13.7 | 2.540E+13 | 13.3 | 3.853E+13 | 2.8 |
| 43 | 1.20E-02 | 1.194E+14 | 16.1 | 2.502E+13 | 13.5 | 3.889E+13 | 2.9 |
| 44 | 1.50E-02 | 1.026E+14 | 16.0 | 2.466E+13 | 13.6 | 3.932E+13 | 3.0 |
| 45 | 1.90E-02 | 7.602E+13 | 14.9 | 2.424E+13 | 13.6 | 3.984E+13 | 3.1 |
| 46 | 2.55E-02 | 5.127E+13 | 16.4 | 2.372E+13 | 13.7 | 4.019E+13 | 3.2 |
| 47 | 3.20E-02 | 4.169E+13 | 16.2 | 2.337E+13 | 13.7 | 4.052E+13 | 3.3 |
| 48 | 4.00E-02 | 4.238E+13 | 17.9 | 2.303E+13 | 13.8 | 4.104E+13 | 3.4 |
| 49 | 5.25E-02 | 3.957E+13 | 20.0 | 2.252E+13 | 13.9 | 4.154E+13 | 3.6 |
| 50 | 6.60E-02 | 2.842E+13 | 18.6 | 2.201E+13 | 14.1 | 4.216E+13 | 3.9 |

| GROUP | ENERGY (MEV) | DIFFERENTIAL FLUX | | INTEGRAL FLUX | | | |
|---|---|---|---|---|---|---|---|
| | | | | ABOVE E | | BELOW E | |
| | | (n/cm$^2$-sec-MeV) | δ(%) | (n/cm$^2$-sec) | δ(%) | (n/cm$^2$-sec) | δ(%) |
| 51 | 8.80E-02 | 2.246E+13 | 19.1 | 2.140E+13 | 14.2 | 4.264E+13 | 4.0 |
| 52 | 1.10E-01 | 2.128E+13 | 19.9 | 2.091E+13 | 14.3 | 4.317E+13 | 4.2 |
| 53 | 1.35E-01 | 1.836E+13 | 20.2 | 2.039E+13 | 14.5 | 4.362E+13 | 4.4 |
| 54 | 1.60E-01 | 1.579E+13 | 20.9 | 1.993E+13 | 14.6 | 4.408E+13 | 4.5 |
| 55 | 1.90E-01 | 1.562E+13 | 21.3 | 1.947E+13 | 14.7 | 4.454E+13 | 4.7 |
| 56 | 2.20E-01 | 1.538E+13 | 21.5 | 1.902E+13 | 14.9 | 4.506E+13 | 4.9 |
| 57 | 2.55E-01 | 1.497E+13 | 21.2 | 1.849E+13 | 15.1 | 4.557E+13 | 5.1 |
| 58 | 2.90E-01 | 1.444E+13 | 20.4 | 1.798E+13 | 15.3 | 4.600E+13 | 5.2 |
| 59 | 3.20E-01 | 1.369E+13 | 19.2 | 1.756E+13 | 15.4 | 4.654E+13 | 5.4 |
| 60 | 3.60E-01 | 1.261E+13 | 19.3 | 1.701E+13 | 15.6 | 4.705E+13 | 5.5 |
| 61 | 4.00E-01 | 1.150E+13 | 20.7 | 1.651E+13 | 15.7 | 4.762E+13 | 5.6 |
| 62 | 4.50E-01 | 1.127E+13 | 22.7 | 1.593E+13 | 15.7 | 4.819E+13 | 5.7 |
| 63 | 5.00E-01 | 1.177E+13 | 24.5 | 1.537E+13 | 15.7 | 4.878E+13 | 5.7 |
| 64 | 5.50E-01 | 1.194E+13 | 26.2 | 1.478E+13 | 15.6 | 4.937E+13 | 5.8 |
| 65 | 6.00E-01 | 1.163E+13 | 27.6 | 1.418E+13 | 15.5 | 5.007E+13 | 5.9 |
| 66 | 6.60E-01 | 1.115E+13 | 28.9 | 1.348E+13 | 15.4 | 5.074E+13 | 6.0 |
| 67 | 7.20E-01 | 1.055E+13 | 30.0 | 1.282E+13 | 15.3 | 5.136E+13 | 6.0 |
| 68 | 7.80E-01 | 9.825E+12 | 31.1 | 1.219E+13 | 15.3 | 5.195E+13 | 6.1 |
| 69 | 8.40E-01 | 9.076E+12 | 32.1 | 1.160E+13 | 15.3 | 5.267E+13 | 6.2 |
| 70 | 9.20E-01 | 8.330E+12 | 30.9 | 1.089E+13 | 15.6 | 5.332E+13 | 6.4 |
| 71 | 1.00E+00 | 7.271E+12 | 26.1 | 1.023E+13 | 15.9 | 5.473E+13 | 6.6 |
| 72 | 1.20E+00 | 6.083E+12 | 22.1 | 8.819E+12 | 16.7 | 5.591E+13 | 6.7 |
| 73 | 1.40E+00 | 5.174E+12 | 21.4 | 7.646E+12 | 17.6 | 5.690E+13 | 6.8 |
| 74 | 1.60E+00 | 4.360E+12 | 27.3 | 6.659E+12 | 18.5 | 5.769E+13 | 6.9 |
| 75 | 1.80E+00 | 3.862E+12 | 40.9 | 5.863E+12 | 17.7 | 5.835E+13 | 7.0 |
| 76 | 2.00E+00 | 3.334E+12 | 42.8 | 5.206E+12 | 14.9 | 5.919E+13 | 7.1 |
| 77 | 2.30E+00 | 2.685E+12 | 28.4 | 4.361E+12 | 9.6 | 5.993E+13 | 7.1 |

| GROUP | ENERGY (MEV) | DIFFERENTIAL FLUX | | INTEGRAL FLUX | | | |
|---|---|---|---|---|---|---|---|
| | | | | ABOVE E | | BELOW E | |
| | | (n/cm$^2$-sec-MeV) | δ(%) | (n/cm$^2$-sec) | δ(%) | (n/cm$^2$-sec) | δ(%) |
| 78 | 2.60E+00 | 2.096E+12 | 14.8 | 3.626E+12 | 6.8 | 6.055E+13 | 7.1 |
| 79 | 2.90E+00 | 1.593E+12 | 11.0 | 3.007E+12 | 6.1 | 6.119E+13 | 7.0 |
| 80 | 3.30E+00 | 1.228E+12 | 10.9 | 2.361E+12 | 5.7 | 6.170E+13 | 6.9 |
| 81 | 3.70E+00 | 9.752E+11 | 8.4 | 1.853E+12 | 5.8 | 6.209E+13 | 6.8 |
| 82 | 4.10E+00 | 8.074E+11 | 7.8 | 1.463E+12 | 6.5 | 6.240E+13 | 6.8 |
| 83 | 4.50E+00 | 6.478E+11 | 6.6 | 1.157E+12 | 7.1 | 6.270E+13 | 6.7 |
| 84 | 5.00E+00 | 5.005E+11 | 7.4 | 8.501E+11 | 7.8 | 6.294E+13 | 6.7 |
| 85 | 5.50E+00 | 3.739E+11 | 9.1 | 6.113E+11 | 8.1 | 6.312E+13 | 6.7 |
| 86 | 6.00E+00 | 2.555E+11 | 9.3 | 4.319E+11 | 8.1 | 6.329E+13 | 6.6 |
| 87 | 6.70E+00 | 1.536E+11 | 9.0 | 2.608E+11 | 8.6 | 6.339E+13 | 6.6 |
| 88 | 7.40E+00 | 9.188E+10 | 9.1 | 1.589E+11 | 10.0 | 6.346E+13 | 6.6 |
| 89 | 8.20E+00 | 5.222E+10 | 9.8 | 8.985E+10 | 13.0 | 6.350E+13 | 6.6 |
| 90 | 9.00E+00 | 2.788E+10 | 11.1 | 5.098E+10 | 18.4 | 6.353E+13 | 6.6 |
| 91 | 1.00E+01 | 1.427E+10 | 10.9 | 2.529E+10 | 30.8 | 6.354E+13 | 6.6 |
| 92 | 1.10E+01 | 7.400E+09 | 16.6 | 1.229E+10 | 51.8 | 6.355E+13 | 6.6 |
| 93 | 1.20E+01 | 3.780E+09 | 36.8 | 5.767E+09 | 80.6 | 6.355E+13 | 6.6 |
| 94 | 1.30E+01 | 1.997E+09 | 65.6 | 2.738E+09 | 110.5 | 6.355E+13 | 6.6 |
| 95 | 1.40E+01 | 1.138E+09 | 96.5 | 1.382E+09 | 135.4 | 6.355E+13 | 6.6 |
| 96 | 1.50E+01 | 7.630E+08 | 126.5 | 7.643E+08 | 153.4 | 6.355E+13 | 6.6 |
| 97 | 1.60E+01 | 6.406E+08 | 153.9 | 4.485E+08 | 165.2 | 6.355E+13 | 6.6 |
| 98 | 1.70E+01 | 5.339E+08 | 171.7 | 2.540E+08 | 171.9 | 6.355E+13 | 6.6 |
| 99 | 1.80E+01 | 4.308E+08 | 181.8 | 1.263E+08 | 172.1 | 6.355E+13 | 6.6 |
| 100 | 1.90E+01 | 1.434E+08 | 145.6 | 3.712E+07 | 145.6 | 6.355E+13 | 6.6 |

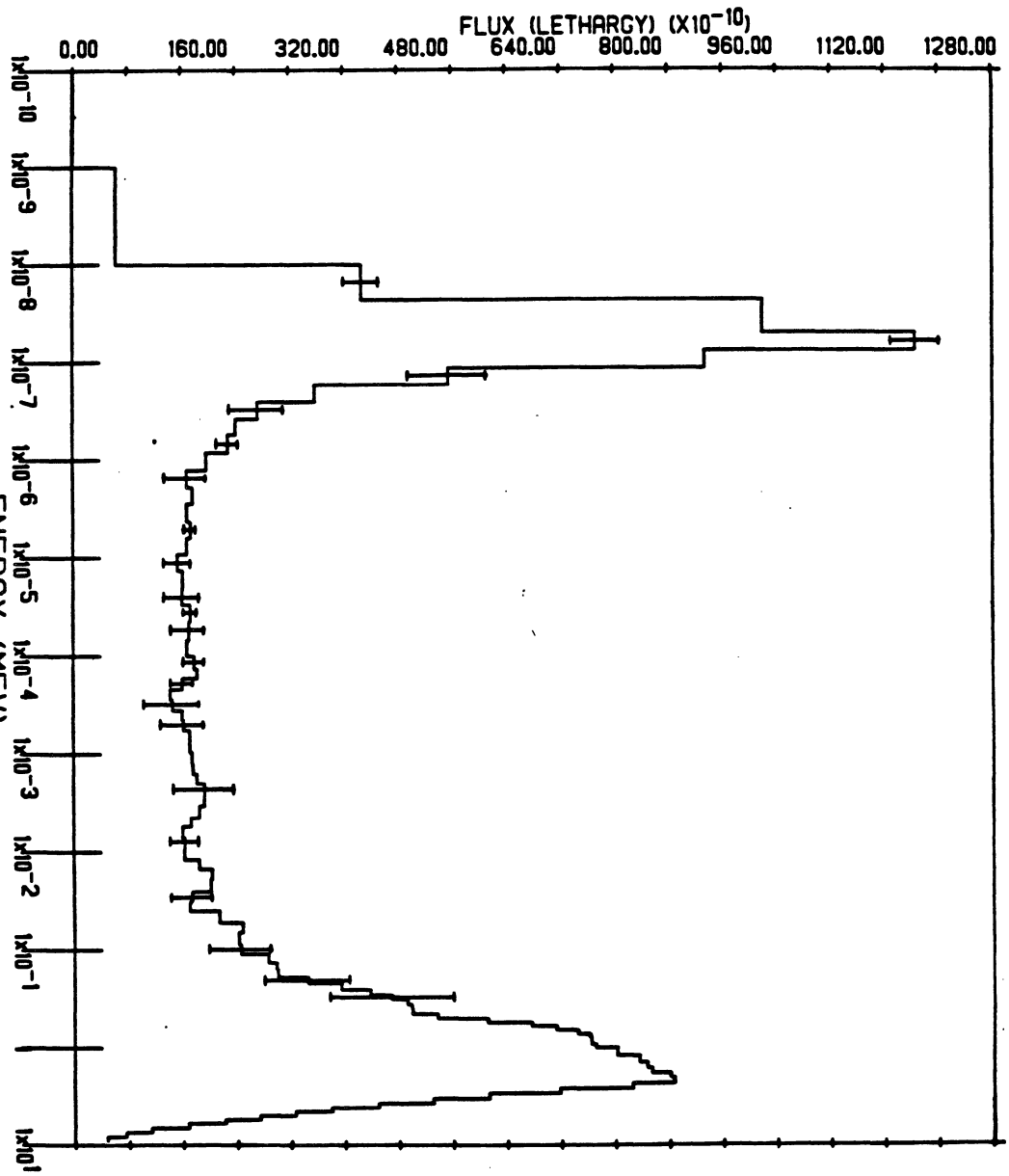


Figure 4 FNR unfolded HEU Spectrum.

fluxes, as well as their uncertainties. Note that the uncertainties in the differential flux tend to vary significantly between groups for energies above .25 eV and below 10 keV. These fluctuations are probably due to the presence of resonances in these groups which serve to enhance the sensitivity of the measurements there. For instance, the effect of the gold resonance at 4.9 eV is evidenced by a sharply lower uncertainty in that energy group. At energies above 9 MeV, the uncertainty in the unfolded flux increases dramatically. This is caused by the limited number of reactions which were used to provide sensitivity in this energy region. In the next section we shall present more accurate measurements of the differential fast fluxes. The last four columns of Table 9 show the integral fluxes above (and including), and below (and including) each energy group. These results will be used later to compare the broad group fluxes in the HEU and LEU cores. In summary, based on the agreement between the measured and calculated activities, and the reasonable shape of the spectrum, we have accepted these results as the measured HEU spectrum. Since it has been our experience that the solution of the unfolding problem using one technique is also recognized as a solution using other techniques, we have not compared these results with the results using other approaches.

The LEU thermal and epithermal flux unfoldings highlight the advantage of using our interactive unfolding approach. Using all the data shown in Table 1.B, there were large unphysical fluctuations in the unfolded flux between .2 and 10 keV. To understand the source of this problem, we began with the twelve reactions with measured to calculated deviations less than five percent, and iteratively added a reaction and then performed the unfolding. Each unfolded spectrum can be used as the input spectrum for the next foil addition. Figure 5 shows the results when the cadmium covered manganese data is entered. This activity was calcu-

lated to be about 6% too large using the spectrum predicted by the remaining activation data. The dashed curve represents the initial input spectrum, and the solid curve is the resulting solution spectrum. The fraction of the total cadmium covered manganese activity produced in each energy group is also shown superimposed as a dashed curve upon the input and solution spectra. The majority of the manganese activity is produced in the 337 eV resonance, and to a lesser extent in the 1.080 keV resonance. Since the flux was well determined in the group containing the 337 eV resonance, the differential flux had to be perturbed more substantially in those groups which were not well determined. Note the significant perturbation which has occurred to the spectrum above 50 keV to compensate for only a 6% discrepancy between the measured and calculated manganese activity. This is a pathological problem with reactor spectral unfolding. As the number of measured activities increases, the consistency of the activities and cross sections must increase to prevent such magnified perturbations.

Table 10 shows the non-threshold reactions which were used in the final LEU fittings. The fit is not as impressive as the HEU unfolding, but still meets the convergence criteria which were defined. Table 11 presents the LEU results in a comparable format to the HEU results presented in Table 9. The uncertainties in these values are comparable to those presented for the HEU results. Figure 6 shows the unfolded LEU thermal and epithermal fluxes. As with the HEU results, the spectrum above 1 MeV is unfolded in greater detail in the next section.

Figure 7 compares the unfolded HEU and LEU spectra. The two spectra are normalized to have the same integral flux above 1 MeV. Beginning at 1 MeV and moving to lower energies, note the remarkable similarity between the spectra. In the region down to .1 MeV, this is principally a reflection of the agreement in the HAMMER calculated

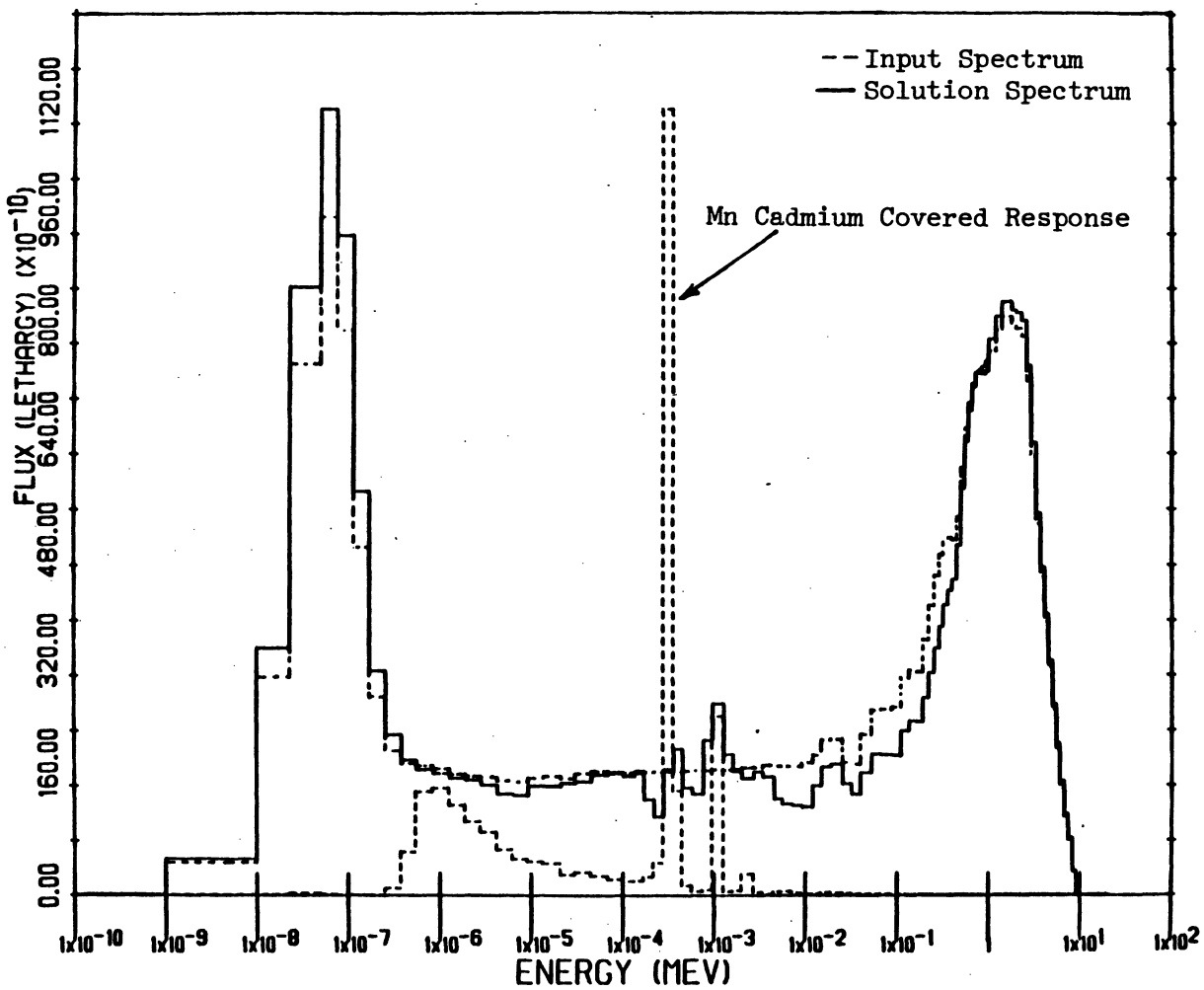


Figure 5 Iterative unfolding example using Mn.

Table 10

Comparison of LEU Unfolded Activities with Measured Activities

| REACTION | FOIL COVER TYPE | ENERGY LIMITS 90% ACTIVITY | | CALCULATED UNFOLDED ACTIVITY | RATIO MEASURED TO CALCULATED ACTIVITIES | DEVIATION MEASURED FROM CALCULATED (%) |
|---|---|---|---|---|---|---|
| | | LOWER (MEV) | UPPER (MEV) | | | |
| U235(N,F)FSPR | BARE | 8.042E-09 | 1.551E-07 | 1.058E-08 | 0.9077 | -9.23 |
| PU239(N,F)FSPR | BARE | 1.094E-08 | 3.155E-07 | 1.798E-08 | 1.0013 | 0.13 |
| U235(N,F)FSPR | CADMIUM | 7.997E-07 | 3.628E-03 | 4.523E-10 | 1.0392 | 3.92 |
| PU239(N,F)FSPR | CADMIUM | 4.080E-07 | 1.541E-03 | 5.710E-10 | 1.0333 | 3.33 |
| NP237(N,F)FSPR | CADMIUM | 6.760E-01 | 4.098E+00 | 2.642E-11 | 1.0029 | 0.29 |
| CU63(N,G)CU64 | CADMIUM | 1.044E-06 | 7.603E-03 | 8.056E-12 | 0.9657 | -3.43 |
| MN55(N,G)MN56 | BARE | 9.130E-09 | 2.997E-07 | 2.569E-10 | 1.0159 | 1.59 |
| CO59(N,G)CO60 | BARE | 9.926E-09 | 1.109E-04 | 8.058E-10 | 1.0003 | 0.03 |
| CO59(N,G)CO60 | CADMIUM | 2.104E-06 | 1.492E-04 | 1.201E-10 | 0.9990 | -0.10 |
| FE58(N,G)FE59 | BARE | 9.260E-09 | 7.367E-07 | 2.369E-11 | 1.1102 | 11.02 |
| FE58(N,G)FE59 | CADMIUM | 1.135E-06 | 3.521E-04 | 2.349E-12 | 0.9323 | -6.77 |
| U238(N,G)U239 | CADMIUM | 7.013E-06 | 1.720E-04 | 2.377E-10 | 0.9759 | -2.41 |
| TH232(N,G)TH233 | CADMIUM | 2.257E-05 | 1.850E-03 | 7.920E-11 | 1.0101 | 1.01 |
| AU197(N,G)AU198 | BARE | 1.711E-08 | 6.031E-06 | 4.066E-09 | 0.9296 | -7.04 |
| AU197(N,G)AU198 | CADMIUM | 4.321E-06 | 1.367E-05 | 2.245E-09 | 0.9980 | -0.20 |
| AG109(N,G)AG110M | BARE | 1.207E-08 | 6.012E-06 | 9.852E-11 | 1.0404 | 4.04 |
| SC45(N,G)SC46 | BARE | 8.795E-09 | 1.531E-07 | 4.807E-10 | 1.0382 | 3.82 |

Table 11

LEU Unfolded Sample Holder Flux
Thermal and Epithermal

| GROUP | ENERGY (MEV) | DIFFERENTIAL FLUX | | INTEGRAL FLUX | | | |
|---|---|---|---|---|---|---|---|
| | | | | ABOVE E | | BELOW E | |
| | | (n/cm$^2$-sec-MeV) | δ(%) | (n/cm$^2$-sec) | δ(%) | (n/cm$^2$-sec) | δ(%) |
| 1 | 1.00E-10 | 9.438E+18 | 8.7 | 6.878E+13 | 4.8 | 8.211E+09 | 8.7 |
| 2 | 1.00E-09 | 9.878E+19 | 6.7 | 6.877E+13 | 4.8 | 8.750E+11 | 6.7 |
| 3 | 1.00E-08 | 2.201E+20 | 5.9 | 6.791E+13 | 4.8 | 3.691E+12 | 6.0 |
| 4 | 2.30E-08 | 2.424E+20 | 5.3 | 6.509E+13 | 5.0 | 1.015E+13 | 5.5 |
| 5 | 5.00E-08 | 1.809E+20 | 4.7 | 5.863E+13 | 5.4 | 1.480E+13 | 5.3 |
| 6 | 7.60E-08 | 1.001E+20 | 3.9 | 5.398E+13 | 5.9 | 1.865E+13 | 4.9 |
| 7 | 1.15E-07 | 4.156E+19 | 4.9 | 5.013E+13 | 6.3 | 2.089E+13 | 4.4 |
| 8 | 1.70E-07 | 1.603E+19 | 14.7 | 4.789E+13 | 6.5 | 2.222E+13 | 4.0 |
| 9 | 2.55E-07 | 7.438E+18 | 20.4 | 4.656E+13 | 6.5 | 2.315E+13 | 3.7 |
| 10 | 3.80E-07 | 4.236E+18 | 13.8 | 4.563E+13 | 6.6 | 2.389E+13 | 3.5 |
| 11 | 5.50E-07 | 2.716E+18 | 7.8 | 4.489E+13 | 6.8 | 2.470E+13 | 3.4 |
| 12 | 8.40E-07 | 1.758E+18 | 8.0 | 4.408E+13 | 6.9 | 2.546E+13 | 3.4 |
| 13 | 1.27E-06 | 1.147E+18 | 8.8 | 4.332E+13 | 7.1 | 2.618E+13 | 3.3 |
| 14 | 1.90E-06 | 7.787E+17 | 7.7 | 4.261E+13 | 7.2 | 2.689E+13 | 3.3 |
| 15 | 2.80E-06 | 5.036E+17 | 7.7 | 4.189E+13 | 7.4 | 2.765E+13 | 3.3 |
| 16 | 4.25E-06 | 2.967E+17 | 5.9 | 4.114E+13 | 7.6 | 2.826E+13 | 3.2 |
| 17 | 6.30E-06 | 1.926E+17 | 8.1 | 4.052E+13 | 7.8 | 2.884E+13 | 3.1 |
| 18 | 9.20E-06 | 1.371E+17 | 13.6 | 3.994E+13 | 7.9 | 2.947E+13 | 3.0 |
| 19 | 1.35E-05 | 8.975E+16 | 10.0 | 3.932E+13 | 8.0 | 3.014E+13 | 2.9 |
| 20 | 2.10E-05 | 6.403E+16 | 12.7 | 3.864E+13 | 8.1 | 3.071E+13 | 2.9 |
| 21 | 3.00E-05 | 4.646E+16 | 14.7 | 3.807E+13 | 8.1 | 3.139E+13 | 2.8 |
| 22 | 4.50E-05 | 3.090E+16 | 10.5 | 3.739E+13 | 8.2 | 3.214E+13 | 2.9 |
| 23 | 6.90E-05 | 2.110E+16 | 8.9 | 3.664E+13 | 8.2 | 3.281E+13 | 2.9 |

| GROUP | ENERGY (MEV) | DIFFERENTIAL FLUX | | INTEGRAL FLUX | | | |
|---|---|---|---|---|---|---|---|
| | | | | ABOVE E | | BELOW E | |
| | | (n/cm$^2$-sec-MeV) | δ(%) | (n/cm$^2$-sec) | δ(%) | (n/cm$^2$-sec) | δ(%) |
| 24 | 1.00E-04 | 1.446E+16 | 12.1 | 3.597E+13 | 8.4 | 3.332E+13 | 2.9 |
| 25 | 1.35E-04 | 1.144E+16 | 9.2 | 3.546E+13 | 8.6 | 3.372E+13 | 2.9 |
| 26 | 1.70E-04 | 7.277E+15 | 15.5 | 3.506E+13 | 8.8 | 3.410E+13 | 2.8 |
| 27 | 2.20E-04 | 5.089E+15 | 59.8 | 3.468E+13 | 8.9 | 3.439E+13 | 2.7 |
| 28 | 2.80E-04 | 5.719E+15 | 21.7 | 3.439E+13 | 9.1 | 3.483E+13 | 2.7 |
| 29 | 3.60E-04 | 5.275E+15 | 12.9 | 3.395E+13 | 9.3 | 3.529E+13 | 2.7 |
| 30 | 4.50E-04 | 3.062E+15 | 16.1 | 3.350E+13 | 9.3 | 3.567E+13 | 2.7 |
| 31 | 5.75E-04 | 2.179E+15 | 20.8 | 3.311E+13 | 9.3 | 3.607E+13 | 2.8 |
| 32 | 7.60E-04 | 2.588E+15 | 22.5 | 3.271E+13 | 9.4 | 3.655E+13 | 2.8 |
| 33 | 9.60E-04 | 2.495E+15 | 31.4 | 3.223E+13 | 9.3 | 3.724E+13 | 2.9 |
| 34 | 1.27E-03 | 1.461E+15 | 21.0 | 3.155E+13 | 8.9 | 3.769E+13 | 3.0 |
| 35 | 1.60E-03 | 1.002E+15 | 17.8 | 3.109E+13 | 8.8 | 3.809E+13 | 3.1 |
| 36 | 2.00E-03 | 7.157E+14 | 20.3 | 3.069E+13 | 8.8 | 3.858E+13 | 3.2 |
| 37 | 2.70E-03 | 6.144E+14 | 17.8 | 3.020E+13 | 8.9 | 3.901E+13 | 3.3 |
| 38 | 3.40E-03 | 4.523E+14 | 17.1 | 2.977E+13 | 8.8 | 3.951E+13 | 3.4 |
| 39 | 4.50E-03 | 2.860E+14 | 15.7 | 2.927E+13 | 8.8 | 3.980E+13 | 3.4 |
| 40 | 5.50E-03 | 2.127E+14 | 16.3 | 2.898E+13 | 8.9 | 4.018E+13 | 3.4 |
| 41 | 7.20E-03 | 1.696E+14 | 16.0 | 2.860E+13 | 9.1 | 4.053E+13 | 3.4 |
| 42 | 9.20E-03 | 1.343E+14 | 19.8 | 2.825E+13 | 9.2 | 4.090E+13 | 3.4 |
| 43 | 1.20E-02 | 1.251E+14 | 17.5 | 2.788E+13 | 9.3 | 4.127E+13 | 3.5 |
| 44 | 1.50E-02 | 1.184E+14 | 17.5 | 2.751E+13 | 9.4 | 4.174E+13 | 3.6 |
| 45 | 1.90E-02 | 9.383E+13 | 17.3 | 2.704E+13 | 9.4 | 4.235E+13 | 3.8 |
| 46 | 2.55E-02 | 6.265E+13 | 18.5 | 2.644E+13 | 9.5 | 4.275E+13 | 3.9 |
| 47 | 3.20E-02 | 4.736E+13 | 16.1 | 2.603E+13 | 9.5 | 4.313E+13 | 4.0 |
| 48 | 4.00E-02 | 4.530E+13 | 16.7 | 2.565E+13 | 9.5 | 4.369E+13 | 4.1 |
| 49 | 5.25E-02 | 4.124E+13 | 18.0 | 2.509E+13 | 9.6 | 4.425E+13 | 4.2 |
| 50 | 6.60E-02 | 3.189E+13 | 19.2 | 2.453E+13 | 9.5 | 4.496E+13 | 4.4 |

| GROUP | ENERGY (MEV) | DIFFERENTIAL FLUX | | INTEGRAL FLUX | | | |
|---|---|---|---|---|---|---|---|
| | | | | ABOVE E | | BELOW E | |
| | | (n/cm$^2$-sec-MeV) | δ(%) | (n/cm$^2$-sec) | δ(%) | (n/cm$^2$-sec) | δ(%) |
| 51 | 8.80E-02 | 2.491E+13 | 20.4 | 2.382E+13 | 9.5 | 4.551E+13 | 4.5 |
| 52 | 1.10E-01 | 2.365E+13 | 22.0 | 2.327E+13 | 9.5 | 4.611E+13 | 4.7 |
| 53 | 1.35E-01 | 2.063E+13 | 23.4 | 2.267E+13 | 9.4 | 4.663E+13 | 4.8 |
| 54 | 1.60E-01 | 1.716E+13 | 24.2 | 2.215E+13 | 9.3 | 4.715E+13 | 5.0 |
| 55 | 1.90E-01 | 1.656E+13 | 24.8 | 2.163E+13 | 9.3 | 4.766E+13 | 5.1 |
| 56 | 2.20E-01 | 1.603E+13 | 25.4 | 2.112E+13 | 9.3 | 4.823E+13 | 5.3 |
| 57 | 2.55E-01 | 1.528E+13 | 25.5 | 2.056E+13 | 9.3 | 4.877E+13 | 5.5 |
| 58 | 2.90E-01 | 1.450E+13 | 25.1 | 2.001E+13 | 9.4 | 4.922E+13 | 5.6 |
| 59 | 3.20E-01 | 1.358E+13 | 24.1 | 1.957E+13 | 9.5 | 4.977E+13 | 5.8 |
| 60 | 3.60E-01 | 1.234E+13 | 23.2 | 1.901E+13 | 9.6 | 5.028E+13 | 5.9 |
| 61 | 4.00E-01 | 1.109E+13 | 22.5 | 1.850E+13 | 9.7 | 5.085E+13 | 6.1 |
| 62 | 4.50E-01 | 1.070E+13 | 22.0 | 1.793E+13 | 9.9 | 5.141E+13 | 6.2 |
| 63 | 5.00E-01 | 1.104E+13 | 20.8 | 1.737E+13 | 10.0 | 5.198E+13 | 6.3 |
| 64 | 5.50E-01 | 1.111E+13 | 19.1 | 1.680E+13 | 10.1 | 5.256E+13 | 6.3 |
| 65 | 6.00E-01 | 1.075E+13 | 17.6 | 1.622E+13 | 10.2 | 5.324E+13 | 6.4 |
| 66 | 6.60E-01 | 1.024E+13 | 16.4 | 1.554E+13 | 10.4 | 5.388E+13 | 6.4 |
| 67 | 7.20E-01 | 9.632E+12 | 15.3 | 1.490E+13 | 10.6 | 5.449E+13 | 6.4 |
| 68 | 7.80E-01 | 8.947E+12 | 14.5 | 1.429E+13 | 10.8 | 5.505E+13 | 6.5 |
| 69 | 8.40E-01 | 8.250E+12 | 13.7 | 1.373E+13 | 11.0 | 5.575E+13 | 6.5 |
| 70 | 9.20E-01 | 7.623E+12 | 12.9 | 1.303E+13 | 11.2 | 5.639E+13 | 6.4 |
| 71 | 1.00E+00 | 6.908E+12 | 11.8 | 1.239E+13 | 11.5 | 5.785E+13 | 6.4 |
| 72 | 1.20E+00 | 6.076E+12 | 10.7 | 1.093E+13 | 12.3 | 5.914E+13 | 6.3 |
| 73 | 1.40E+00 | 5.393E+12 | 10.2 | 9.646E+12 | 13.1 | 6.028E+13 | 6.2 |
| 74 | 1.60E+00 | 4.762E+12 | 10.2 | 8.502E+12 | 13.9 | 6.129E+13 | 6.1 |
| 75 | 1.80E+00 | 4.198E+12 | 10.6 | 7.492E+12 | 14.7 | 6.218E+13 | 6.0 |
| 76 | 2.00E+00 | 3.696E+12 | 11.3 | 6.602E+12 | 15.4 | 6.335E+13 | 5.8 |
| 77 | 2.30E+00 | 3.203E+12 | 12.4 | 5.427E+12 | 16.5 | 6.437E+13 | 5.7 |

| GROUP | ENERGY (MEV) | DIFFERENTIAL FLUX | | INTEGRAL FLUX | | | |
|---|---|---|---|---|---|---|---|
| | | | | ABOVE E | | BELOW E | |
| | | ($n/cm^2$-sec-MeV) | δ(%) | ($n/cm^2$-sec) | δ(%) | ($n/cm^2$-sec) | δ(%) |
| 78 | 2.60E+00 | 2.632E+12 | 13.6 | 4.409E+12 | 17.6 | 6.521E+13 | 5.5 |
| 79 | 2.90E+00 | 1.998E+12 | 14.9 | 3.574E+12 | 18.7 | 6.605E+13 | 5.4 |
| 80 | 3.30E+00 | 1.498E+12 | 16.4 | 2.730E+12 | 19.9 | 6.668E+13 | 5.3 |
| 81 | 3.70E+00 | 1.159E+12 | 17.8 | 2.098E+12 | 21.0 | 6.717E+13 | 5.1 |
| 82 | 4.10E+00 | 9.044E+11 | 19.1 | 1.611E+12 | 22.0 | 6.755E+13 | 5.1 |
| 83 | 4.50E+00 | 6.841E+11 | 20.4 | 1.231E+12 | 22.9 | 6.791E+13 | 5.0 |
| 84 | 5.00E+00 | 5.049E+11 | 21.8 | 8.728E+11 | 23.9 | 6.817E+13 | 4.9 |
| 85 | 5.50E+00 | 3.674E+11 | 23.1 | 6.091E+11 | 24.9 | 6.836E+13 | 4.9 |
| 86 | 6.00E+00 | 2.505E+11 | 24.4 | 4.176E+11 | 25.7 | 6.855E+13 | 4.8 |
| 87 | 6.70E+00 | 1.618E+11 | 25.8 | 2.354E+11 | 26.7 | 6.866E+13 | 4.8 |
| 88 | 7.40E+00 | 1.033E+11 | 27.2 | 1.181E+11 | 27.6 | 6.875E+13 | 4.8 |
| 89 | 8.20E+00 | 3.978E+10 | 28.6 | 3.275E+10 | 28.6 | 6.878E+13 | 4.8 |

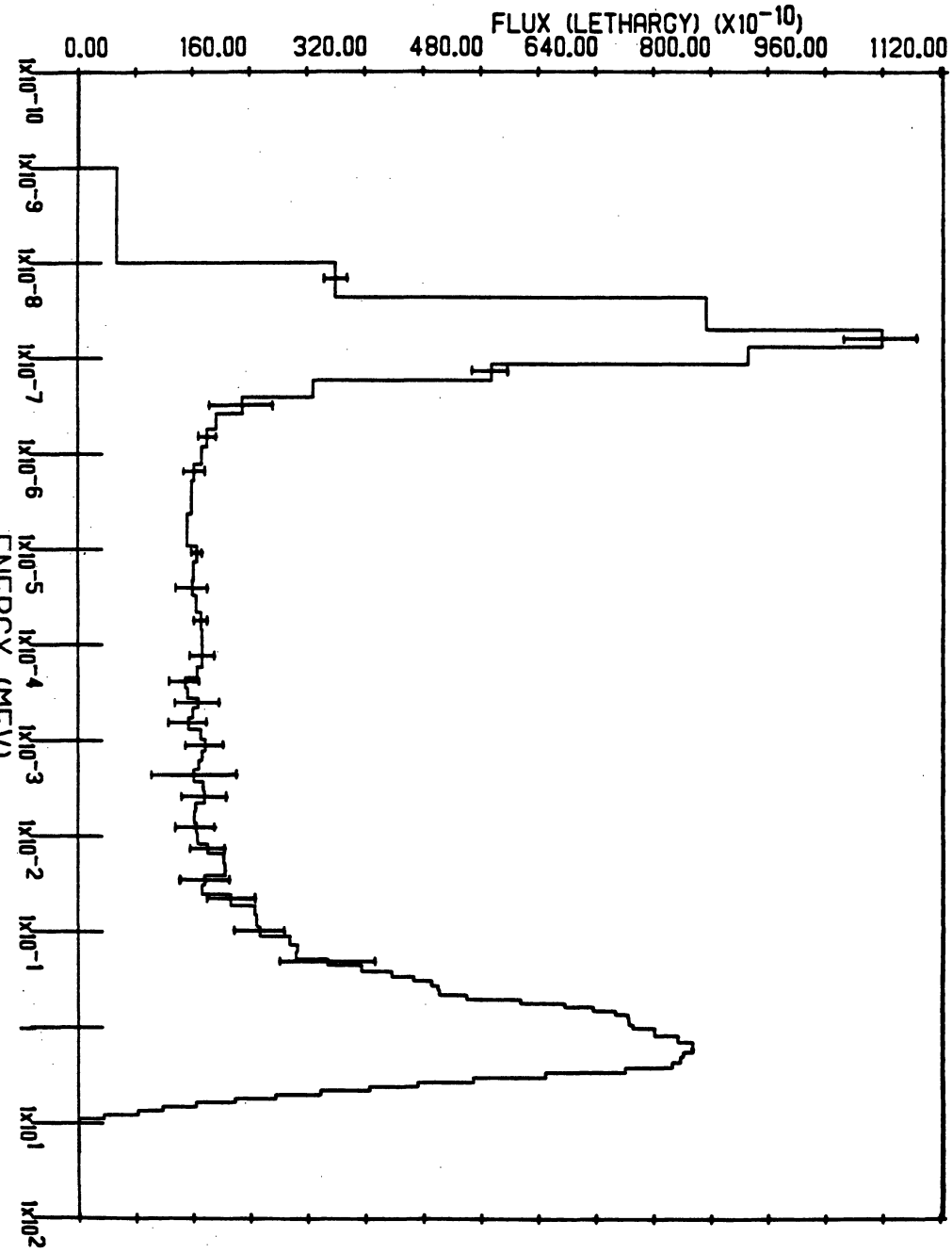


Figure 6 FNR unfolded LEU spectrum.

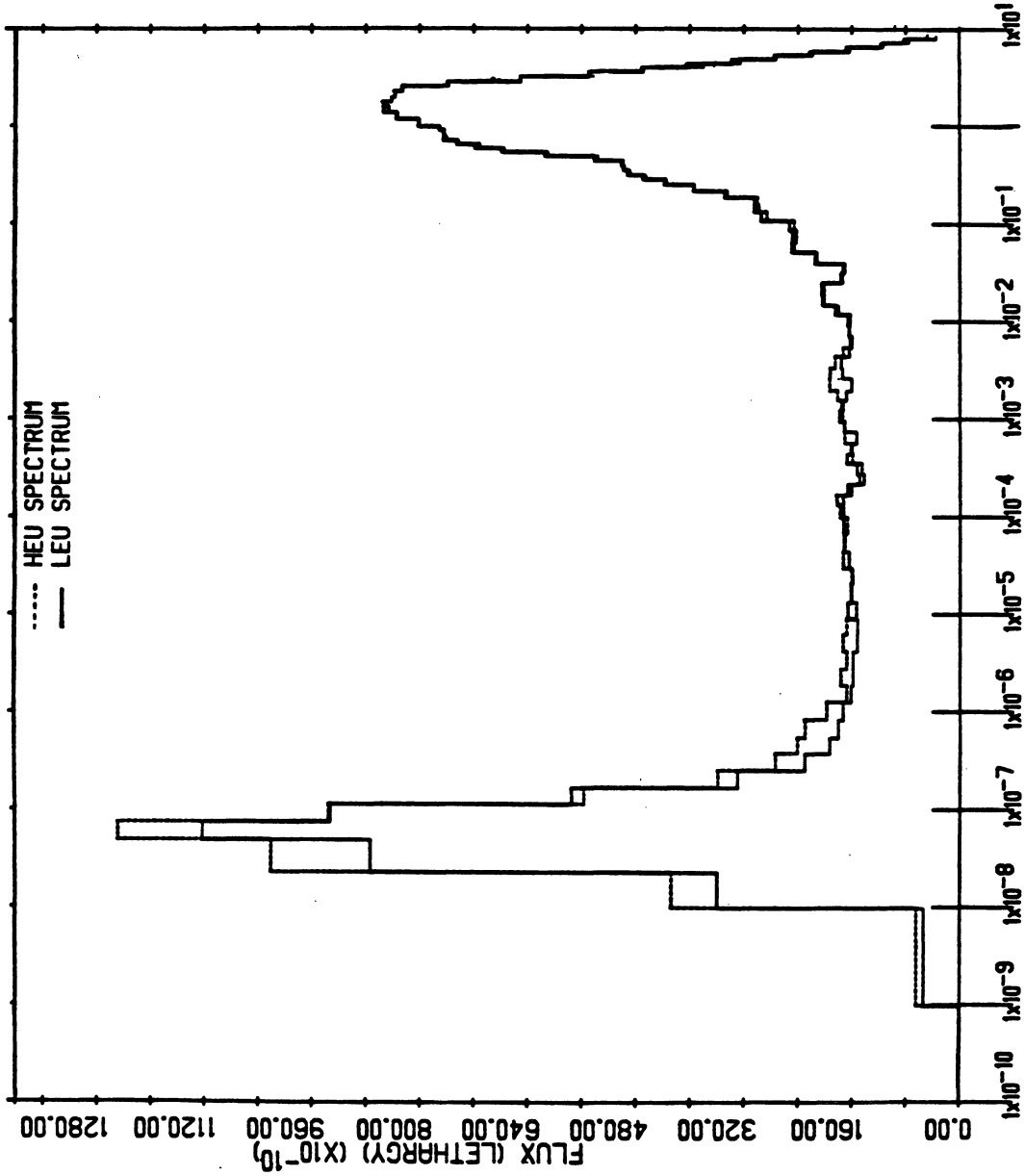


Figure 7 Comparison of normalized HEU and LEU spectra.

spectra since only the neptunium fission reaction has enough sensitivity in this region to alter the calculated spectra. In the region from 10 keV down to 10 eV, there is relatively good agreement in the shape of the spectrum. Both HEU and LEU spectra show identical depressions at about .2 keV for reasons which are not understood. Below 10 eV, the spectra begin to look distinct. It is in this region where the harder nature of the LEU spectrum becomes apparent. This may be related to the $U^{238}$ capture cross section. While the $U^{238}$ capture cross section has many resonances, principal resonances appear at 6.7 eV, 10.2, and 20 eV. If a significant number of neutrons are absorbed in slowing down through these resonances, then one might expect the flux to be slightly lower in this region. In the thermal energy range, the significantly larger HEU thermal flux is quite apparent, and not unexpected.

Table 12 compares the broad group integral fluxes for the HEU and LEU spectra. For each of the three broad groups, the integral flux and its uncertainty, and the fraction of the total integral flux are shown. The uncertainty in the collapsed broad group integral flux is smaller than the average of the uncertainties in the groups comprising it because of the strong correlations between groups. That is, if the differential flux is unfolded to be too large in one energy group, it will usually be too small in a nearby energy group so that the integral activity is close to being correct. Because of these correlations, the uncertainties in integral fluxes are usually much smaller than the uncertainties in the differential fluxes. For the fast flux, a large uncertainty in the integral flux is quoted based on the results shown in Tables 9 and 11. This is because we have used very few threshold foils in the unfoldings. In the next section, we shall show that the HEU fast flux is not different from the value presented in Table 12, and the LEU fast flux is only 4% larger than the value presented here. Furthermore, the uncertainties in these fast flux

Table 12

Broad Group Comparisons of Unfolded Fluxes
HEU Versus LEU

| ENERGY REGION | HEU RESULTS | | | LEU RESULTS | | | NORMALIZED RATIO HEU/LEU |
|---|---|---|---|---|---|---|---|
| | INTEGRAL FLUX ($\times 10^{13}$) | $\delta$(%) | FRACTION of TOTAL | INTEGRAL FLUX ($\times 10^{13}$) | $\delta$(%) | FRACTION of TOTAL | |
| $\phi_{sc}$ (E < .55 eV) | 2.339 | 3.0 | .368 | 2.389 | 3.4 | .347 | 1.19±.03 |
| $\phi_{epi}$ (.55 eV< E <1 MeV) | 2.993 | 4.0 | .471 | 3.250 | 6.0 | .473 | 1.11 |
| $\phi_{fast}$ (E > 1 MeV) | 1.023 | 15.9[1] | .161 | 1.239 | 11.0[1] | .180 | 1.00 |

(1) The actual uncertainty in this value is much smaller. These deconvolutions used only a few threshold reactions, and hence the results show a large uncertainty. The fast flux unfoldings used more reactions, and the integral fast fluxes differ slightly from these values.

values are much lower. The final column of Table 12 shows the values of the HEU to LEU ratio of the integral fluxes normalized to the same fast flux. Note that the ratio of the subcadmium fluxes would increase to 1.22 using the better value for the LEU fast flux presented in the next section. This is slightly larger than the 1.19 value one would expect.

4. Unfolded Fast Flux

The threshold reaction data shown in Table 7 were used to unfold the HEU and LEU core fast fluxes. As expected, the HEU and LEU fast spectra showed the same general characteristics when they were unfolded. In the discussion which follows, we shall present the results of the LEU fast spectral unfolding, but note any differences from the HEU results.

For the fast flux unfolding, the energy region from 1 to 15 MeV was broken into 50 energy groups. A cross section library for this energy grid was developed for the threshold reactions. Not all of the measured threshold data reported in Table 7 were used in the unfoldings. In particular, the $V^{51}(n,\alpha)$, $Mn^{55}(n,2n)$, $Ni^{59}(n, 2n)$ $Np^{237}$(n,fission), and $Mg^{24}(n,p)$ data were excluded from our final unfoldings. The $V^{51}(n,\alpha)$, $Mn^{55}(n,2n)$, and $Ni^{58}(n,2n)$ reactions were not used because the cross sections are not well known. When these cross sections are better determined, this data should be incorporated into the unfoldings. The $Np^{237}$(n,fission) reaction is not included in the fast flux unfoldings reported here because 36% of the activity is produced below 1 MeV. We have performed fast flux unfoldings covering the energy range .5 MeV to 15 MeV using $Np^{237}$, and the measured fluxes are consistent with the data reported in Tables 9 and 11. This is expected since the same $Np^{237}$ data was also used in both of those flux unfoldings. Finally, the $Mg^{24}(n,p)$ reaction was not included because the HEU and LEU solid holder measurements, as well as the LEU hollow holder

measurement, support a cross section which is 10% smaller in order to be consistent with other threshold reaction data covering nearly the same energy region.

Table 13 shows the threshold reactions used, and the energy range of sensitivity to the flux for each case. These energy bands cover the region above 1.4 MeV completely, and their staggered positions imply the shape of the unfolded differential flux should be meaningful. In addition, the reaction rate per target nucleus which would be calculated using the unfolded flux is shown, along with a comparison with the measured activity. The average magnitude of the deviation is 3.7%, which is quite reasonable considering the uncertainties in the cross sections. We have allowed the number of iterations to increase to see if the fit would improve, but the solution changed only minimally. From this, we conclude that the solution is stable with respect to the number of iterations used. Furthermore, we have also employed two least squares unfolding methods (FERRET and STAYSL), but the shapes of the unfolded curves were not significantly different. As a result, we shall limit our discussion to the unfolded LEU results using the semi-empirical method (SANL). Table 14 compares our deviations between measured and unfolded activities with those one would obtain from a more limited set of threshold data measured in the ORR[4]. It is interesting that the first three reactions, which represent some of our worst fit data, show the same type of disagreements after unfolding as the ORR data does. This type of similarity tends to strengthen our confidence in the measured activities, but raises questions about our cross sections.

Table 15 presents the values of the differential unfolded flux, the associated uncertainty for each group (excluding the effects of errors in the cross sections), and the percentage difference between the input spectrum and the unfolded spectrum. We have deliberately separated out the

Table 13

LEU Unfolded Spectrum Activity Comparisons

| REACTION | COVER TYPE | ENERGY RANGE FOR 90% ACTIVITY (MEV) | | UNFOLDED ACTIVITY (1/sec) | RATIO OF MEASURED TO UNFOLDED ACTIVITY | DEVIATION OF MEASURED FROM UNFOLDED (%) |
|---|---|---|---|---|---|---|
| | | LOWER | UPPER | | | |
| IN115(N,N)IN115M | CADMIUM | 1.374E+00 | 5.001E+00 | 3.051E-12 | 1.0064 | 0.64 |
| TH232(N,F)FSPR | CADMIUM | 1.565E+00 | 5.897E+00 | 1.213E-12 | 1.0881 | 8.81 |
| U238(N,F)FSPR | BARE | 1.570E+00 | 5.463E+00 | 5.231E-12 | 0.9366 | -6.34 |
| TI47(N,P)SC47 | CADMIUM | 2.009E+00 | 6.391E+00 | 3.552E-13 | 0.9291 | -7.09 |
| NI58(N,P)CO58 | BARE | 2.322E+00 | 6.579E+00 | 1.657E-12 | 1.0739 | 7.39 |
| ZN64(N,P)CU64 | CADMIUM | 2.658E+00 | 6.407E+00 | 5.191E-13 | 0.9690 | -3.10 |
| FE54(N,P)54MN | BARE | 2.669E+00 | 6.795E+00 | 1.254E-12 | 1.0207 | 2.07 |
| AL27(N,P)MG27 | CADMIUM | 3.847E+00 | 8.430E+00 | 6.711E-14 | 0.9462 | -5.38 |
| CO59(N,P)FE59 | BARE | 3.837E+00 | 8.512E+00 | 2.277E-14 | 0.9529 | -4.71 |
| TI46(N,P)SC46 | CADMIUM | 4.250E+00 | 8.462E+00 | 1.652E-13 | 1.0530 | 5.30 |
| NI60(N,P)CO60 | CADMIUM | 5.318E+00 | 1.002E+01 | 4.013E-14 | 1.0092 | 0.92 |
| FE54(N,A)CR51 | BARE | 5.483E+00 | 1.071E+01 | 1.234E-14 | 1.0695 | 6.95 |
| FE56(N,P)MN56 | CADMIUM | 5.669E+00 | 1.069E+01 | 1.739E-14 | 0.9950 | -0.50 |
| TI48(N,P)SC48 | CADMIUM | 6.122E+00 | 1.181E+01 | 4.397E-15 | 1.0121 | 1.21 |
| AL27(N,A)NA24 | CADMIUM | 6.751E+00 | 1.168E+01 | 1.112E-14 | 1.0076 | 0.76 |
| CO59(N,2N)CO58 | BARE | 1.153E+01 | 1.413E+01 | 2.994E-15 | 1.0053 | 0.53 |
| ZR90(N,2N)ZR89 | CADMIUM | 1.255E+01 | 1.450E+01 | 1.176E-15 | 0.9949 | -0.51 |

Table 14

Comparison of Deviations between Measured and Calculated Activities for FNR and ORR Unfoldings

| Reaction | Deviation between Measured Activity and Unfolded Activity | |
|---|---|---|
| | FNR LEU | ORR[5] |
| $Fe^{54}(n,\alpha)Cr^{51}$ | 7. | 11. |
| $Ti^{47}(n,p)Sc^{47}$ | -7. | -18. |
| $Ni^{58}(n,p)Co^{58}$ | 7. | 6. |
| $Fe^{54}(n,p)Mn^{54}$ | 2. | 5. |
| $Ti^{48}(n,p)Sc^{48}$ | 1. | -8. |
| $U^{238}$(n,fission) | -6. | 8. |

effect of cross section errors on the uncertainty in the unfolded flux to illustrate the best possible results which could be obtained with accurate activation data. However, we have performed the error analysis including estimates of the cross section uncertainties. For this case, the errors shown in Table 15 increase by a factor of ~2-3.5. Thus, the uncertainty in the unfolded flux is dominated by the uncertainties in the cross sections. The uncertainty below 1.5 MeV is larger than at other energies because of the limited amount of foil coverage in this region. Also shown for reference in Table 15 is the unfolded integral flux above each energy E. Table 16 shows the errors associated with some integral fluxes. Comparing column 3 with the errors shown in Table 15, it is interesting that the errors in the integral fluxes are less than the errors in the differential fluxes. This is because of strong correlations between the differential errors which tend to cancel out. This is expected since if the flux is too large in one group, it must

Table 15

Unfolded Differential Fast Flux

| Group Number | Lower Energy (MeV) | Flux (n/cm$^2$-sec-MeV) | | | Integral Flux Above E |
|---|---|---|---|---|---|
| | | Unfolded Spectra | Uncert. (%) | % Diff. from Input | |
| 1 | 0.100E+01 | 0.767E+13 | 16.0 | -2.90 | 0.128E+14 |
| 2 | 0.125E+01 | 0.686E+13 | 12.0 | -7.64 | 0.109E+14 |
| 3 | 0.150E+01 | 0.575E+13 | 9.3 | -4.94 | 0.917E+13 |
| 4 | 0.175E+01 | 0.483E+13 | 7.2 | 0.86 | 0.773E+13 |
| 5 | 0.200E+01 | 0.424E+13 | 5.7 | 2.65 | 0.652E+13 |
| 6 | 0.225E+01 | 0.360E+13 | 4.1 | 2.93 | 0.546E+13 |
| 7 | 0.250E+01 | 0.296E+13 | 4.1 | 2.65 | 0.456E+13 |
| 8 | 0.275E+01 | 0.235E+13 | 4.4 | 3.32 | 0.382E+13 |
| 9 | 0.300E+01 | 0.191E+13 | 4.6 | 5.05 | 0.323E+13 |
| 10 | 0.325E+01 | 0.160E+13 | 4.8 | 5.83 | 0.276E+13 |
| 11 | 0.350E+01 | 0.137E+13 | 5.2 | 5.15 | 0.236E+13 |
| 12 | 0.375E+01 | 0.117E+13 | 5.7 | 3.60 | 0.201E+13 |
| 13 | 0.400E+01 | 0.100E+13 | 5.9 | 2.18 | 0.172E+13 |
| 14 | 0.425E+01 | 0.860E+12 | 5.8 | 1.70 | 0.147E+13 |
| 15 | 0.450E+01 | 0.750E+12 | 5.9 | 1.52 | 0.126E+13 |
| 16 | 0.475E+01 | 0.667E+12 | 5.6 | 0.86 | 0.107E+13 |
| 17 | 0.500E+01 | 0.579E+12 | 4.7 | 0.67 | 0.901E+12 |
| 18 | 0.525E+01 | 0.496E+12 | 4.1 | 0.39 | 0.756E+12 |
| 19 | 0.550E+01 | 0.425E+12 | 4.5 | 0.77 | 0.632E+12 |
| 20 | 0.575E+01 | 0.364E+12 | 6.2 | 2.08 | 0.526E+12 |
| 21 | 0.600E+01 | 0.306E+12 | 6.8 | 3.70 | 0.435E+12 |
| 22 | 0.625E+01 | 0.250E+12 | 5.9 | 5.64 | 0.359E+12 |
| 23 | 0.650E+01 | 0.202E+12 | 5.6 | 7.72 | 0.296E+12 |
| 24 | 0.675E+01 | 0.165E+12 | 5.1 | 9.63 | 0.246E+12 |
| 25 | 0.700E+01 | 0.136E+12 | 4.6 | 11.35 | 0.204E+12 |
| 26 | 0.725E+01 | 0.113E+12 | 4.2 | 12.86 | 0.170E+12 |
| 27 | 0.750E+01 | 0.946E+11 | 4.4 | 14.27 | 0.142E+12 |
| 28 | 0.775E+01 | 0.797E+11 | 4.6 | 15.47 | 0.118E+12 |
| 29 | 0.800E+01 | 0.667E+11 | 4.5 | 16.52 | 0.985E+11 |
| 30 | 0.825E+01 | 0.553E+11 | 4.4 | 17.37 | 0.819E+11 |
| 31 | 0.850E+01 | 0.459E+11 | 4.4 | 18.07 | 0.680E+11 |
| 32 | 0.875E+01 | 0.382E+11 | 4.8 | 18.60 | 0.566E+11 |
| 33 | 0.900E+01 | 0.318E+11 | 5.8 | 19.00 | 0.470E+11 |
| 34 | 0.925E+01 | 0.265E+11 | 7.6 | 19.29 | 0.391E+11 |
| 35 | 0.950E+01 | 0.221E+11 | 9.6 | 19.50 | 0.325E+11 |
| 36 | 0.975E+01 | 0.183E+11 | 11.7 | 19.66 | 0.270E+11 |
| 37 | 0.100E+02 | 0.153E+11 | 13.8 | 19.86 | 0.224E+11 |
| 38 | 0.103E+02 | 0.127E+11 | 15.8 | 20.03 | 0.186E+11 |
| 39 | 0.105E+02 | 0.106E+11 | 17.0 | 19.80 | 0.154E+11 |
| 40 | 0.108E+02 | 0.894E+10 | 15.7 | 18.85 | 0.127E+11 |
| 41 | 0.110E+02 | 0.753E+10 | 13.2 | 17.86 | 0.105E+11 |
| 42 | 0.113E+02 | 0.634E+10 | 15.4 | 16.87 | 0.861E+10 |

| Group Number | Lower Energy (MeV) | Flux ($n/cm^2$-sec-MeV) | | | Integral Flux Above E |
|---|---|---|---|---|---|
| | | Unfolded Spectra | Uncert. (%) | % Diff. from Input | |
| 43 | 0.115E+02 | 0.532E+10 | 19.0 | 16.06 | 0.703E+10 |
| 44 | 0.118E+02 | 0.443E+10 | 18.9 | 16.05 | 0.570E+10 |
| 45 | 0.120E+02 | 0.333E+10 | 12.9 | 18.45 | 0.459E+10 |
| 46 | 0.125E+02 | 0.225E+10 | 7.1 | 20.63 | 0.293E+10 |
| 47 | 0.130E+02 | 0.154E+10 | 5.8 | 22.05 | 0.180E+10 |
| 48 | 0.135E+02 | 0.105E+10 | 8.1 | 23.01 | 0.103E+10 |
| 49 | 0.140E+02 | 0.723E+09 | 10.8 | 23.60 | 0.509E+09 |
| 50 | 0.145E+02 | 0.294E+09 | 30.7 | 23.96 | 0.147E+09 |

be too small in another group so that the integral activities are correct. Because of this cancellation, the unfolding methods excel at predicting integral fluxes over arbitrary energy regions.

Table 16
Analysis of Integral Flux Errors

| Energy Range (MeV) | | Integral Flux Uncertainty (%) | |
|---|---|---|---|
| From | To | no $\delta\sigma$[1] | with $\delta\sigma$[2] |
| 1.5 | 15.0 | 2.56 | 8.24 |
| 1.5 | 4.0 | 3.60 | 10.31 |
| 4.0 | 6.0 | 4.44 | 11.52 |
| 6.0 | 9.0 | 4.47 | 7.60 |
| 9.0 | 12.0 | 9.66 | 24.80 |
| 12.0 | 15.0 | 7.08 | 15.13 |

[1] Uncertainties exclude the effects of errors in the cross sections.

[2] Uncertainties include the effects of errors in the cross sections.

Figure 8 shows $\phi(E)$ versus energy for the calculated measured (solution) spectra. The input and solution spectra are normalized to give the same integral flux above 1 MeV. At 3.25 MeV, the unfolded flux shows a slight dip relative to the HAMMER input flux. Harris[6] attributed a dip in his proton recoil measurements to the oxygen elastic scattering resonance at about 3.5 MeV. Since our thermal and epithermal measured flux had a greater thermal to epithermal flux ratio than the calculations predicted, one might suspect the calculations were based on a model in which we underestimated the amount of water around the holder. If so, one might expect the measured flux to be slightly lower than the calculated flux at 3.5 MeV. From 4 to 6 MeV, the unfolded spectrum follows the shape of the HAMMER calculation

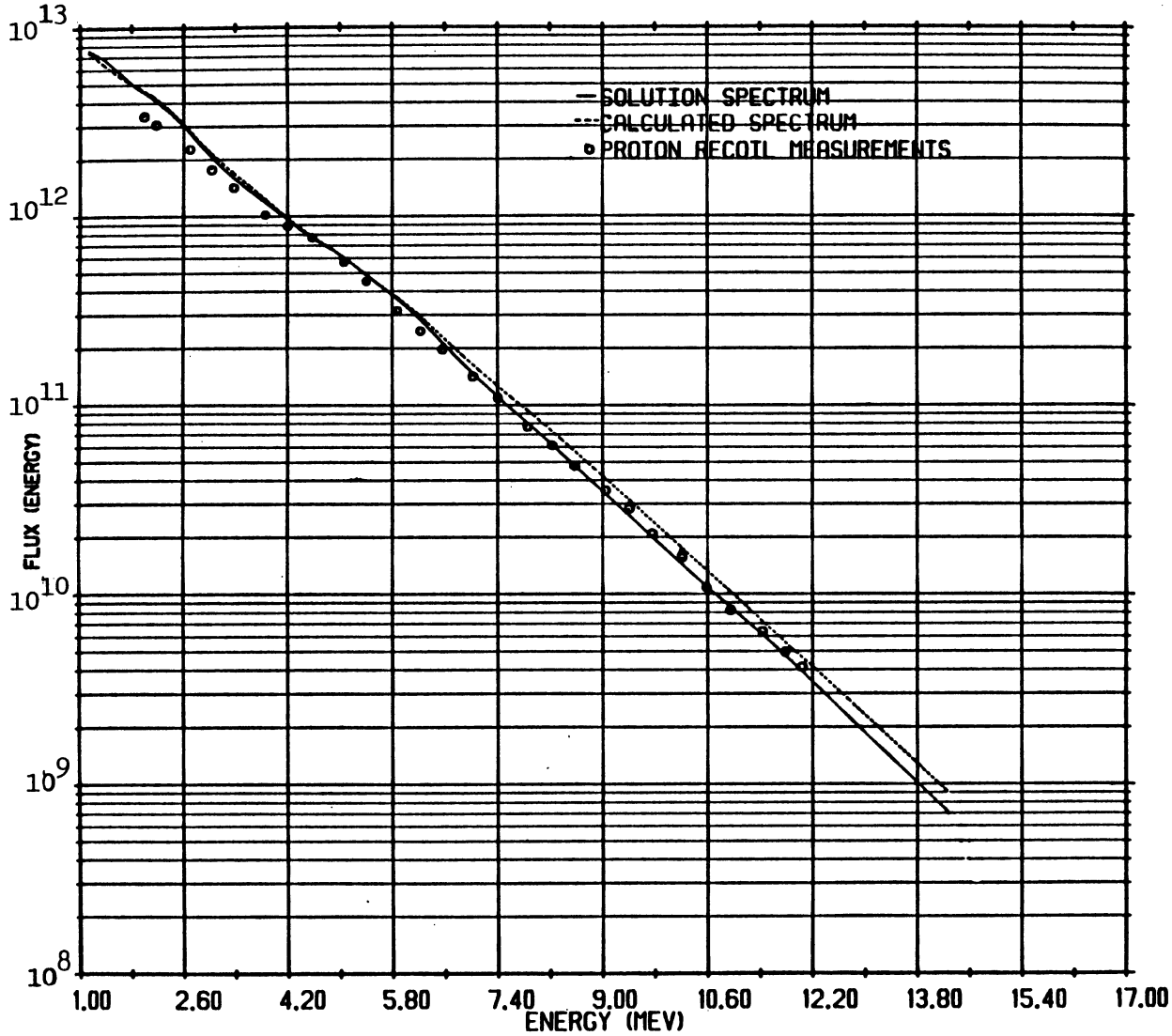


Figure 8 FNR measured and calculated fast spectra.

reasonably well. It is interesting that integral fast spectrum measurements using threshold reactions have shown a large rise in the flux in this region relative to measurements made using other techniques. This has been the source of a controversy between direct differential measurements (e.g., proton recoil, time of flight) and integral measurements (i.e., foil activation) of the fission spectrum. Grundl[7], McElroy[8], and Fabry[9] have independently reported a large (30%) "bulge" in the fast flux in the 3-6 MeV range, or an equivalent hardening in the "temperature" of the fission spectrum from 1.29 MeV to 1.47 MeV. These early measurements used a much smaller set of threshold reaction data than ours, and cross sections which were presumably less accurate.

Figure 8 also shows Harris's proton recoil measurements for comparison. The calculations, unfolded spectrum, and proton recoil measurements agree at 4.5 MeV. It is interesting that our full spectral unfoldings using the newer ENDF-IV cross sections and a more comprehensive set of activation data still appears to show this deviation, although to a smaller extent. This tends to indicate that this controversy between direct differential measurements and integral methods (i.e., threshold activations), may be directly related to the accuracy of the cross sections known at that time. Above 7 MeV, the unfolded flux is significantly depressed relative to the calculated spectrum. It is impressive that a depression of the flux in this energy range was demanded by <u>all</u> of the five (six, if $Mg^{24}$ is included) threshold reactions having sensitivity in this region. For this reason, it is difficult to dismiss this depression as an experimental error. For the HEU and the LEU hollow holder spectrum unfolded using the FERRET, STAYSL, and SANL codes, this depression is also present. In this region, our calculated spectrum consists of a perturbed fission spectrum. The agreement between the measured proton recoil spectrum and the unfolded spectrum is quite good and lends

credence to the shape of the unfolded results. Above 11 MeV, the agreement between the measured and calculated spectra remains poor. In this region, the (n,2n) reactions are providing spectral sensitivity, so one would expect the unfolded results to be meaningful. Above 12 MeV, we do not have any proton recoil data to compare with our unfolded results. Overall, the unfolded spectrum is quite credible. Below 6 MeV, the unfolded spectrum agrees with the HAMMER calculated spectrum reasonably well, but at the lower energies, it deviates from the proton recoil data. Since there will be neutrons scattering down into these lower energies, one would expect the flux at these lower energies to be sensitive to the amount of water in the vicinity of the detectors. Thus, the unfolded flux should exceed the flux seen at the proton recoil spectrometer at lower energies. Above 6 MeV, the unfolded spectrum agrees well with the measured proton recoil data, but deviates from the calculated spectrum. This says that the particular extrapolation that we used to extend the HAMMER calculations was not appropriate, and does not reflect on the accuracy of that set of computer codes.

There are three conclusions we can draw from our fast flux unfolding efforts. First, we recognize that spectral unfolding does not provide the resolution which is available with the direct differential methods, such as proton recoil telescopes. This is inherent in the unfolding method and the shape of the cross sections. In practice, unfolding serves as a means for making refinements to one's best estimate of the spectrum to become more consistent with the integral activation measurements. Second, the unfolded solution does not appear to be significantly dependent upon the method used for the unfolding. The spectral features described above were observed using all three unfolding methods. Solutions from one unfolding method were recognized as solutions to the other unfolding methods. This is not surprising since all methods attempt to minimize the

difference between a measured and calculated activity. If one has a good first approximation to the spectrum, then the changes which must be introduced by the unfolding method will be small, and relatively independent of the technique used to infer the change. Third, we have found the shape of the unfolded spectra to be relatively independent of the input spectrum in those energy regions where there is good foil coverage. We have tried moderately different input spectra for the region above 2 MeV to test this sensitivity, and the solution exhibited the same characteristics shown in Figure 8. Furthermore, it is encouraging that the unfolded solution looks more like the previously measured spectrum rather than the input spectrum above 6 MeV. This indicates that the unfolded solution is more than just a reflection of the input spectrum. Finally, the accuracy of the high energy threshold reaction cross sections are currently the most significant obstacle to performing more precise fast flux unfoldings. Like the thermal and epithermal flux unfoldings, increasing the number of reactions used in the unfoldings may improve the resolution of the differential unfolded spectrum. However, because the cross sections are smoother and the energy coverage more complete, one does not require the same amount of consistency between the measurements and cross section sets to prevent unphysical features in the unfolded spectrum. Thus, to some extent, unfolding the fast flux is an easier problem than unfolding the thermal and epithermal fluxes. But the error analysis has also shown that the accuracy of the unfolded spectrum is currently limited by the accuracy of the threshold cross sections. The errors in the differential fluxes have been estimated to be 15-40%, which is too large to expect to accurately see small perturbations in the spectrum. A complete set of threshold reactions (~15-20) with accurately known cross sections (~±3-5%) is probably required to be able to confidently unfold the differential fission spectrum with good precision and resolution. While the accuracy of many

threshold cross sections has improved in the past 15 years, these conditions have still not been met. However, considering the difficulty of inferring differential quantities from integral measurements, it is impressive that the technique works even as well as it does.

## 5. Summary and Conclusions

The large number of reaction rate measurements has allowed a comparison of the consistency of the cross sections. For most reactions, there is a good agreement between the fluxes predicted using the measured activities and the cross sections. However, the iron capture reaction at thermal energies appears to be 10% too small when compared with the results of the measurements made using cobalt, gold, silver, manganese, and copper foils. We have also noted in a separate work that there are inconsistencies in the gold total cross section at thermal energies which also need resolution. At higher energies, the $Mg^{24}(n,p)$ cross section yields a fast flux which is inconsistent with the results obtained using other threshold reactions. Based upon our measurements, this cross section should be decreased by 10%. The $Zn^{64}(n,p)$ cross section measured by Argonne National Laboratory is substantially different from the ENDF-IV evaluation. Since only the ANL cross section yields a reliable fast flux when applied to our measurements, we suggest the ANL cross section is more accurate. At very high energies (E>10 MeV), the accuracy of the cross sections in general is not particularly good. Precision measurements of the cross sections at these energies are difficult, but they are needed for more accurate deconvolutions of the high energy differential fast flux.

Regarding the unfolding methodology, we did not find much difference between the spectra determined with the semi-empirical and least squares unfolding techniques. This may have been because our initial estimate of the shape of the spectrum was too consistent with the activation measure-

ments, so the amount of change required by the unfolding codes was not dramatic. We did, however, discover that the choice of the input spectrum normalization can affect the shape of the unfolded spectrum. This is an area which we believe has not been generally explored. The interactive semi-empirical unfolding program we have developed is similar to the SAND-II algorithm, and has the advantages of speed, flexibility, convenience, and accuracy. It allows the user to graphically see the effects of each measured reaction rate on the unfolded flux, and provides a physical feel for the solution. The least squares methods we explored provide the mathematical guarantee of a minimum variance solution, and a rigorously correct error analysis. This latter advantage is the practical motivation for using the least squares techniques. However, while the error propagation is rigorous, the resulting errors are dependent upon knowledge of the uncertainties in the input spectrum, which are not well known. This is an area which has been receiving attention, and may make the least squares methods even more advantageous in the future.

The HEU and LEU spectra were found to be measurably different, particularly below the principal $U^{238}$ capture resonances. For the same integral fast flux, the LEU integral subcadmium flux was measured to be 19±3% smaller than the HEU value. This corresponds almost exactly to the difference in the $U^{235}$ number densities. Above 1 MeV, there were no measurable differences between the HEU and LEU spectrum. The unfolded fast spectrum agrees well with the measured proton recoil data above 4 MeV. A clean comparison of just these measured data is shown in Figure 9 for reference. This level of agreement was achieved by using a large number of accurate threshold reaction data, recent ENDF-IV and -V cross sections, and the fact that the spectrum is sufficiently smooth (i.e., small second derivatives) at these energies so the lower resolution of the multiple foil method was not critical. From this, we con-

clude that the multiple foil method can be used to measure absolute differential fast spectra reasonably accurately.

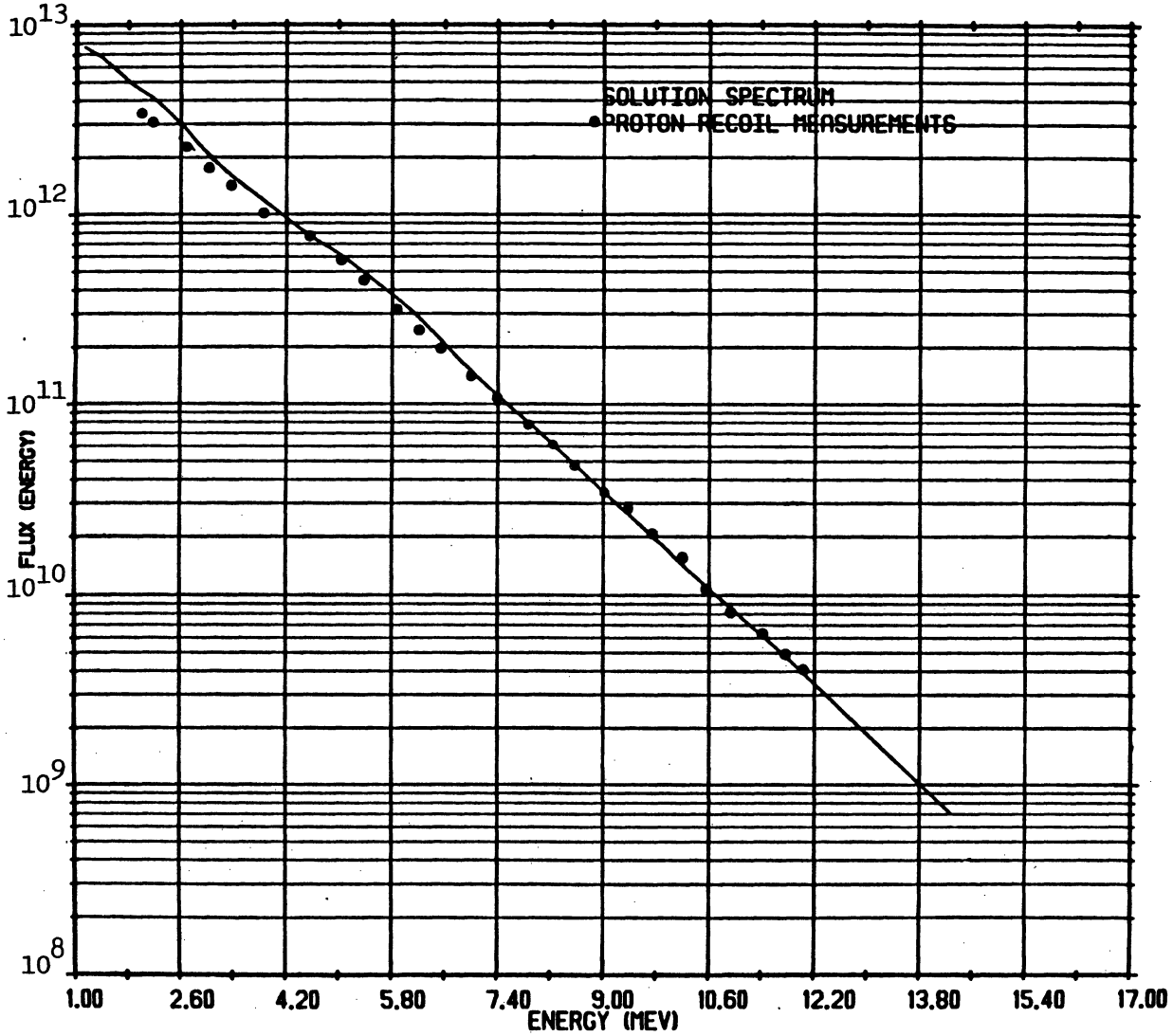


Figure 9 FNR measured fast flux

REFERENCES

1. D. K. Wehe and J. S. King, "FNR Demonstration Experiments Part II: Subcadmium Neutron Flux Measurements", Proc. of the Int'l Meeting on Development, Fabrication, and Application of Reduced Enrichment Fuels for Research and Test Reactors, ANL/RERTR/TM-4, Argonne National Laboratory, Argonne, IL (September 1983).

2. D. K. Wehe and J. S. King, "FNR Demonstration Experiments - Part I: Beam Port Leakage Currents and Spectra", Proc. of the Int'l Meeting on Development, Fabrication, and Application of Reduced Enrichment Fuels for Research and Test Reactors, ANL/RERTR/TM-4, Argonne National Laboratory, Argonne, IL (September 1983).

3. M. A. Kirk. R. C. Birtcher, T. H. Blewitt, L. R. Greenwood, R. J. Popek, and R. R. Heinrich, "Measurements of Neutron Spectra and Fluxes at Spallation-Neutron Sources and Their Application to Radiation Effects Research", Journal of Nuclear Materials, 96 (1981) 37-50.

4. L. R. Greenwood, personal communication, 1979.

5. N. A. Frigerio, Nucl. Instr. Meth.,114 (1974) 175.

6. Lawrence Harris, Jr., Measurement of Fast Neutron Spectra in Water and Graphite, Ph.D. Thesis, Department of Nuclear Engineering, University of Michigan, Ann Arbor, MI, 1967, p. 68.

7. J. A. Grundl, "A Study of Fission-Neutron Spectral with High-Energy Activation Detectors", Nucl. Sci. Eng., 31, (1968) p 191-206.

8. W. M. McElroy, "Implications of Recent Fission-Averaged Cross-Section Measurements", Nucl. Sci. Eng., 36, 109 (1969).

9. A. Fabry and M. DeCoster, "Integral Test of Capture Cross Sections in the Energy Range 0.1-2.0 MeV", Proceedings of the Second Conference on Neutron Cross Sections and Technology, Spec. Publ. 299, Vol. 2, p 1263, National Bureau of Standards (1968).